

RICE UNIVERSITY

**Single-Molecule Studies of Proteins at Polymer based
Chromatographic Interfaces**

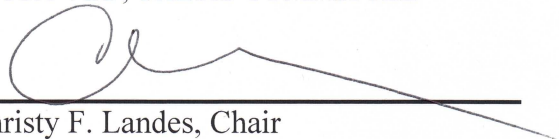
by

Nicholas A Moringo

A THESIS SUBMITTED
IN PARTIAL FULFILLMENT OF THE
REQUIREMENTS FOR THE DEGREE

Doctor of Philosophy

APPROVED, THESIS COMMITTEE



Christy F. Landes, Chair
Professor of Chemistry, Electrical and
Computer Engineering, and Chemical and
Biomolecular Engineering



Sibani Lisa Biswal
Professor, Associate Department Chair,
Director of Graduate Studies, Chemical
and Biomolecular Engineering
Associate Professor of Material Science
and Nano Engineering



Matteo Pasquali
Professor of Chemical and Biomolecular
Engineering

HOUSTON, TEXAS
December 2019

Abstract

Single-Molecule Studies of Proteins at Polymer based Chromatographic Interfaces

by

Nicholas Anthony Moringo

The worldwide pharmaceutical landscape has witnessed a large influx of biological-based therapeutics, termed 'biologics', for the successful treatment of diseases and illnesses. The downstream separation and purification of promising biologics via chromatography dominates the total production cost leading to market entry. A mechanistic examination of protein interactions at the interface of stationary phase materials can improve and enable predictive chromatographic separation optimization. Single-molecule imaging techniques, inspired by the advances of super-resolution microscopy, can capture the highly dynamic interactions of proteins at stationary phase materials. It is observed that nanoscale protein dynamics can explain experimentally observed increases in separation efficiencies. We uncover how the suppression of anomalous surface diffusion, which leads to improved separations, can be tuned with stationary phase surface chemistries, polymer packing, and ionic salt conditions. Overall, we have shown that single-molecule imaging can relate protein dynamics at the nanoscale to improved protein separations at the interface of synthetic polymer materials.

Acknowledgments

There are many people in my life that have played a critical role in my accomplishments. Without them, I would not have had the incredible opportunity to explore my scientific curiosities in the last four and a half years at Rice University. So fair warning, this is going to be a long one.

Most importantly, I have to thank my colleague, life-long partner, and incredible wife Nicole Moringo for her unconditional love, support, and competitive drive that always pushes my intellectual endeavors to higher levels. From the day I met you at UC: Irvine I knew I had found something special, someone, that could kick my ass on every exam and shove it in my face, driving me to study harder and harder daily. There is so much more I can say about how important you are to my success in this program (such as collaborating on projects together), but our story is just in the beginning chapters, and I cannot wait to see what we conquer next as a team!

To my advisor Dr. Christy Landes, I could not have made it down this scientific journey without your guidance. At times I wanted to quit, give up, or never come back but you always motivated and inspired me to keep pushing. You are a great role model and an incredible scientist. I am very proud to have been advised by you during this experience. I am very grateful for the opportunity to expand my knowledge of scientific tools, techniques, and more importantly how to write properly using which and that. Most importantly Christy, thank you for pushing me to develop scientific independence in the lab. Also, thank you to my committee

members Dr. Biswal and Dr. Pasquali for their time serving on my committee and giving important feedback. Also, thank you to Dr. Link for always being supportive, offering constructive scientific feedback, and offering guidance during group meetings it was a pleasure working with you.

Of course to my incredible and crazy friends and family. To my mother, Colleen, for always sending me meditation videos and crazy natural “remedies” to combat the stress of graduate school, I could have not done this without you. To Esteban, if anyone in my life has taught me to fight for what you want and to never give up it is you. Watching you take down the best golfers in the world week after week coming from poverty in Mexico, has shown me that anything is possible in life, but you have to fight for it. To my father Nick, you have always been there for me through thick and thin and I appreciate everything you and Tracy do for me. To my siblings Eden, Ryan, Mason, and Madisyn I love having you in my life and wish you nothing but success in your lives. To my incredible in-laws, Chris and Ambrose, your love and passion for Nicole and I is always supportive, insightful, and inspiring. Last but not least, to my incredible friends Sam Drake and Justin Sieker. The random golf trips, phone calls, and text messages of memes that made me laugh during the tough days in the lab were some of the most motivating parts of graduate school. Cheers to more golf trips and lasting memories, but please get some golf lessons Sieker. Jack Drake thank you for always calling to check in and chat about life. Also thank you to my grandparents Frank, Jan, Ann, and Dominick for your support and love. Also to my Aunt Natalie and Uncle Rich. The things you instilled in me at a young age are things that I carry with me in science daily.

Also, I could have not have gotten through challenging times without the wonderful friends and colleagues I met at Rice University. David Renard, your uplifting personality, intellectual knowledge, and “let’s do it” attitude for wine breaks at any time to recover from graduate school kicking us in the face are some of the memories I will never forget. I look forward to seeing our friendship grow beyond Rice. Colleagues and drinking friends: Logan Bishop and Thomas Heiderscheit thank you for the funny lunchtime stories, puns (I can’t believe I wrote that), and most importantly laughs that pushed us all through the day-to-day at Rice. To my hacker golf buddies, at Rice, Carlos Origel and Ben Hoener, I hope you both get golf coaches soon, but I must say chasing your golf balls all over the Woodlands sure was a blast. I hope to find you both in the fairway soon. Also, to members of the Link-Landes family Lauren, Lauren, Sudeshna, and Rashad thank you for your friendship, feedback, and being amazing co-workers. I appreciated the chance to work with all of you. Also to Dr. Lesa Tran, I enjoyed teaching for you and learning more about Rice, especially being the first TA for The Chemistry of Cooking course. Your mentorship, guidance, and long chats in your office will never be forgotten.

To my fantastic dog Lilly, you were a pain and a lot of work when we got you at 1.4 lbs, but the joy, energy, and love you bring into our house is truly incredible. The walks on campus in the evening watching you ‘hunt’ squirrels, chase balls, and bounce in the bushes at lizards truly disconnects my mind from the daily stress of life. I could not have asked for a better dog to bring into our house, and I am sure you feel the same way with how much we spoil you every day. Your mom, Nicole, cooks for you more than she cooks for me😊.

I have to say without Hao Shen as a mentor in my early days at Rice, I do not think I would have been a successful graduate student. Your wisdom, patience, and dedication to helping me from cleaning slides to writing my first manuscript were learning experiences that I will hold close to my heart. Hao, I cannot say this enough but thank you for everything. I wish you the best as a faculty member at Kent State. Joey Tauzin although I couldn't execute a serial dilution on day one we sure have come a long way. Thank you for all your input and guidance in my research in the Landes group. It was a pleasure working with you and long live the pumpkin pants in your mind!

To the Esteban Toledo Family Foundation. Thank you for allowing me to be a part of such a fantastic story and mission to help orphans in Mexicali, MX. You have indeed given me the ability to grow outside of the realms of science and contribute to the philanthropic efforts of an amazing foundation.

Also a huge thanks to all the staff at the Woodlands Country Club. Coming out and ripping golf balls at the amazing tree-lined tournament course was crucial in my success at Rice. Chris, Richard, Austin, and Darrell thank you for all your kindness and allowing me to play out there so often.

Lastly, to the New York Yankees, I am very angry that you couldn't take down the Astros once while I lived here to go to the World Series, but I forgive you because we know you have more rings than any team and are still the best team over in the MLB. But please finally get your act together and win a championship again soon.

Funding Acknowledgments

This work was funded by the Welch Foundation [C-1787 and C-1664] and the National Science Foundation [CHE-1151647, CHE-1808382, and CBET-1438634].

Also, Nicholas Anthony Moring acknowledges that this material is based upon work supported by the National Science Foundation Graduate Research Fellowship Program under grant no. 1450681 and grant no. 1842494.

Contents

Abstract	ii
Acknowledgments.....	iii
Funding Acknowledgments.....	vii
Contents	viii
List of Figures	xii
List of Equations	xviii
Abbreviations.....	xix
Chapter 1 Introduction	1
1.1. Motivation	1
1.2. Background.....	4
1.3. Specific Aims.....	5
1.3.1. <i>Aim 1: Relate surface chemistry modalities at industrial relevant polymer support to nanoscale protein dynamics.....</i>	<i>6</i>
1.3.2. <i>Aim 2: Establish a relation between single-molecule dynamics to theoretical and ensemble improvements in separation efficiencies under salting out conditions</i>	<i>6</i>
1.3.3. <i>Aim 3: Link the suppression of anomalous surface diffusion of a model protein to the free volumes present in thin polymer films</i>	<i>6</i>
1.4. Overview.....	7
Chapter 2 Background	9
2.1. Abstract	9
2.2. Origin and Advancement of Single-Molecule imaging.....	10
2.3. Previous single-molecule studies at heterogeneous surfaces	16
2.3.1. Protein Unfolding at Stationary phase support materials.....	24
2.3.2. Competitive protein dynamics	29
2.3.3. Protein transport super-localized under nanoconfinement	30
2.3.4. 3D imaging and tracking and novel point spread functions.....	34
2.4. Conclusion	38

Chapter 3 Variable lysozyme transport dynamics on oxidatively functionalized polystyrene films.....	39
3.1. Abstract	39
3.2. Introduction.....	40
3.3. Materials and Methods	43
3.3.1. Polystyrene Film Preparation and Ellipsometry	43
3.3.2. Polystyrene Functionalization	44
3.3.2.1. UV Functionalization	44
3.3.2.2. Plasma Treatment	44
3.3.2.3. Ligand Grafting.....	45
3.3.3. Wide-field Single Molecule Fluorescence Microscopy.....	45
3.3.4. Protein Preparation	47
3.3.5. Goniometry Measurements	47
3.3.6. Atomic Force Microscopy	47
3.3.7. X-ray photoelectron spectroscopy	47
3.4. Results and Discussion	48
3.4.1. UV Treatment	50
3.4.2. Plasma Treatment.....	55
3.4.3. Ligand Grafted	59
3.4.4. Functionalization technique comparison	62
3.4.5. AFM Surface Roughness Analysis	64
3.5. Conclusion	66
Chapter 4 A mechanistic examination of salting out in protein-polymer membrane interactions.....	68
4.1. Abstract	68
4.2. Significance.....	69
4.3. Introduction.....	70
4.4. Materials and Methods	73
4.4.1. Single-molecule tracking.....	73
4.4.2. Nylon Film Preparation and Microfluidic Assembly	74
4.4.3. Nylon Film Ellipsometry	75
4.4.4. Fluorescent Protein Solution Preparation	75

4.4.5. Nylon Bead Preparation.....	75
4.4.6. Ensemble Fast Protein Liquid Chromatography	76
4.4.7. Monte Carlo Chromatographic Simulations	77
4.4.8. Processing and fundamental workings of Simulated Chromatograms	79
4.5. Results and Discussion	80
4.5.1. Transferrin surface dynamics	80
4.5.2. Single-molecule Transferrin Kinetics	84
4.5.3. Ensemble Circular Dichroism	88
4.5.4. Fast Protein Liquid Chromatography.....	90
4.5.5. Monte Carlo Chromatographic Simulations	92
4.6. Conclusions.....	96
Chapter 5 Polymer free volume effects on protein dynamics at polystyrene revealed by single-molecule spectroscopy	98
5.1. Abstract	98
5.2. Introduction.....	99
5.3. Materials and Methods	102
5.3.1. Preparation of polymer films.....	102
5.3.2. Polymer thickness and refractive index characterization	103
5.3.3. Film annealing and modification	103
5.3.4. mPEG Doping of PS	103
5.3.5. Protein Dilutions and fluorescence labeling.....	104
5.3.6. Protein surface charge and hydrodynamic measurements	104
5.3.7. Single-molecule measurements	104
5.3.8. Protein molecule identification and tracking	105
5.4. Results and Discussion	106
5.4.1. α -LA adsorption and dynamics at PS surface	106
5.4.2. Adsorption of Lys on pure PS surface	109
5.4.3. Lys adsorption at Annealed and Cyclohexane developed PS films	113
5.4.4. Lys dynamics at mPEG doped PS films	116
5.5. Conclusion	118
Chapter 6 Conclusion and Future Outlooks	120

6.1. Overall Conclusions	120
6.2. Future Directions.....	122
Chapter 7 SI Appendices	123
7.1. Appendix to Chapter 2: Variable Lys transport dynamics on oxidatively functionalized polystyrene films	123
7.2. Appendix to Chapter 3: A mechanistic examination of salting out in protein- polymer membrane interactions	144
7.3. Appendix to Chapter 4: Polymer free volume effects on protein dynamics at polystyrene revealed by single-molecule spectroscopy	166
References	180

List of Figures

Figure 1.1 Energy expenditure on Chemical Separations in the United States as of 2019.	2
Figure 1.2 Comparison of small molecules vs. biologics within the top ten retailed pharmaceuticals in the United States reported in billions of dollars from 2008 to 2018.²	3
Figure 2.1 Jablonski Diagram.	11
Figure 2.2 Super-localization using point spread function (PSF) fitting for nanometer spatial resolution. (A) The PSF of a single molecule in a bacteria cell. (B) 2D histogram of pixels counts for PSF in (A). (C) 2D Gaussian used to fit PSF in (B). (D) Final localization of the center of mass of the Gaussian function used in (C). Reproduced with permission from <i>Angewandte Chemie Intl. Edition</i>.....	12
Figure 2.3 Fundamentals of super-resolution reconstruction imaging. (A) Ground truth image with black dots representing single dye molecules. (B) Image captured exciting all emitters at a time resulting in a diffraction-limited image. (C) Photoswitching dyes emission (D) stochastically exciting sparse subsets of emitters during each camera exposure. (E) Final reconstructed image by fitting each emitter's PSF and determining localization below the diffraction limit of light over many camera frames. Reproduced with permission from <i>Angewandte Chemie Intl. Edition</i>.....	13
Figure 2.4 Typical through objective widefield total internal reflection fluorescence microscope setup.....	14
Figure 2.5 Super-resolved α-lactalbumin adsorption and desorption at clustered ligands on agarose. (A) Specific adsorption sites are quantified by identifying single adsorption events in each image frame. (B) Adsorption frequency dependence vs. ligand cluster size. (C) Cumulative distribution of α-lactalbumin residence times at different ligand sites. (D) Ensemble averaged elution profiles for engineered ligand clusters (603 sites, red) and stochastically clustered ligands (1,706 sites, cyan) on functionalized agarose supports. (E, F) Ionic strength dependence of the number of specific adsorption sites (E) and total adsorption events per site (F). Adapted with	

kind permissions from the National Academy of Sciences ³² and 2014 Elsevier.⁶⁵ 17

Figure 2.6 Imaging complex protein motion on chromatographic supports. (A) Example trajectories of α -lactalbumin proteins exchanging at a silica support under two pH conditions. (B) A schematic illustration of one proposed type of motion, desorption-mediated continuous time random walk. Adapted with kind permission from John Wiley and Sons ⁷⁸ and the American Physical Society.⁷⁹..... 23

Figure 2.7 Lysozyme adsorption-unfolding dynamics on a fused silica support. (A) Representative trajectories of single lysozyme proteins undergoing a “search” process for unfolding sites on FS interface. Black segments of each trajectory represent the folded lysozyme state and red segments indicate unfolded conformation. (B) Cartoon representation of proposed model behind surface induced unfolding of lysozyme at unfolding sites. (C-F) Distributions of trajectories Euclidean distance before first detected unfolding event at total lysozyme concentrations of: (C) 1.0×10^{-10} M, (D) 1.5×10^{-9} M, (E) 5.5×10^{-9} M, and (F) 7.1×10^{-8} M. Labeled lysozyme concentrations were held constant in C-F. Scale bar in (A) represents 5 μ m. Adapted with the kind permission of the American Chemical Society.¹⁰⁵ 26

Figure 2.8 Relating pore structure and analyte transport using fcsSOFI. (A) Extracting diffusion coefficients from simulated 1D diffusion with fcsSOFI. (B) Simulated frame-averaged image of emitter diffusion in two pores located within the diffraction limit of each other. True pore positions are labeled by the arrows. (C) The pore structure resolved with 2nd order fcsSOFI calculation and one step of blind deconvolution. (D - E) Diffusion coefficient distribution and pore size from diffraction-limited image and fcsSOFI image, respectively, of 1% agarose structure. (B - E) Scale bar = 2 μ m. Figure adapted from American Chemical Society.¹²⁶ 32

Figure 2.9 Application of DH PSF microscopy to study porous support structure. (A) Scheme of double helix PSF 3D microscopy. (B) Representative data of standard PSF and double helix PSF. Scale bar = 2 μ m. (C) DCDHF-P molecules diffusing in thick PMMA polymer substrate. Scale bar = 2 μ m. (D) Localization of fluorescent beads in 3D on porous polystyrene film by fitting the DH PSFs. (E) Overlay of fluorescent bead 3D localizations on the bright field image of porous polystyrene film. Figures (A - C) are adapted from National Academy of Sciences ⁷⁶ and (D - E) are adapted from Scientific Reports.²⁷ 35

Figure 2.10 Application of the stretching lobed PM. The orientation of lobes encodes arrival time shown on the y-axis. Axial emitter location is encoded by the distance between the lobes shown on the x-axis. Reprinted with permission from *OSA publishing*. 37

Figure 3.1 Experimental setup using a TIRF excitation geometry. Evanescent wave depicted in the excitation of Rhodamine-B labeled lysozyme probe with maximum evanescent intensity at the film-liquid interface. (B) Representative time-dependent lysozyme trajectories from 1,000 frames of data on as prepared polystyrene film with camera integration time of 30 ms (Scale bar is representative of 2 μm). (C) Structure of polystyrene and structure of lysozyme (PBD: 4Z98, hen egg white lysozyme¹⁸³) with secondary structural motifs indicated by various colors (left to right). (D) Structure of Rhodamine B dye with counter-ion..... 49

Figure 3.2 Lysozyme adsorption at UV-treated polystyrene interfaces. (A) Static contact angle measurements for polystyrene and UV treated polystyrene films with corresponding treatment times. Lysozyme binding rates (B) and single frame displacements distributions (C) for polystyrene and UV-treated polystyrene (10, 20 and 30 minute treatments). Error bars in (B) represent the standard deviation of the mean from at least 1,600 imaged adsorption events. Each condition in (B, C) represents at least 800 events worth of data..... 51

Figure 3.3 Lysozyme adsorption at plasma treated polystyrene interfaces. (A) Static contact angle measurements for polystyrene and plasma treated polystyrene films. (B) Binding rates of lysozyme onto polystyrene (0 sec.) and oxygen plasma treated polystyrene. Error bars for each treatment time represent the standard deviation of the mean from at least 1,600 adsorption events. (C) Cumulative distributions of surface residence times for respective treatment times outlined in (A). Distributions are fit to the sum of two exponentials indicated by solid lines. (D) Single frame displacement distributions for respective treatment times in (A, B). (E) Representative time-dependent lysozyme trajectories from 1,000 frames of data from treatment times represented in (B-D) (Scale bar is representative of 2 μm). Each condition in (B-D) represents at least 800 events worth of data..... 55

Figure 3.4 Lysozyme adsorption at ligand grafted polystyrene interfaces. (A) Binding rates of lysozyme onto polystyrene (0 min.) and ligand grafted polystyrene. Error bars for each treatment time represent the standard deviation of the mean from at least 1,600 adsorption events. (B) Cumulative

distributions of surface residence times for respective grafting times outlined in (A). Distributions are fit to the sum of two exponentials indicated by solid lines. (C) Single frame displacement distributions for ligand grafted polystyrene surfaces represented in (A, B). (D) Representative time-dependent lysozyme trajectories from 1,000 frames of data from treatment times represented in (A-C) (Scale bar is representative of 2 μm). Each condition in (A-C) represents at least 800 events worth of data.59

Figure 3.5 Atomic force microscopy analyses of surface roughness on as prepared and oxidized polystyrene samples, all images shown are $1 \times 1 \mu\text{m}^2$ area (Scale bar = 500 nm). Samples (A-D) are representative of: (A) native polystyrene (B) UV treated polystyrene (30 min.) (C) plasma treated polystyrene (7 sec.) and (D) ligand grafted polystyrene (30 mins). Root Mean Squared (RMS) surface roughness values (nm) were determined by taking surface roughness measurements using Nanoscope analysis software (Version 1.5) and measuring $2 \times 2 \mu\text{m}^2$ iteratively on 5 separate regions of two samples for each treatment. Error is the standard deviation of sampled data for each method.64

Figure 4.1 Transferrin surface dynamics at nylon at varied ionic strengths. (A) Cartoon representation of two modes of transferrin-nylon interaction, CTRW (cyan) and single site adsorption-desorption (magenta) (PBD: 1D3K²⁷⁶). (B) Representative single-molecule transferrin trajectories at nylon interface undergoing a CTRW (cyan) and single site adsorption-desorption (magenta). (C) Percentage of transferrin molecules exhibiting CTRW vs. simple adsorption-desorption. (D) Single frame displacement distributions at varied ionic strengths. (E) Percent of single frame displacements contributing to immobile and hopping surface transport from sampling distributions in C. The 0 mM condition is shown on logarithmic scale in (C, E) in order to display entire range of salt concentrations.82

Figure 4.2 Transferrin kinetics at nylon at varied ionic strengths. (A) Rate of adsorption. (B) Surface residence time distributions represented in a cumulative distribution and fit to a double exponential decay with solid lines (Equation 4.2). (C) Pre-exponential coefficients from fitting results in (B). (D) Desorption rate constants from fits in plot (B).85

Figure 4.3 Structural examination of transferrin at nylon surface under varied ionic conditions. Cartoon depiction of folded transferrin (A) and unfolded transferrin (B) at nylon in the presence of salt (PBD: 1D3K²⁷⁶). (C) Ensemble

CD spectroscopy of transferrin at varied ionic conditions in the presence of nylon microspheres.	88
---	----

Figure 4.4 FPLC of transferrin with nylon membranes. (A) Transferrin chromatograms under salting out conditions with calculated mean retention times and standard deviation from triplicate separations (inset). (B) Full width half maximum of chromatograms shown in (A).	91
--	----

Figure 4.5 Simulated chromatograms using Monte Carlo simulations. (A) Cartoon depicting contribution of two desorption rate constants on final elution profile line shape. (B) Peak aligned chromatograms simulated from 500,000 molecules using values extracted from CDF fits shown in Fig. 2B-D. (C) Measured FWHM of the peaks shown in B with error bars representing standard deviation of simulations performed five times with 100,000 molecules.	96
--	----

Figure 5.1 α -LA adsorption and dynamics at PS films. (A) The central localization for a single α -LA in 63 consecutive frames. (B) 2D histogram of combined central localizations from 20 α -LA molecules. (C) Single frame displacement distributions for α -LA adsorbed onto PS films with varied PS MWs. (D) α -LA surface residence time cumulative distributions fit to Equation 4.2 (solid lines).	107
---	-----

Figure 5.2 Lys adsorption and dynamics at PS films. (A) Representative trajectories of single Lys at the interface of PS (MW=36k) with color map representing frame number for each trajectory. (B) Single frame displacement distributions for Lys on PS films with varied MWs. α -LA distribution shown for comparison. (C) Lys hopping distributions with the calculated mean and standard error of the mean at each MW of PS. (D) Cumulative distribution of surface residence time for Lys with fits to Equation 4.2 shown in the solid lines.	111
---	-----

Figure 5.3 Lys dynamics at thermally annealed and cyclohexane developed PS films. (A) Single frame displacement distributions for as-prepared and thermally annealed PS films. (B) Surface residence time distributions for as-prepared and thermally annealed PS films with fit to Equation 4.2 shown with solid lines. (C) Single frame displacement distributions for toluene and cyclohexane developed PS. (D) Surface residence time distributions for toluene and cyclohexane developed PS films with fit to Equation 4.2 shown with solid lines.	113
--	-----

Figure 5.4 Comparison of Lys dynamics at as-prepared and mPEG doped PS films. (A) The distributions of single frame displacements at as-prepared and mPEG doped PS films. (D) Cumulative distribution of surface residence time for Lys adsorption at as-prepared and mPEG doped PS films. Solid lines are fits to Equation 4.2. 116

List of Equations

Equation 2.1 The Abbe diffraction limit of light. ⁴⁰	11
Equation 2.2 Snell's Law. ⁵⁹	15
Equation 2.3 Lévy spectral function.	18
Equation 2.4 Poisson distribution of dwell times.....	19
Equation 2.5 fcsSOFI second order autocorrelation spatial enhancement with relation to diffusion coefficient.....	31
Equation 2.6 Spatial resolution of final fcsSOFI image.	32
Equation 4.1 Time spent at stationary phase support as per Giddings and Eyrings statistical model. ⁶⁶	77
Equation 4.2 Two term exponential for desorption rate constants.....	86
Equation 7.1 Radius of Gyration	131
Equation 7.2 Radius of Gyration Tensor	132
Equation 7.3 Molar Residue Ellipticity conversion	146

Abbreviations

PSF	Point Spread Function
TIRF	Total Internal Reflection Fluorescence
CTRW	Continuous Time Random Walk
EMCCD	Electron Multiplying Charge Coupled Device
FWHM	Full Width at Half Maximum
Lys	Lysozyme
FPLC	Fast Protein Liquid Chromatography
α -LA	alpha-lactalbumin

|Chapter 1

Introduction

^α Portions of this Chapter are reproduced with permission from published work: **Moringo, Nicholas A.**, Hao Shen, Logan D.C. Bishop, Wenxiao Wang, and Christy F. Landes. "Enhancing analytical separations using super-resolution microscopy." *Annual review of physical chemistry* 2018, 69, 353-375.

1.1. Motivation

The National Academy of Sciences of the United States recently reported that 15% of the total energy consumption in the United States is allocated to chemical separations (Figure 1.1).¹ Chemical separations are critical for maintaining our quality of life, industrial energy production, and sustaining our nation's role as a leader in innovative technologies. As a result of the importance purifications and separations carry for our country, the National Academy has established a research agenda that can advance separation and purification processes for a wide array of industries spanning

from food processing, energy storage, and everyday medical products.¹ Separation and purification of promising protein-based therapeutics termed ‘biologics,’ are the focus of the presented work given the large cost and the current gap in knowledge of the complex dynamics of proteins at the interface of separation materials.

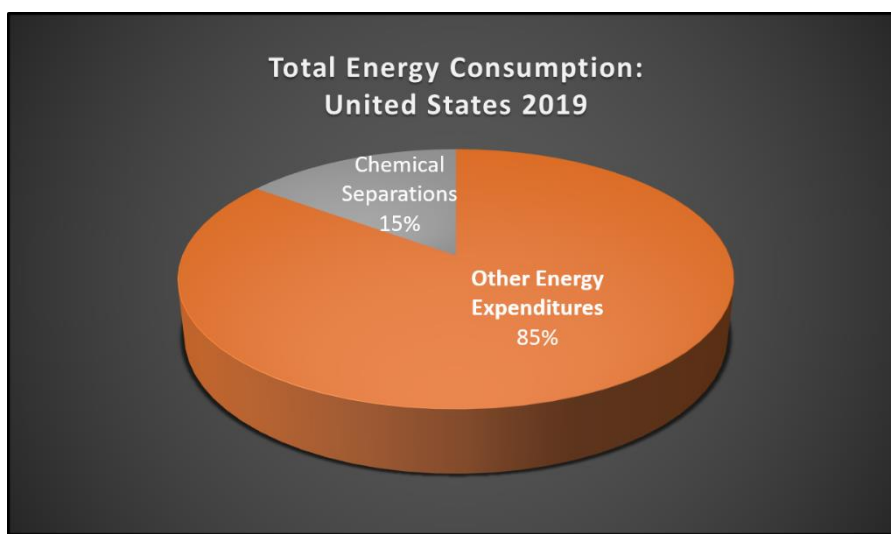


Figure 1.1 Energy expenditure on Chemical Separations in the United States as of 2019.

Biologics have superseded small molecules as the dominant retailed pharmaceuticals in recent years. Specifically, 70% of the top ten retailed pharmaceuticals in the United States were biologics in 2018, in comparison to 0% in 2008 (Figure 1.2).² The high demand for biologics has caused tremendous strain on the purification and separation via chromatography. Challenges associated with the purification and separation of proteins arise from their complex and dynamic structures, which are highly sensitive to environmental conditions such as pH, ionic conditions, and interactions with other proteins.³ Moreover, current models established in the chromatography community lack

mechanistic and predictive capabilities. Advancements in our understanding of these complex systems will lower input costs, minimize the costs to patients, and lower energy consumption.

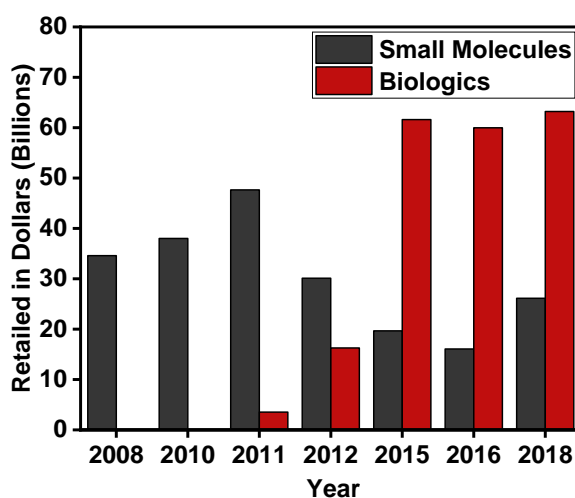


Figure 1.2 Comparison of small molecules vs. biologics within the top ten retailed pharmaceuticals in the United States reported in billions of dollars from 2008 to 2018.²

The heavy use of biologics in patient therapies has placed a large financial burden on the manufacturing and production of promising biologics, increasing the cost of patient care. As of 2015, introducing a promising ‘biologic’ to market cost ~\$2.6 billion,⁴ of which ~50% can be attributed to separation and purification.⁵⁻⁷ Chromatography is heavily used from lab-scale refinement to downstream industrial purification of proteins.⁸⁻¹⁰ With worldwide medical use of biologics only increasing,^{2,11-12} it is time to address the mismatch between the status quo of empirical separations and the need for predictive separations at both benchtop and industrial scales. The lack of predictive

separations can be attributed both to the complexity of the underlying physics and chemistry – hampering computation and experimental analyses – with ensemble assays such as adsorption isotherms masking underlying heterogeneity.¹³⁻¹⁴

The effort to analytically model separations began as early as the 1920s.¹⁵⁻¹⁶ To date, however, there is still no comprehensive theory to link the multiscale dynamic processes occurring in a chromatographic column to observable elution profiles. Instead, users at the laboratory and industrial scales are left to rely on oversimplified empirical equations.¹⁷ More elegant theoretical advances made as early as the 1950s¹⁸ were not adapted for the simple reason that there was no experimental way to link the underlying physics to a quantifiable observable. The advent of single-molecule and super-resolution methods in particular, makes it possible to extract the theoretical parameters driving chromatographic separations.

1.2. Background

Super-resolution microscopy¹⁹ and single-molecule imaging²⁰ are noninvasive tools that quantify and image the multifaceted components present in protein separations.²¹ Super-resolution microscopy is a robust field enjoying rapid improvements in spatial resolution,²² temporal resolution,²³ and the increased complexity of samples that can be studied.^{19-20,24-25} Access to nanoscale dynamics is often challenging with traditional techniques,²⁶ but readily achieved with super-molecule microscopy. Single-molecule methods allow for individual fluorescently labeled proteins to be monitored in real-time with a high spatiotemporal resolution, thereby capturing dynamics in a high throughput fashion.^{24,27-29} Additionally, super-molecule techniques monitor molecules

exploring heterogeneous local environments that are often averaged with ensemble experimental techniques.³⁰

Providing an experimental framework to motivate theoretical developments towards advanced chromatographic models is necessary for optimizing separations. Single-molecule imaging quantifies rare subpopulation interactions often averaged in traditional measurements.³¹ Rare interaction types are important for elution profile shapes, particularly in determining the origin of tailing and/or fronting observed in elution profiles.³² Access to kinetic and dynamic information of rare interactions can have important implications for designing efficient separations. Therefore, we use single-molecule imaging methods to further develop the fundamental understanding of protein-polymer interactions present in separation systems.

1.3. Specific Aims

The goal of this project is to utilize single-molecule imaging methods to relate nanoscale phenomena on polymer support materials to observables in real chromatographic separations. It is important to develop a relationship between surface chemistries, polymer chain physics, and ionic conditions to interfacial protein interactions at the interface of polymer materials. The following aims are completed to achieve this goal.

1.3.1. Aim 1: Relate surface chemistry modalities at industrial relevant polymer support to nanoscale protein dynamics

Utilize TIRF microscopy to image the dynamics of a model protein, lysozyme, at the interface of chemically oxidized polystyrene films. Surface chemistries, surface roughness, and surface hydrophilicity of the films are related to hindered continuous-time random walk (CTRW) dynamics of lysozyme.

1.3.2. Aim 2: Establish a relation between single-molecule dynamics to theoretical and ensemble improvements in separation efficiencies under salting out conditions

Investigate improved efficiencies in ensemble fast protein liquid chromatography (FPLC) of a protein, transferrin, and relate improvements to super resolved single-molecule dynamics and kinetics. Further, single-molecule kinetics are used to inform Monte Carlo based simulations that predict improvements in separation efficiencies confirming trends observed in FPLC.

1.3.3. Aim 3: Link the suppression of anomalous surface diffusion of a model protein to the free volumes present in thin polymer films

Perform single-molecule tracking of alpha-lactalbumin (α -LA) and Lys at polystyrene (PS) films with varied free volumes modulated via molecular weight, thermal annealing, and adjusting solvent quality. Hindered CTRW dynamics are directly related to the free volumes present in the PS films. Hindered CTRW dynamics are hypothesized to be driven by hydrophobic interactions.

1.4. Overview

Chapter 2 presents a scientific and historical background to fluorescence based single-molecule spectroscopy and chromatographic separations. Also, previous research is discussed that led to the development of the above specific aims.

Chapter 3 contains work relevant to Aim 1. The transport dynamics of a globular protein, Lys, are quantified at the surface of chemically oxidized polystyrene interfaces. It was observed that the CTRW exhibited by Lys is hindered as a result of all oxidative treatments. However, the oxidative state and chemical identities of surface chemistries that formed stronger water hydration layers results in greater hindrance of Lys dynamics. This work was published in *Langmuir*.

Chapter 4 contains work relevant to Aim 2. The interfacial kinetics and dynamics of a well-studied protein, transferrin, was quantified under varied ionic conditions to emulate salting out processes heavily utilized in industrial biologic purification. Single-molecule kinetics and structural changes to transferrin are related to improved separation efficiencies in ensemble FPLC experiments with varied ionic conditions. Lastly, Monte Carlo simulations informed by single-molecule kinetics predict improved separations. This work connects single-molecule observables to real separation efficiencies confirmed by theoretical predictions for the first time. The work presented in this chapter was published in the *Proceedings of the National Academy of Sciences of the United States*.

Chapter 5 contains work relevant to Aim 3. The surface dynamics of Lys and α -LA are quantified at PS with varied free volumes modulated via molecular weight, thermal annealing, and adjusted solvent quality. α -LA was highly immobile on the

surface of PS regardless of the film conditions, but surface residence times did depend on the MW of the PS. The free volume of the underlying film had a direct effect on the observed anomalous diffusion of Lys. More specifically, as free volumes decreased so did the mobility and step size distributions. This work is currently under review for publication in *Langmuir*.

Chapter 6 contains a conclusion for Chapters 2-5 including future outlooks on single-molecule microscopy as a tool for advancing separation sciences.

Chapter 7 contains supplemental data and analyses for Chapters 2-5.

|Chapter 2

Background

^α Portions of this Chapter are reproduced with permission from published work:

Moringo, Nicholas A., Hao Shen, Logan D.C. Bishop, Wenxiao Wang, and Christy F. Landes. "Enhancing analytical separations using super-resolution microscopy." *Annual review of physical chemistry* 2018, 69, 353-375.

2.1. Abstract

This chapter provides the background of single-molecule imaging that enables the localization of single fluorescently labeled proteins below the diffraction limit of light. Included is a brief discussion of the widefield microscopy techniques implemented in this work. Lastly, a brief background of chromatography is discussed followed by a survey of other's work studying interfacial protein-polymer interactions at the single-molecule level, which motivates the work presented here.

2.2. Origin and Advancement of Single-Molecule imaging

All the work discussed and presented here utilizes the phenomena of fluorescence to image, localize, and track individual molecules.³³ Fluorescence is the emission of light from a compound that has absorbed photons from a light source, thereby promoting electrons in the molecule to excited electronic states.³³ A Jablonski diagram illustrates possible absorption transitions and decay pathways for electrons with respect to the electronic energy levels of that molecule (Figure 2.1).³⁴ Molecules can be excited with specific wavelengths of light that match the energy required to promote an electron from the ground state to an electronic excited state (Figure 2.1, $S_0 \rightarrow S_1$), following the Frank-Condon principle.³⁵⁻³⁶ After excitation, the electron will often decay to the lowest vibrational energy state within the electronic excited state, formally known as Kasha's Rule,³⁷ before decaying radiatively (fluorescence) or non-radiatively (internal conversion or IC) shown in Figure 2.1. The fluorescence emission is red shifted (i.e. Stokes shift³⁴) in relation to the excitation wavelength due to the energy loss that occurs during the vibrational relaxation outlined by Kasha's rule.³⁷ Sequential photon absorptions can also occur as denoted as excited state absorption (ESA) in Figure 2.1. Lastly, intersystem crossing (ISC) can also occur when the spin state of the excited electron enters a triplet state ($S_1 \rightarrow T_1$) and then decays via phosphorescence (radiative) or via IC (non-radiative) (Figure 2.1). However, the time scale over which an electron decays from the singlet state in comparison to the triplet state is five orders of magnitude faster at times. Therefore fluorescence is often the most dominant decay pathway for most dyes.³³ Additionally, advanced dye molecule designs have improved quantum efficiencies over large spectral regimes that favor fluorescence emission.³⁸⁻³⁹ Dye molecule improvements that allow for

more photons to be emitted per unit time are advantageous for improved signal in imaging and localizing molecules of interest.

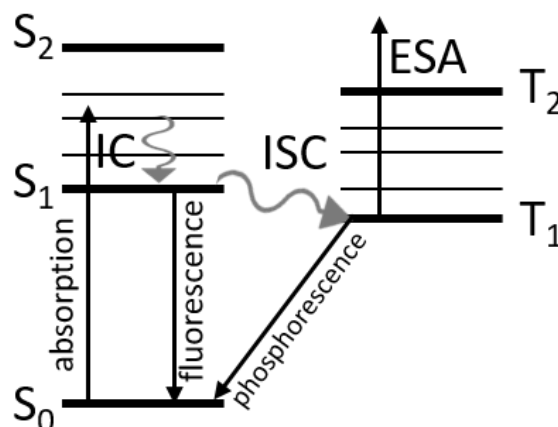


Figure 2.1 Jablonski Diagram.

The spatial resolution of a traditional microscope is limited to the diffraction limit of light due to the wave-like behavior of light. The inherent localization resolution limit of a point emitter was described by Ernst Abbe in 1873⁴⁰ in Equation 2.1:

$$d = \frac{\lambda}{2NA}$$

Equation 2.1 The Abbe diffraction limit of light.⁴⁰

The Abbe equation relates d , the distance over which two light-emitting points can be resolved (i.e. spatial resolution), to the wavelength (λ) of light emitted from the source. Further, the resolving power of the objective (NA) used to image the emitters also determines a microscope's overall spatial resolution. A commonly used benchtop

microscope would usually be equipped to provide a ~ 200 nm spatial resolution.⁴⁰

However, with the advancement in optics, sensitive photodetectors, and imaging processing techniques the spatial limits of microscopy have pushed the resolution beyond the Abbe diffraction limit.

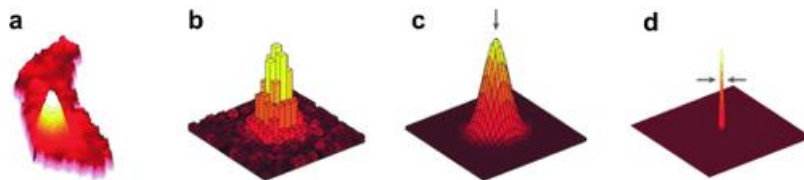


Figure 2.2 Super-localization using point spread function (PSF) fitting for nanometer spatial resolution. (A) The PSF of a single molecule in a bacteria cell. (B) 2D histogram of pixels counts for PSF in (A). (C) 2D Gaussian used to fit PSF in (B). (D) Final localization of the center of mass of the Gaussian function used in (C). Reproduced with permission from *Angewandte Chemie Intl. Edition*.

In 2014, Betzig,⁴¹ Moerner,⁴²⁻⁴³ and Hell⁴⁴⁻⁴⁵ received the Nobel Prize in Chemistry⁴⁶ for advancing the field of microscopy with methods that push the spatial resolution of imaging single fluorescent emitters to tens of nanometers. Two general approaches were developed as a part of the 2014 Nobel Prize. One approach fits the point spread function (PSF), the camera's response from a single emitter known as the "airy disk"⁴⁰, with a 2D Gaussian to determine the lateral location of an emitter down to a few nanometers shown in Figure 2.2.⁴²⁻⁴³ This method is applied to many fluorescing molecules separated in both time and space to reconstruct complex structures.⁴¹ The second approach utilizes two excitation sources, one laser bleaches emitters in a ring-like area about a region of interest, while the other laser excites the emitter of interest. Both

approaches aim to lower emitter density across a sample by either the stochastic photophysics of fluorescence or depleting emitters in a region of interest with a light source. Additionally, as the number of photons emitted by a fluorescent molecule increases, the localization accuracy increases by decreasing the FWHM of the emitters PSF. Further developments and methods for super-resolving emitters including PAINT,⁴⁷ STORM,⁴⁸ and PALM,³⁸ which can super resolve complex structures depicted in Figure 2.3. New advancements in imaging have pushed the limits of localization to three dimensions,⁴⁹ improved the temporal resolution for capturing fast dynamics,²³⁻²⁴ and increased the complexity of systems studied.⁵⁰⁻⁵³

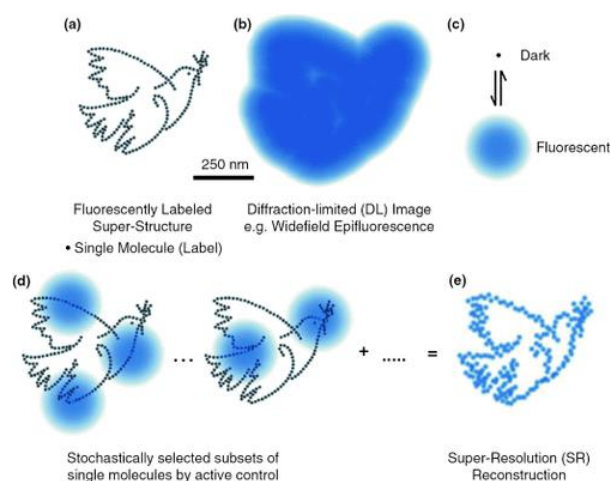


Figure 2.3 Fundamentals of super-resolution reconstruction imaging. (A) Ground truth image with black dots representing single dye molecules. (B) Image captured exciting all emitters at a time resulting in a diffraction-limited image. (C) Photoswitching dyes emission (D) stochastically exciting sparse subsets of emitters during each camera exposure. (E) Final reconstructed image by fitting each emitter's PSF and determining localization below the diffraction limit of light over many camera frames. Reproduced with permission from *Angewandte Chemie Intl. Edition*.

Many microscopy techniques exist that enable single-molecules to be tracked below the diffraction limit of light in complex systems. Active feedback confocal based methods utilize point detectors and closed feedback loop systems to track a single-molecule over large axial and lateral ranges with a temporal resolution of milliseconds to even microseconds.⁵⁴⁻⁵⁶ Although active confocal methods are very versatile and useful for providing dynamic information about a molecule of interest, these methods lack the throughput to study interfacial phenomena.⁵⁷⁻⁵⁸ Also, multiple detectors, lasers, and costly piezo stages are needed to successfully implement these methods in a microscope setup. Widefield microscopy has throughput high enough to study interfacial dynamics at the interface of separation support materials at a lower cost.

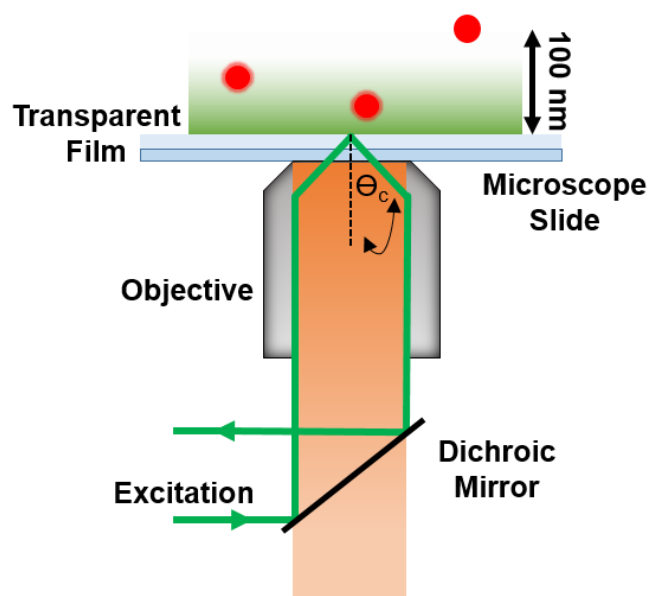


Figure 2.4 Typical through objective widefield total internal reflection fluorescence microscope setup.

Widefield microscopy allows for a large area in sample space to be imaged on a camera. The fundamental difference in the illumination geometry when comparing confocal to widefield is that the back aperture of the objective is filled with a collimated light source during confocal imaging. Confocal geometries result in a small confocal volume being illuminated in sample space. Comparatively, in widefield illumination schemes, the light source is focused at the back aperture of the objective causing a large illumination area at the sample once light passes through the objective (Figure 2.4). Total internal reflection (TIR) geometries are ideal in widefield imaging to study interfacial single-molecule interactions (Figure 2.4). The focused light source is aligned to the edge of a high numerical aperture objective creating an evanescent field that propagates from the interface of refractive index mismatch roughly 100 nm into sample space, shown with the green gradient in Figure 2.4.⁵³ TIR occurs as a result of light refracting through media of different refractive indices as outlined by Snells Law in Equation 2.2:

$$n_1 \sin \theta_1 = n_2 \sin \theta_2$$

Equation 2.2 Snell's Law.⁵⁹

TIR often occurs at an incident angle of 69 degrees for high numerical aperture objectives.³² The incident angle (i.e. critical angle, Θ_c , Figure 2.4) required for TIR can be analytically derived based on the refractive indices of the media a user is imaging through using Equation 2.2.⁶⁰ TIR geometry uniquely prevents emitters diffusing in the bulk from being imaged, allowing only light emitted from closely interacting molecules to reach the detector of the microscope. High numerical aperture oil immersion objectives

are advantageous for widefield based single-molecule imaging due to their high angle light-collecting capabilities that result in improved FWHM of PSFs (Equation 2.1). Additionally, the refractive index of immersion media on the objective must match that of the refractive index of glass to satisfy the requirements for TIR to occur from the interface of the material of interest. Thus, it is also ideal to study polymer materials that have a refractive index close to that of oil immersion media ($n=1.51$) and coverslip materials ($n=1.51$). Overall, widefield fluorescence imaging is a robust microscopy method that enables for the high throughput acquisition of single molecules exploring large areas of an interface.

2.3. Previous single-molecule studies at heterogeneous surfaces

Single-molecule techniques close the knowledge gap between empirically established chromatographic theories with molecular scale experimental observables (Figure 2.5). Molecular scale details are acquired by directly monitoring individual analyte molecules, allowing access to inter-site heterogeneities thought to be a major contributor to fronting and tailing in chromatographic separations.⁶¹⁻⁶³ Kisley et al. investigated molecular-scale ion-exchange chromatography by utilizing fluorescently tagged α -lactalbumin and engineered agarose supports as a model system.³² α -lactalbumin is a globular protein that carries a net negative charge under neutral pH and agarose is a common porous support for the separation of biomolecules. For the experiments, agarose surfaces were functionalized with amide-containing ligands that carry net positive charges, thus forming a model ion-exchange system. Total internal reflection (TIR) widefield microscopy was used to observe the adsorption and desorption

of proteins at ligand-functionalized sites on the stationary phase, while mobile phase diffusion (diffusion coefficient $\sim 150 \mu\text{m}^2/\text{s}$) was too fast to be observed. The experiments achieved a sub-diffraction localization precision of $\sim 30 \text{ nm}$ by fitting each adsorption event with a 2D Gaussian function and extracting its spatial position as the centroid. Experimental details of the super-resolution experiment and analysis can be found in an extensive review of the subject.^{20,64} Super-localization, coupled with kinetic analysis, made it possible to distinguish between specific, repeat protein adsorption at ligand sites and nonspecific adsorption due to trapping within pores on the agarose support (Figure 2.5A).

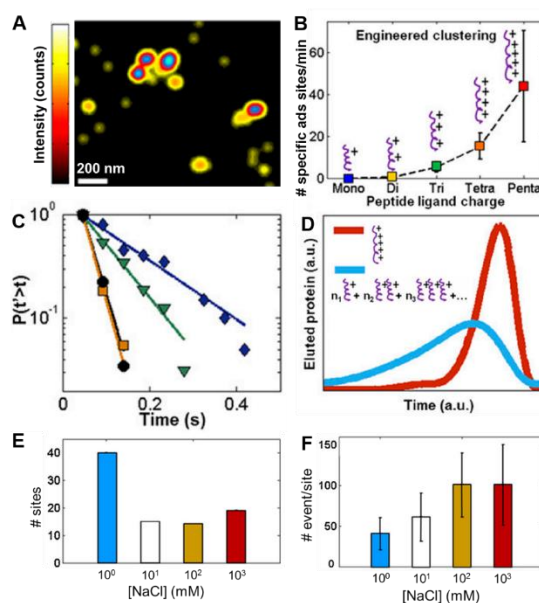


Figure 2.5 Super-resolved α -lactalbumin adsorption and desorption at clustered ligands on agarose. (A) Specific adsorption sites are quantified by identifying single adsorption events in each image frame. (B) Adsorption frequency dependence vs. ligand cluster size. (C) Cumulative distribution of α -lactalbumin residence times at different ligand sites. (D) Ensemble averaged elution profiles for engineered ligand clusters (603 sites, red) and stochastically clustered ligands (1,706 sites, cyan) on functionalized agarose

supports. (E, F) Ionic strength dependence of the number of specific adsorption sites (E) and total adsorption events per site (F). Adapted with kind permissions from the National Academy of Sciences ³² and 2014 Elsevier.⁶⁵

One of the most important conclusions reached by the early super-resolved protein adsorption studies is that stochastic ligand clustering on the agarose support causes heterogeneity in protein adsorption-desorption kinetics (Figure 2.5B-D). As suggested by previous theories,⁶⁶ adsorption heterogeneity leads directly to broadening of the macroscale elution time. The experiments showed that the underlying kinetics and associated macroscale elution profiles could be narrowed by engineering optimized ligand clusters (Figure 2.5B).³² Adsorption and desorption times were extracted at the single site level by analyzing the waiting times between adsorption events and the residence times before desorption, respectively. Interestingly, even with optimized engineered ligand clusters, intersite heterogeneity for both adsorption and desorption was still observed (Figure 2.5C).

$$\phi(\omega) = \exp \left[i\omega t_m + t_m \int_0^{\infty} \exp[i\omega\tau - 1] M(d\tau_s) \right]$$

Equation 2.3 Lévy spectral function.

Using the Lévy representation expressed above in Equation 2.3, the distribution of protein desorption times were correlated to the ensemble elution profiles. Further comparison between the engineered sites versus stochastically formed sites indicated that the HETP might be reduced by as much as 5 times by optimizing ligand clustering.³² A

mathematical description of the separation efficiency was derived by converting the Poisson distribution of dwell times, extracted experimentally, to the frequency domain relationship expressed in Equation 2.4:

$$\phi(t_s; \omega | t_m) = \exp \left[r_m \sum_{i=1}^{i=k} ((\exp[i\omega\tau_{s,i}] - 1) \Delta F(\tau_{s,i})) \right]$$

Equation 2.4 Poisson distribution of dwell times.

In Equation 2.4 Poisson distribution of dwell times., t_s is the time spent in the stationary phase while t_m is the time spent in the mobile phase, r_m is the number of times a protein adsorbed during time t_m , and k is index of the discrete set of desorption times. The elution profile can be extracted from a single surface adsorption site with this equation. By taking all the specific adsorption sites into consideration and generating the site averaged elution profiles, the difference between the stochastically clustered monoargininamide and pentaargininamide was obvious: the stochastically clustered monoargininamide resulted in more severe peak broadening while the pentaargininamide exhibited a narrow Gaussian distribution with mild fronting (Figure 2.5D). The theoretical plate heights were calculated by taking the ratio of the variances of the Gaussian fits to the peaks. It was found that the plate height of pentaargininamide functionalized agarose was five times lower than the clustered monoargininamide functionalized counterpart, indicating that the separation efficiency in chromatography can be largely improved if proper surface engineering is performed.

The intersite kinetic heterogeneity in both adsorption and desorption (Figure 2.5C) was later related to steric availability of ligand sites within the agarose stationary phase to the analyte proteins.⁶⁵ Super-resolution imaging and kinetic analyses demonstrated that increasing ionic strength both decreased heterogeneity in agarose pore size and narrowed the available sites on which proteins were observed to adsorb.⁶⁵ Sodium chloride, with a concentration ranging from 1 to 1000 mM, was added to the solution to adjust the ionic strength of the mobile phase. It was found that the number of specific adsorption sites was significantly reduced at increased salt concentrations (Figure 2.5E), consistent with the notion that screening of electrostatic interactions by salt can eliminate most weakly accessible binding sites. On the other hand, the number of protein adsorption events at each remaining ligand site slightly increased with salt, inconsistent with a purely electrostatic effect (Figure 2.5F). Control experiments (not shown) suggested that instead, shrinking and narrowing of agarose pore sizes was also an important contributor to the observed protein-ligand interactions.

In ion-exchange separations, tuning ionic strength is a commonly used empirical parameter to optimize chromatographic elutions by influencing charge-charge interactions without significant effects on protein denaturation.^{13-14,67} Specifically, it is well established that high ionic strength in the mobile phase can reduce apparent adsorption heterogeneity leading to higher eluting capabilities in ion-exchange chromatography.⁶⁸⁻⁶⁹ However, the super-resolution and single-protein kinetic analyses discussed above demonstrate that the mechanisms driving the macroscale elution are more complex than can be explained by electrostatics alone. Simulation of macroscale

elution profiles using Equation 2.4 predicted that separation could be enhanced by three-fold by suppressing steric heterogeneities among ligands.⁶⁵

Super-resolution studies, in addition to revealing the effects of ligand clustering and steric availability on specific adsorption at ligands, also provide insight about nonspecific protein adsorption to the stationary phase support. Although specific adsorption sites are the dominating factor in the elution, contributions from nonspecific adsorption sites cannot be neglected. For example, the Wirth group and others have shown that rare, but long-lived adsorption to defects on silica stationary phases can have an outsized impact on the ensemble behavior.⁷⁰⁻⁷³ Shen et al. studied the adsorption of α -lactalbumin onto thin nylon 6,6 films using wide-field single-molecule spectroscopy.⁵³ The rate of protein adsorption was determined by counting the number of new adsorbed events per unit time per unit surface area. Under steady-state solution conditions, the rate of adsorption was found to be dependent on the time of adsorption and the protein concentration in the bulk solution. Super-resolution imaging analysis revealed that the surface adsorbed protein molecules were at discrete nonspecific binding sites, which implied a monolayer adsorption model. A kinetic model was proposed allowing for extraction of the site-averaged rate constants for adsorption-desorption and the total number of adsorption sites on nylon surfaces. Comparing the protein adsorption on flat and porous nylon 6,6 films revealed that the porous structures increased the number of adsorption sites by four-fold, however the adsorption processes became less energetically favorable. Use of steady-state kinetic analyses can provide quantitative evaluation of the role of nonspecific adsorption on chromatographic performance.

Another important consideration when applying super-resolution methods to quantify adsorption and desorption dynamics is the limited temporal resolution of modern CCD detectors. The recently developed Super-Temporal Resolution Microscopy (STReM) by Wang et al. demonstrated that it is possible to achieve time resolutions up to 20 times faster than common camera frame rates.²⁴ This simple improvement allows for improved abilities to resolve fast events that are important in chromatographic separations^{21,74}. The current detectable events have a lower bound of a few milliseconds, imposed by the camera frame rate. STReM adopts a concept from compressive sensing that makes it possible to encode fast sub-frame spatiotemporal information within a single frame.²⁴ STReM is achieved by placing a double-helix phase mask (DHPM), originally designed for compressing 3D information into a 2D image,⁷⁵⁻⁷⁷ into the optical detection path and rotating it at constant speed.²⁴ Doing so encodes sub-frame information into the orientations of the final double-helix point spread functions (DH PSFs). The angular frequency is adjusted such that the DHPM rotates 180 degrees in one frame, thus the angle of the DHPM in a single frame encodes its sub-frame position. Using both simulated and experimental methods, it was shown that STReM can be applied to analytes that exhibit fast adsorption-desorption kinetics, short sub-frame surface residence times, and even undergo sub-frame 2D transport.²⁴ For the latter two scenarios, the resulting PSFs are complicated and sophisticated analysis algorithms must be employed for data recovery.²⁷ Nevertheless, STReM is capable of enhancing the effective temporal resolution by 20 times in all three cases and resolving protein desorption kinetics that would not be observed with traditional camera capabilities.²³

Single-molecule and super-resolution methods have recently revealed that protein adsorption-desorption can be coupled to additional processes that are not well described by simple physical models.²¹ Kisley et al. studied the α -lactalbumin adsorption at a silica substrate, a model system for aqueous normal phase and hydrophilic interaction chromatography.⁷⁸ Two linked modes of interaction were observed by single-molecule tracking under low pH conditions: adsorption-desorption and surface diffusion (Figure 2.6A). It was suggested that such diffusive dynamics are a culmination of electrostatic, hydrophobic, and hydrogen bonding interactions.

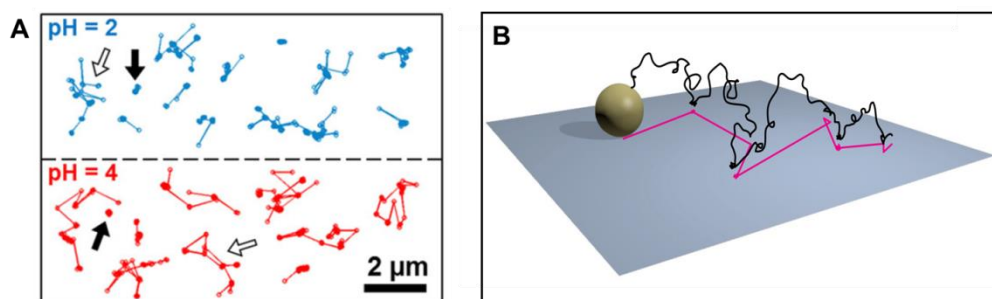


Figure 2.6 Imaging complex protein motion on chromatographic supports. (A) Example trajectories of α -lactalbumin proteins exchanging at a silica support under two pH conditions. (B) A schematic illustration of one proposed type of motion, desorption-mediated continuous time random walk. Adapted with kind permission from John Wiley and Sons⁷⁸ and the American Physical Society.⁷⁹

Schwartz and coworkers have systematically studied protein interactions at various interfaces⁷⁹⁻⁸⁰ and proposed the interaction could be modeled as a desorption-mediated continuous time random walk (CTRW). Here, a CTRW means that analyte molecule in the mobile phase intermittently hops through the bulk solution before

stochastically immobilizing to a binding site for a variable amount of time (Figure 2.6B).⁷⁹ Because the available adsorption sites are heterogeneous in binding energy, the waiting time of the CTRW is a broad distribution that can only be expressed by a power-law. CTRW were widely observed over polymer matrices,⁸¹⁻⁸² oil-water interfaces,⁸³⁻⁸⁴ and functionalized substrates.⁸⁵⁻⁸⁷ These are usually considered as model substrates in reverse phase liquid chromatography, normal phase chromatography, and ion-exchange chromatography.^{70,73} The preceding work suggests that protein adsorption-desorption at even the simplest chromatographic supports can be much more complicated than the equilibrium adsorption-desorption implicit within Langmuir adsorption models, but that super-resolution methods are useful for distinguishing, quantifying, and tuning the processes.

2.3.1. Protein Unfolding at Stationary phase support materials

Reorganization of a protein's structural motif directly alters the intrinsic behavior as the protein's size, geometry, overall charge, and exposed chemical domains are altered, thus introducing additional mechanisms to influence elutions.⁸⁸⁻⁸⁹ Dynamic protein unfolding is a rich and complex field all on its own, but it is important to consider the unique information that can be provided by single-molecule and super-resolution studies at stationary phase surfaces. Importantly, single-molecule techniques allow for single proteins to be monitored in real time, thereby elucidating variations in dynamics of structural changes and surface dynamics and revealing heterogeneities otherwise hidden.

Single-molecule Förster resonance energy transfer (smFRET) is a technique that can be combined with single particle tracking in order to measure nanometer sized structural changes occurring in a protein during periods of transport and immobility at an

adsorption site. FRET relies on non-radiative energy transfer, inversely proportional to the distance between two fluorescent probes, to measure distance changes on the order of nanometers.⁹⁰⁻⁹³ smFRET has been powerful in the investigation of protein structures at the single-molecule level in many systems discussed thoroughly elsewhere.^{51,94-98} The ability to interrogate conformational dynamics of proteins with molecular scale precision has also been the result of advancements in fluorescent labeling techniques and methodologies covered by Weiss⁹⁹ and Yang.¹⁰⁰ More recently, researchers have utilized smFRET combined with single-protein tracking to investigate protein dynamics at the interfaces of chromatographic support materials, uncovering mechanistic cues in protein unfolding pathways present in separation systems.¹⁰¹

Kaar and coworkers were the first to employ tracking smFRET to monitor protein conformational changes during interfacial adsorption, desorption, and surface diffusion dynamics.¹⁰² This work determined that two first-order kinetic pathways exist for the model protein organophosphorus hydrolase (OPH) to unfold on a fused silica (FS) interface. It was observed that if OPH unfolded during its trajectory at the FS interface it could readily desorb regardless of OPH's structural conformation during the initial adsorption. These findings provide proof that unfolded proteins can reversibly adsorb to an interface and likely result in solution-phase protein aggregates.¹⁰³⁻¹⁰⁴ Kaar et al. were the first to show direct molecular level evidence of this phenomenon, which likely serves as an initiation step in interfacial fouling. Studies indicate that fouling is predicated by the accumulation of unfolded proteins in the mobile phase of separation systems.¹⁰² This work highlights the strong potential of tracking smFRET to discern dynamics from conformational subpopulations of proteins during

adsorption-desorption processes at stationary phase supports, as well as to uncover the large discrepancy among protein unfolding timescales. Such details would traditionally not be accessible by ensemble based measurements. Single-molecule measurements found evidence of transformations on the order of tenths of seconds, compared to hour long transformations detected by ensemble measurements. This discrepancy in time scales is likely due to ensemble measurements monitoring the relative rates to which unfolded and folded populations are changing in comparison to the unfolding processes of individual proteins in real time.¹⁰²

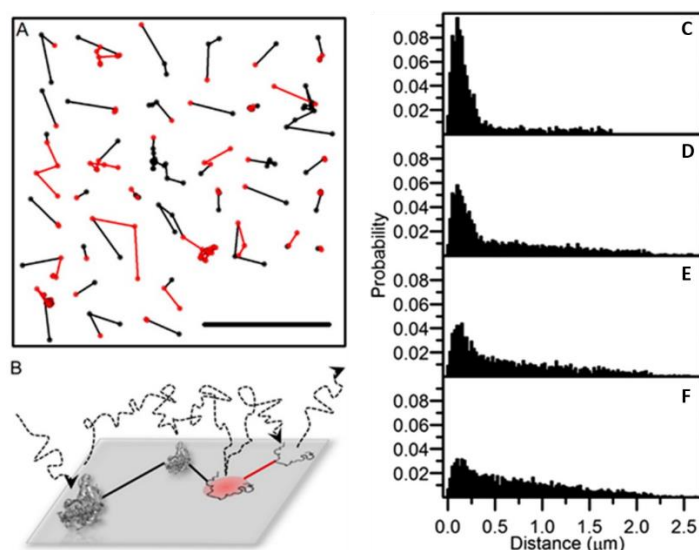


Figure 2.7 Lysozyme adsorption-unfolding dynamics on a fused silica support.

(A) Representative trajectories of single lysozyme proteins undergoing a “search” process for unfolding sites on FS interface. Black segments of each trajectory represent the folded lysozyme state and red segments indicate unfolded conformation. (B) Cartoon representation of proposed model behind surface induced unfolding of lysozyme at unfolding sites. (C-F) Distributions of trajectories Euclidean distance before first detected unfolding event at total lysozyme concentrations of: (C) 1.0×10^{-10} M, (D) 1.5×10^{-9} M, (E) 5.5×10^{-9} M, and (F) 7.1×10^{-8} M. Labeled lysozyme concentrations were held constant in C-

F. Scale bar in (A) represents 5 μm . Adapted with the kind permission of the American Chemical Society.¹⁰⁵

Further insights into unfolding and transport dynamics of proteins at industrially relevant support materials have been provided by tracking smFRET¹⁰⁶. Weltz and coworkers investigated the transport and unfolding dynamics of a model protein lysozyme at a fused silica support¹⁰⁵. Tracking and unfolding trajectories shown in Figure 2.7A elucidated that lysozyme explores large amounts of the interface prior to unfolding. Lysozyme exhibited a surface transport behavior consistent with a CTRW¹⁰⁷⁻¹⁰⁸ containing distinct hopping and waiting periods between adsorption sites along the support (Figure 2.7B). Weltz and coworkers determined that a rare subpopulation of adsorption sites exist on the support that induces lysozyme unfolding (Figure 2.7B).¹⁰⁵ In this study, the effective concentration of labeled lysozyme was fixed while the amount of unlabeled lysozyme in the solution was increased incrementally in each experimental condition (Figure 2.7C-F). It was determined that increasing the effective concentration and surface coverage of lysozyme caused labeled lysozyme molecules to explore larger distances on the support prior to unfolding on the surface (Figure 3.1C-F). As a result of increasing the effective lysozyme concentration, the number of strongly adsorbing sites and the number of adsorptions at these sites decreased, thereby decreasing heterogeneity in the lysozyme-FS interactions. The decrease in heterogeneity was attributed to unlabeled lysozyme molecules passivating the surface at higher effective concentrations. Tracking results also highlighted that increasing the unlabeled lysozyme concentration caused the labeled lysozyme population to exhibit longer flights between adsorption sites and shorter waiting times between flights. These findings suggest that passivated support

materials give rise to less heterogeneity in surface residence times of adsorbed protein molecules and likely can mitigate resulting peak broadening in separation systems.

Ultimately, this work highlights the importance of adsorption site heterogeneity and its direct role on protein unfolding and surface transport dynamics at support materials.

As discussed earlier, achieving greater temporal resolution is also important for understanding protein unfolding at a stationary support, given that unfolding dynamics can occur on fast timescales.¹⁰⁹⁻¹¹¹ Though tracking smFRET provides high throughput acquisition of the unfolding and transport mechanics of model proteins, non-tracking smFRET techniques can provide a greater temporal resolution. For example, confocal based smFRET can achieve a microsecond temporal resolution.¹¹² However, confocal smFRET exhibits lower throughput due to a smaller inherent imaging area. Saito and coworkers utilized a confocal based technique in order to uncover the unfolding dynamics of ubiquitin at a polymer coated support.¹¹² A covalent polymer coating was used to suppress artifacts originating from adsorption at the interface of the microfluidic assembly. The introduction of the hydrophobic polymer allowed for near surface protein conformations to be measured with high temporal resolution. smFRET results indicated that ubiquitin exhibits a large heterogeneity in conformational states when unfolded. However, ubiquitin exhibits a well-defined structure while undergoing near surface diffusion in the folded state. Interestingly, ubiquitin's structural changes in the unfolded states occurred on a time scale longer than 1 millisecond.¹¹² These results provide insight into the complex nature of protein dynamics at wide array of timescales unique to each protein and stationary phase.

Developing a more thorough understanding of protein unfolding dynamics at support interfaces is essential to optimizing separations through robust bottom-up design. The utility of smFRET to investigate real time single protein structural changes during surface transport at separation support materials has been discussed above. Advancements in labeling techniques, sensitive photon detectors, and experimental designs has allowed smFRET to be utilized in probing a large array of protein-surface interactions in real time. Although tradeoffs do exist between tracking and non-tracking smFRET techniques, both provide access to fine details in the delicate and dynamic structural changes that occur in a protein while diffusing through separation systems. These techniques can be extended to more support materials and proteins to build on the already impressive fundamental understanding of the multifaceted processes of protein unfolding.

2.3.2. Competitive protein dynamics

The target analyte protein is often only one of many proteins present in a separation column, providing another layer of complexity through potential protein-protein interactions. For example, mobile phase interactions as well as competitive adsorption-desorption processes at stationary phase can play a role in the overall performance of a separation system, though very little is known about the mechanistic details at the single protein level. Many ensemble based techniques have been utilized to investigate protein-protein interactions in a variety of systems and have been discussed thoroughly by Phizicky and Fields.¹¹³ In addition, a range of experimental¹¹⁴⁻¹¹⁵ and theoretical studies¹¹⁶⁻¹¹⁷ have explored how multiple proteins competitively adsorb to an interface. These processes are highly dynamic and play an important role in the

separation of target proteins from upstream byproducts. Protein-protein and competitive protein adsorption effects should be investigated with single-molecule techniques in the future to develop a mechanistic understanding of these processes. Recently, Kisley et al. reported that insulin competitors in the mobile phase blocked α -lactalbumin adsorption at some ligands, but had no influence on adsorption/desorption kinetics at sites where adsorption did occur, an unexpected result that certainly motivates further experimental and theoretical examination.⁵²

2.3.3. Protein transport super-localized under nanoconfinement

Chromatographic separations utilize porous stationary phase materials that introduce many complex paths for proteins to explore during elution. Porous surface features are often heterogeneous in size, density, and overall surface morphology¹¹⁸. Protein translation and rotation within pores can be hindered under nanoconfined conditions. This complexity presents a challenge to experimentally quantify structure-function relationships present in separation systems. Porous polymer supports are increasingly commonplace because of their low fabrication price, chemical stability, and ease of surface functionalization¹¹⁹⁻¹²¹. Studying protein interactions with porous supports via super-resolution microscopy provides structural details of porous networks and dynamic information about protein transport simultaneously.

The development of non-invasive techniques to report structure-function relationships in separation systems is essential to the development of function specific support materials. Advanced imaging techniques such as atomic force microscopy and scanning electron microscopy are able to image porous structure with nanometer scale

spatial resolution. However, these methods can damage delicate polymer materials during image acquisition and have limited functionality in quantifying dynamics under the aqueous conditions necessary for protein separations.¹²² In particular, porous supports can reversibly swell and shrink in the changing ion-exchange solution conditions.¹²³ An ideal experimental technique would provide *in situ* imaging of porous supports in tandem with single-molecule tracking, allowing insights into the relationship between underlying structure of support materials and analyte protein transport dynamics.¹²⁴⁻¹²⁵ Of particular utility is the recently developed fluorescence correlation spectroscopy Super-Resolution Optical Fluctuation Imaging (fcsSOFI) method.¹²⁶

fcsSOFI enables both the porous substrate morphology and particle transport kinetics to be simultaneously quantified by relating fluorescence fluctuations due to hindered diffusion within a pore to the size of the pore.¹²⁶ fcsSOFI has the potential to provide rich sub-diffraction information in environments where emitter signals are low and/or in confined spaces.¹²⁷⁻¹²⁹ Mathematically, fcsSOFI generates a high-resolution image of the porous support from an autocorrelation map.¹³⁰ The super-resolved image is calculated from the second order autocorrelation of each pixel. Each point spread function (PSF) in the second order autocorrelation map is spatially enhanced by a factor related to the diffusion coefficient (Equation 2.5):

$$G_2(r, \tau) \sim \int dr_1 U(r - r_1) \times \left[U(r - r_1) \otimes \exp\left(-\frac{(r - r_1)^2}{4D\tau}\right) \right] \varepsilon_1 \varepsilon_2$$

Equation 2.5 fcsSOFI second order autocorrelation spatial enhancement with relation to diffusion coefficient.

in which $U(r)$ represents the PSF distribution, ε_1 and ε_2 are the constant brightness of an emitters in two consecutive frames, D denotes the diffusion coefficient from fluctuation correlation spectroscopy (FCS), and \otimes is convolution operation. The PSF in the autocorrelation map is enhanced to a spatial resolution below the optical diffraction limit (Equation 2.6):

$$\frac{1}{\sigma_{new}^2} = \frac{1}{\sigma_{xy}^2} + \frac{1}{\sigma_{xy}^2 + nD\tau}$$

Equation 2.6 Spatial resolution of final fcsSOFI image.

in which n is a constant determined by the dimensions of the emitter movement, τ represents a time lag, and σ is the standard deviation of the PSFs Gaussian. The resolution of fcsSOFI image is thus improved by a factor between 0 and $\sqrt{2}$.

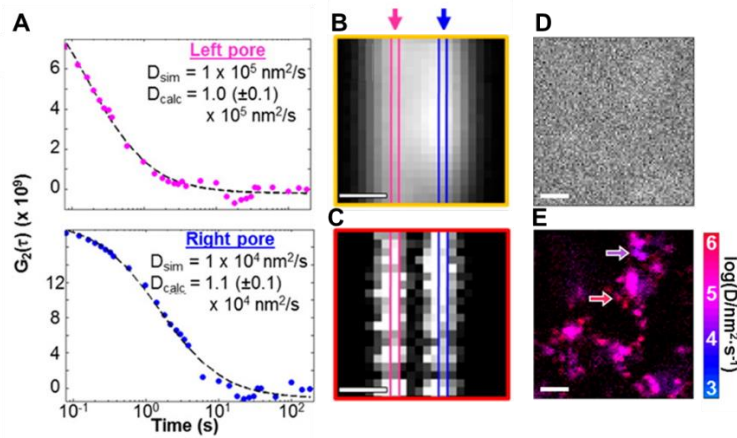


Figure 2.8 Relating pore structure and analyte transport using fcsSOFI. (A) Extracting diffusion coefficients from simulated 1D diffusion with fcsSOFI. (B) Simulated frame-averaged image of emitter diffusion in two pores located within the diffraction limit of each other. True pore positions are labeled by the arrows. (C) The pore structure resolved with 2nd order fcsSOFI calculation

and one step of blind deconvolution. (D - E) Diffusion coefficient distribution and pore size from diffraction-limited image and fcsSOFI image, respectively, of 1% agarose structure. (B - E) Scale bar = 2 μm . Figure adapted from American Chemical Society.¹²⁶

Kisley et al. demonstrated the utility of this technique in both simulated and experimental systems.¹²⁶ In this work, a 1D transport simulation is performed and the pore structure is recovered with a high spatial resolution. Figure 2.8A illustrates how the diffusion coefficient is calculated by fitting the autocorrelation curve. Results are compared to ground truth data and achieve an error under 10 percent. Second order autocorrelation allows for spatial resolution beyond the optical diffraction limit (Figure 2.8B) and can be used to recover the substrate structure (Figure 2.8C). Experimentally, Kisley applied fcsSOFI to image a porous agarose support as a model system due to its use as a stationary support in separation systems. As compared to the raw image (Figure 2.8D), fcsSOFI images can resolve heterogeneities in agarose pore size and related them to transport dynamics of analytes within the pores (Figure 2.8E). The ability to resolve both the porous structure of agarose and the dynamics of an emitter in an aqueous environment was an essential advancement in resolving real time transport in these complex support materials. In the same work, fcsSOFI was successfully applied to resolve the structure of lyotropic liquid crystal gels using perylene diimide as the reporter molecule, achieving results not obtainable with traditional single particle tracking (SPT). Versatility and robustness of fcsSOFI suggests it will form an essential tool in developing a fundamental understanding of structure-function relationships underlying separations at porous supports.

2.3.4. 3D imaging and tracking and novel point spread functions

A method of directly measuring a protein's interaction in porous supports with high axial and lateral spatial resolution would provide unprecedented details about protein separation systems. Three-dimensional protein transport in porous materials is not completely captured with other types of super-resolution imaging because all output images and diffusion maps are projected onto a 2D plane. In comparison, 3D super-resolution microscopy is a powerful tool for studying protein kinetics on porous substrates^{19,76,131} and can be achieved using multi-focal plane microscopy,¹³²⁻¹³³ astigmatic imaging using a cylindrical lens,¹³⁴⁻¹³⁵ light-sheet fluorescence microscopy,¹³⁶⁻¹³⁷ or DH PSF microscopy.⁷⁵⁻⁷⁶ Here, we focus on DH PSF 3D microscopy originally proposed by Pavani and Piestun⁷⁷ as a route for providing high spatial resolution and localization of fluorescent emitters in 3D. We emphasize this technique because of its simplistic implementation in existing microscopy setups, high spatial localization capability, and larger axial range compared with other 3D super-resolution microscopy techniques.¹³⁸ DH PSF microscopy provides three dimensional localization of a fluorescent emitter by the addition of a 4f system¹³⁹ and a phase mask⁷⁷ in the detection path of a traditional microscope (Figure 2.9A). The addition of the phase mask within the 4f system causes the 2D Gaussian PSF (Figure 2.9B, upper) to be converted to a DH PSF (Figure 2.9B, lower) which has two lobes. The orientation of the two lobes encodes the depth of the emitters. Doing so provides a spatial resolution of ~20 nm in both the lateral and axial dimensions.⁷⁶

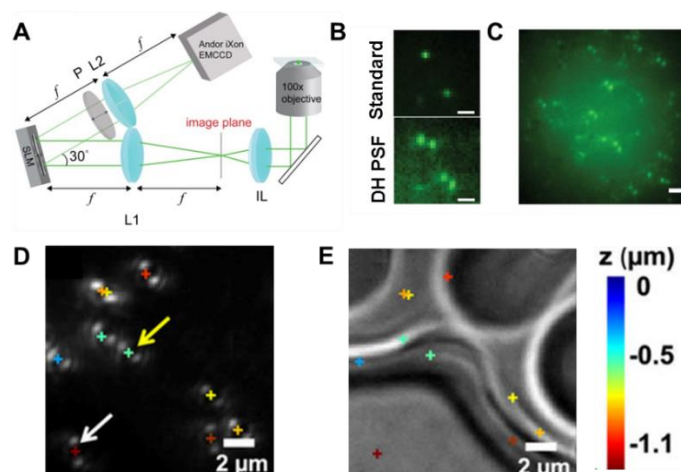


Figure 2.9 Application of DH PSF microscopy to study porous support structure. (A) Scheme of double helix PSF 3D microscopy. (B) Representative data of standard PSF and double helix PSF. Scale bar = 2 μm . (C) DCDHF-P molecules diffusing in thick PMMA polymer substrate. Scale bar = 2 μm . (D) Localization of fluorescent beads in 3D on porous polystyrene film by fitting the DH PSFs. (E) Overlay of fluorescent bead 3D localizations on the bright field image of porous polystyrene film. Figures (A - C) are adapted from National Academy of Sciences⁷⁶ and (D - E) are adapted from Scientific Reports.²⁷

3D SPT is a powerful tool to provide more insight into the interaction of molecules on a porous substrate. Pavani and coworkers first applied DH microscopy to track DCDHF-P fluorophore molecules in the thick PMMA polymer surface (Figure 2.9C).⁷⁶ They reported that the diffusion of single fluorescent emitters can be distinguished in 3D below the diffraction limit.⁷⁶ In addition, Shuang et al. studied the adsorption and desorption of fluorescent beads on porous polystyrene films.²⁷ Varied orientation of the DH PSF lobes encodes adsorption site depths (Figure 2.9D). Overlaying the single-molecule localizations on a bright-field image of the underlying porous surface provided confirmation of the axial resolution of this technique on porous

polymer supports (Figure 2.9E). Improved resolution in three dimensions makes DH microscopy an invaluable tool in the analysis and investigation of porous media.

Recently, the improved temporal resolution from rotating the DH PSF allows for the encoding of sub-frame information into 2D images.²³ Wang et al. showed that rotating the DH PSF 180 degrees during a frame exposure uncovered protein desorption kinetics not resolved with the traditional time resolution of other single-molecule techniques.²³ Non-rotating PSF results only showed a single exponential time of residence times, whereas the improved temporal resolution of STReM resolved a second desorption pathway that was sequential from the surface of nylon films.²³ In addition to improved time resolution recent work has shown that 3D localization and subframe temporal information can be achieved with unique PSF design utilizing newly developed PM design algorithms.

Developing a PM pattern that produces a desired final PSF is a computational challenging phase retrieval problem,¹⁴⁰ where you are recovering the signal in the Fourier domain from the amplitude in the spatial domain.¹⁴¹ Wang et al. established a Gauss-Newton algorithm that recovers phase mask patterns for a desired final PSF design with high efficacy.²⁵ This algorithm was then utilized to develop a powerful stretching double lobe PSF that enables 3D tracking below the diffraction limit of light while compressing sub-frame temporal information into the final 2D image.²⁵

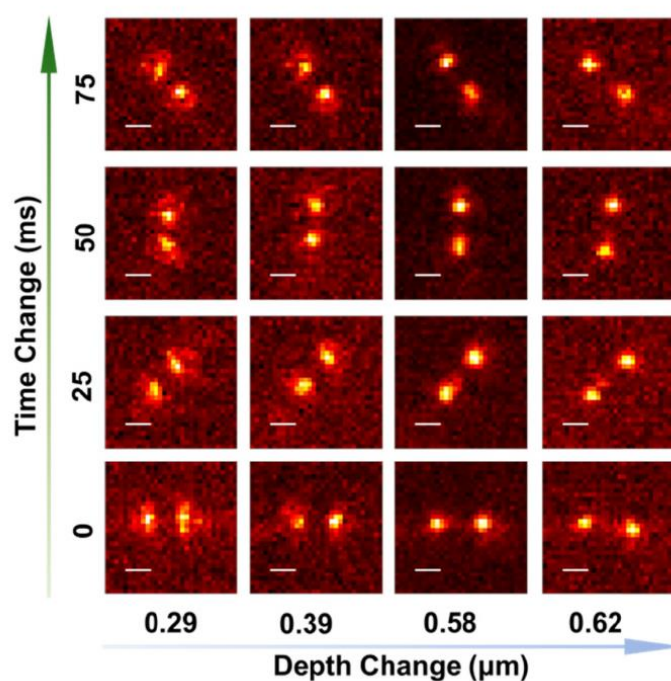


Figure 2.10 Application of the stretching lobed PM. The orientation of lobes encodes arrival time shown on the y-axis. Axial emitter location is encoded by the distance between the lobes shown on the x-axis. Reprinted with permission from *OSA publishing*.

3D localizations and sub-frame arrival times are achieved by rotating the phase mask 180 degrees within one integration time.²⁵ As shown in Figure 2.10²⁵ the distance between the two lobes encodes the axial location of the emitter, while the angle of the two lobes encodes the emitter's arrival time at the interface. This allows for the lateral, axial, and sub frame arrival times to be retrieved from a 2D image captured on a scientific camera.²⁵ This novel stretching-lobe PSF can be utilized to further motivate studies into the highly multiscalar dynamics of proteins within separation systems.

2.4. Conclusion

Here we provide the current outlook of super-resolution techniques and their implementation to investigate the three main phenomena within separation systems: adsorption-desorption dynamics, protein unfolding and competitive protein kinetics, and transport in porous stationary phase media. Super-resolution microscopy's ability to provide mechanistic insights into the heterogeneous behaviors of protein molecules in separation systems, most importantly, to extract parameters that directly relate to a stochastic theory are highlighted here. Super-resolution continues to provide mechanistic insights into the complex components in chromatographic systems, thereby motivating a robust and predictive theory of chromatographic separations.

Variable lysozyme transport dynamics on oxidatively functionalized polystyrene films

¶Reprinted (adapted) with permission (Moringo, N., Shen, H., Tauzin, L., Wang, W., Bishop, L. D.C., Landes, C.F., *Langmuir* 2017, 33, 41, 10818-10828). Copyright (2019) American Chemical Society.

3.1. Abstract

Tuning protein adsorption dynamics at polymeric interfaces is of great interest to many biomedical and material applications. Functionalization of polymer surfaces is a common method to introduce application specific surface chemistries to a polymer interface. In this work single molecule fluorescence microscopy is utilized to determine the adsorption dynamics of lysozyme, a well-studied antibacterial protein, at the interface of polystyrene oxidized via UV exposure, oxygen plasma, and functionalized by ligand

grafting to produce varying degrees of surface hydrophilicity, surface roughness, and induced oxygen content. Single molecule tracking indicates lysozyme loading capacities and surface mobility at the polymer interface is hindered as a result of all functionalization techniques. Adsorption dynamics of lysozyme depend on the extent and the specificity of the oxygen functionalities introduced to the polystyrene surface. Hindered adsorption and mobility is dominated by hydrophobic effects attributed to water hydration layer formation at the functionalized polystyrene surfaces.

3.2. Introduction

Elucidation of mechanistic details of modified polymer properties and their role in protein rich environments is essential to advancements in many fields of scientific importance including biological nanoarray sensing,¹⁴²⁻¹⁴⁵ biomedical transplants,¹⁴⁶⁻¹⁴⁸ and industrial drug purification.¹⁴⁹⁻¹⁵¹ Protein surface transport dynamics at modified polymer interfaces are complex and often dictate the efficacy of these systems.³⁰ However, studying the complex interactions between these macromolecules is often challenging due to the dynamic structural motifs,^{152,153} heterogeneous modes of transport^{154,155} and varying chemical properties exhibited by proteins and polymers.^{30,145} Oxidative functionalization of polymers has been an area of great interest given the ability for oxygen containing functionalities to be incorporated into the outermost layers of the polymer while keeping the bulk chemical properties unaffected.¹⁵⁶⁻¹⁵⁹ Moreover, oxidation processes that modify polymer surface characteristics can be tuned to perturb protein adsorption dynamics for

specific applications including membrane antifouling,¹⁶⁰⁻¹⁶¹ cell adhesion,¹⁶² and biocompatibility.^{163,164}

Conventional methods such as quartz crystal microbalance,^{26,165} isothermal titration calibration,^{166,167} and dynamic light scattering¹⁶⁸ reveal important information about average structural and chemical details occurring during protein adsorption, but lack multiscale spatiotemporal resolution and thus suffer from ensemble averaging of underlying macromolecule dynamics. Studying dynamic and heterogeneous interactions using wide-field single molecule fluorescence microscopy allows for high spatial and temporal resolution of single binding events to be monitored in real-time,^{169,170} uncovering mechanistic details of these complex systems in a high throughput fashion. Advancements in labeling methods, optical microscopy, and tracking algorithms^{24,27-28} allow single molecules to be tracked within complex environments.^{171,172} For example, mechanistic detail about intracellular protein transport,¹⁷³⁻¹⁷⁶ adsorption processes along chromatographic interfaces,^{21,32,65,78,124,177-178} and protein adsorption dynamics at polymeric interfaces^{53,85,179-181} have been revealed using wide-field single molecule tracking methods.

Excitation of labeled proteins within a small distance (~80 nm) of the interface of interest is achieved by utilizing total internal reflection fluorescence (TIRF) microscopy in which an exponentially decaying evanescent wave is created at refractive index boundaries. TIRF allows for background signal to be suppressed from probes that are not at the interface, and thus is ideal for monitoring dynamic processes occurring at heterogeneous surfaces, such as polymers.^{181,82} Recently the Schwartz group utilized single molecule

TIRF to uncover the presence of slow in-plane diffusion of target molecules undergoing desorption-mediated transport on patterned polymeric interfaces, in addition to reduced mobility along boundaries of varying hydrophilicity.⁸² Moreover, single molecule TIRF was also used to investigate how the structural changes of thermoresponsive polymer brushes effected the surface transport of surfactant molecules.¹⁸² These examples highlight the utility for single molecule spectroscopy to elucidate mechanistic details in complex systems that exhibit heterogeneous surface chemistries.

Here, we implement single molecule TIRF to investigate the interfacial adsorption dynamics of a well-studied antibacterial protein, lysozyme,^{183,184} on polystyrene interfaces that have been oxidized by UV exposure, plasma treatment, and functionalized by ligand grafting resulting in varying degrees of hydrophilicity. Polystyrene is the polymer of interest in this study given its low cost and chemical stability under laser radiation¹⁸⁵ in addition to its heavy use in cell culture dishes,¹⁸⁶ food packing industries,¹⁸⁷ and recent applications in postsurgical wound healing.¹⁸⁸ UV light and oxygen plasma treatments are utilized as two oxidation techniques because these techniques avoid complex wet chemistries and can be readily implemented in commercial polymer functionalization. Lastly, a ligand grafting technique¹⁸⁹ is utilized to directly control the oxygen containing species introduced on the polystyrene interface, in addition to the ligand's biological relevance and compatibility.^{190,191} Binding rates, single frame displacements, trajectory's radius of gyration calculations, and surface residence times are presented in our analysis of lysozyme adsorption dynamics on polystyrene and functionalized polystyrene interfaces. Polystyrene surface characterization was conducted utilizing atomic force microscopy

(AFM), static contact angle measurements, and X-ray photoelectron spectroscopy (XPS) to relate polymer properties to single molecule observables. Each functionalization technique induced unique surface functional groups to the polystyrene interface. Our results indicate that increasing the density and oxidation state of hydrophilic species at the polystyrene interface hinders the mobility of adsorbed lysozyme molecules. Moreover, each treatment technique increased surface roughness and hydrophilicity resulting in lower surface residence times and binding rates of lysozyme. The varied interactions of lysozyme is dominated by hydrophobic effects and the increasing role of hydration layers at polystyrene interfaces functionalized with more polar chemistries.

3.3. Materials and Methods

3.3.1. Polystyrene Film Preparation and Ellipsometry

Glass microscope coverslips (22 x 22 mm, Fisherbrand, borosilicate) were sonicated for 20 minutes sequentially in solutions of: critical cleaning detergent and water (Liquinox), deionized water ($>1 \text{ M}\Omega\cdot\text{cm}$), methanol (Sigma), and acetone (Sigma). The glass slides were then cleaned in a bath of piranha base solution (1:1:5 28% $\text{NH}_4\text{OH}/30\%\text{H}_2\text{O}_2/\text{H}_2\text{O}$) heated at 80°C for 20 min. The coverslips were then dried under a steady stream of compressed nitrogen followed by 2 minutes of oxygen plasma treatment (Harrick Plasma, PDC-32G).

Polystyrene pellets (Sigma-Aldrich, $M_w=36,000$) were dissolved in toluene (Sigma-Aldrich) to prepare a 1.5 w/w% solution of polystyrene. Roughly 50 μL of the

polystyrene solution was deposited onto the center of a cleaned glass slide; then samples were spin coated (SPI KW-4A) at 3000 RPM for 1 minute. The resulting films were used as is for all polystyrene film measurements. The spin coated film thickness (~60 nm) was determined using ellipsometry (Gaertner 7109-C370B, Figure S1) with silicon wafer as the substrate (Silicon Quest Int'l, Prime Grade).

3.3.2. Polystyrene Functionalization

The following three methods were used to functionalize polystyrene films:

3.3.2.1. UV Functionalization

Spin coated polystyrene films were irradiated by a high powered UV lamp (UVP LLC, 365 nm, 100 watt) under atmospheric conditions for 10, 20 or 30 minutes. The spin coated samples were placed roughly 9 cm from the UV lamp during the treatment period. All samples were rinsed under a gentle stream of DI water before all experiments to remove weakly bound polymeric by-products from this treatment technique.

3.3.2.2. Plasma Treatment

Polystyrene films were individually placed in a oxygen plasma cleaner at a fixed position inside the instrument to keep plasma exposure consistent between each treated sample. The plasma cleaner was flashed with oxygen three times prior to treatment for 1, 3, 5 or 7 seconds at ~200 mTorr. All samples were rinsed

under a gentle stream of DI water before all experiments to remove weakly bound polymeric by-products from this treatment technique.

3.3.2.3. Ligand Grafting

Ligand grafting was induced by UV light exposure using a two-step process adopted from Ma and coworkers.¹⁸⁹ A 10 w/w% solution of benzophenone/acetone was prepared and 100 μ L of the resulting solution was deposited onto the polystyrene film surface and irradiated for 1 minute with a UV lamp. The film surface was then rinsed thoroughly with acetone in order to remove unreacted benzophenone from the film. Following this 100 μ L 10 w/w% solution of Allyl α -D-galactopyranoside (Sigma)/DI water was added to the benzophenone treated surface and irradiated for various treatment times of 5, 10, 20 or 30 minutes. The films were then rinsed with deionized water thoroughly and dried under a stream of compressed nitrogen gas.

3.3.3. Wide-field Single Molecule Fluorescence Microscopy

Single molecule fluorescence measurements were conducted on a custom TIRF wide-field microscope (Figure 1A). Excitation light was generated by a 532 nm diode laser (Coherent, Compass 315M-100SL) and focused at the back edge of a high numerical aperture oil-immersion objective (100 \times N.A. 1.45 Alpha Plan-Fluar, Carl Zeiss) to achieve TIR, corresponding to an angle of incidence $\sim 78^\circ$. An exponentially decaying evanescent field was produced as a result of achieving the TIR condition thereby exciting only probes within ~ 80 nm of the interface. Emitters located within the evanescent field but not

interacting with the interface are not detected due to motion blur. The power density used for all measurements of this work was 0.10 kW/cm^2 at the interface. Fluorescence was collected using the same objective (epifluorescence) and passed through a $2.5\times$ lens followed by a dichroic mirror (Chroma z532/rpc633). The emission light then passes through a notch filter (Kaiser, HNPF-532.0-1.0) and a band pass filter (Chroma, ET585/65m), after which the illumination area ($30 \times 20 \text{ }\mu\text{m}^2$) was projected onto an EMCCD camera (Andor, iXon 897). The EMCCD was operated with an integration time of 30 ms and an electron multiplying gain of 300 in frame transfer mode for all measurements. The resulting setup allows for a $600 \text{ }\mu\text{m}^2$ area to be monitored at the polymer interface producing high throughput data acquisition. Data was collected in stacks of 1,000 frames (30 seconds) with a ~ 1 minute delay between consecutive movies. Each sample was measured for 6,000 frames in one region and was illuminated for 45 minutes at 0.20 kW/cm^2 before data collection to photobleach any contaminants in the films reducing background signal. At this power density laser induced oxidation of the polystyrene is unlikely to occur given power densities orders of magnitude greater are needed to oxidize polystyrene.¹⁹² Probe solutions (100 μL) were drop cast onto the films and immediately measured thereafter in a controlled environment with a relative humidity of 55%. The density of emitters on the polystyrene interface did not change over time for represented measurements. A previously published tracking algorithm was used to construct trajectories from single molecule data (details in SI).²⁸

3.3.4. Protein Preparation

Lysozyme C labeled with Rhodamine B (Nanocs, Figure 1C-D) served as the probe molecule used in this study. All protein solutions were prepared in 10 mM HEPES Buffer (Sigma, pH 7.1) with probe molecule concentrations at 1.0 nM for all results presented.

3.3.5. Goniometry Measurements

Static water contact angle measurements of all films were conducted using a goniometer (Ramé-hart Model 200) to determine changes in hydrophilicity as a result of various outlined treatment methods. Contact angle measurements reflect regionally averaged hydrophilicities of the polystyrene interfaces given the contact area of the water solution is $\sim 1 \text{ mm}^2$.

3.3.6. Atomic Force Microscopy

Surface roughness characterization of polystyrene and oxidized polystyrene surfaces were conducted using AFM (Bruker, Multimode 8), operated in peak force tapping mode. Silicon tip nitride lever probes (Bruker, Scan Asyst, $f_0 = 70 \text{ kHz}$) with reflective aluminum coating were used to probe respective surfaces. Samples for AFM measurements were prepared using the same protocol as single molecule experiments.

3.3.7. X-ray photoelectron spectroscopy

X-ray photoelectron spectroscopic (XPS) analyses were conducted using a PHI Quantera XPS. The excitation source Al K α X-rays (1486.7 eV) was operated at 40W,

15kV and focused to spot size of 50 μ m diameter. This produces a corresponding sampling depth of ~3 nm. Survey scans were conducted in 0.5eV steps over the 1100–0 eV binding energy range with a pass energy of 140eV. High resolution spectra of C1s and O1s were performed in 0.1eV steps with a pass energy of 26 eV. High resolution scans were used for spectra deconvolution and elemental percent composition analyses.

3.4. Results and Discussion

The introduction of hydrophilic moieties to the polystyrene interface, as a result of oxidative treatment and functionalization, inhibits lysozyme mobility reducing hopping to adjacent binding sites in addition to decreasing binding rates. Each functionalization method caused a decrease in surface residence time for lysozyme molecules that was exacerbated as polystyrene became more hydrophilic. The experimental setup for single molecule data acquisition is shown in Figure 3.1A with the TIR condition occurring at the film-liquid interface. The TIR condition occurs at this interface due to a large refractive index mismatch between the polystyrene ($n \sim 1.58$) and probe solutions ($n \sim 1.33$), rather than occurring at the closely matched glass ($n \sim 1.52$) and polystyrene interface as shown in our previous work studying similar interfaces.^{53,81,85} The TIR condition reduces background signal from emitters in the bulk solution not interacting with the polystyrene interface. Representative lysozyme trajectories (1,000 frames) on polystyrene are shown in Figure 3.1B. The structures for polystyrene, lysozyme, and the fluorescent label with counter-ion are shown in Figure 3.1C-D from left to right respectively. Lysozyme is highly mobile on the surface of polystyrene, exploring large amounts of the surface with long-lived

trajectories indicated by the time-dependent color gradient in Figure 3.1B. The dynamic mobility of lysozyme has also been observed by other on hydrophobic surfaces.¹⁹³ Given the high throughput nature of our data acquisition, single molecule trajectories are acquired from many regions of a sample allowing our results to reflect the lysozyme-polystyrene interactions at the ensemble level. However, single molecule techniques allow us access to subpopulations of lysozyme-polystyrene interactions occurring at the heterogeneous polymer interface.

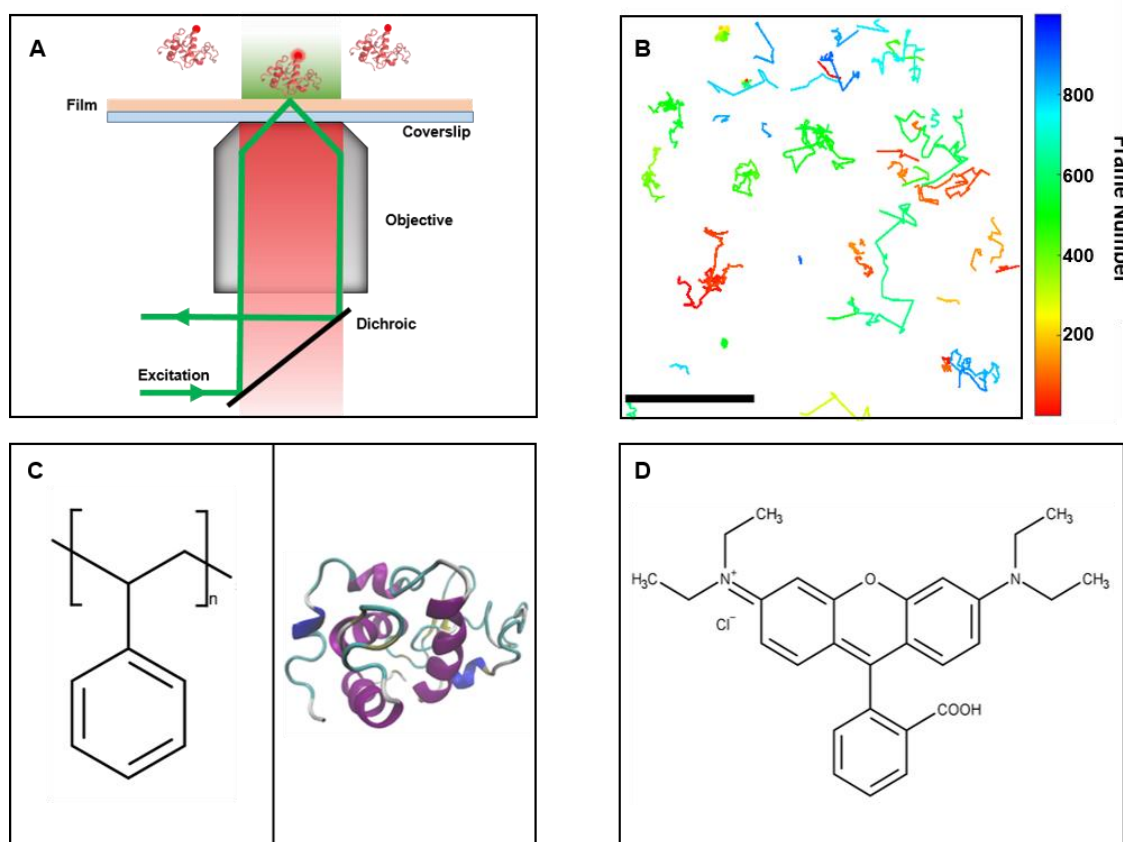


Figure 3.1 Experimental setup using a TIRF excitation geometry. Evanescent wave depicted in the excitation of Rhodamine-B labeled lysozyme probe with maximum evanescent intensity at the film-liquid interface. (B) Representative

time-dependent lysozyme trajectories from 1,000 frames of data on as prepared polystyrene film with camera integration time of 30 ms (Scale bar is representative of 2 μm). (C) Structure of polystyrene and structure of lysozyme (PBD: 4Z98, hen egg white lysozyme¹⁸³) with secondary structural motifs indicated by various colors (left to right). (D) Structure of Rhodamine B dye with counter-ion.

3.4.1. UV Treatment

Exposing polystyrene films to UV light increases the film hydrophilicity while the lysozyme adsorption binding rate and surface mobility decrease, but all are independent of exposure time (Figure 3.2). Contact angle measurements (Figure 3.2A, Figure S3) show that UV exposure increases hydrophilicity, but not in a tunable fashion. The increase in hydrophilicity with UV exposure is likely caused by the mild oxidation of the polystyrene¹⁵⁷⁻¹⁵⁹ interface causing water hydration layers to form,¹⁹⁴ which strongly interact with the polymer interface. The interactions between water and polymer surfaces, which exhibit varying degrees of hydrophilicity, are well studied and indicate that the viscosity and density of water molecules at the interface increases as the surface becomes more hydrophilic with an increase in hydrogen bonding.¹⁹⁵⁻¹⁹⁸

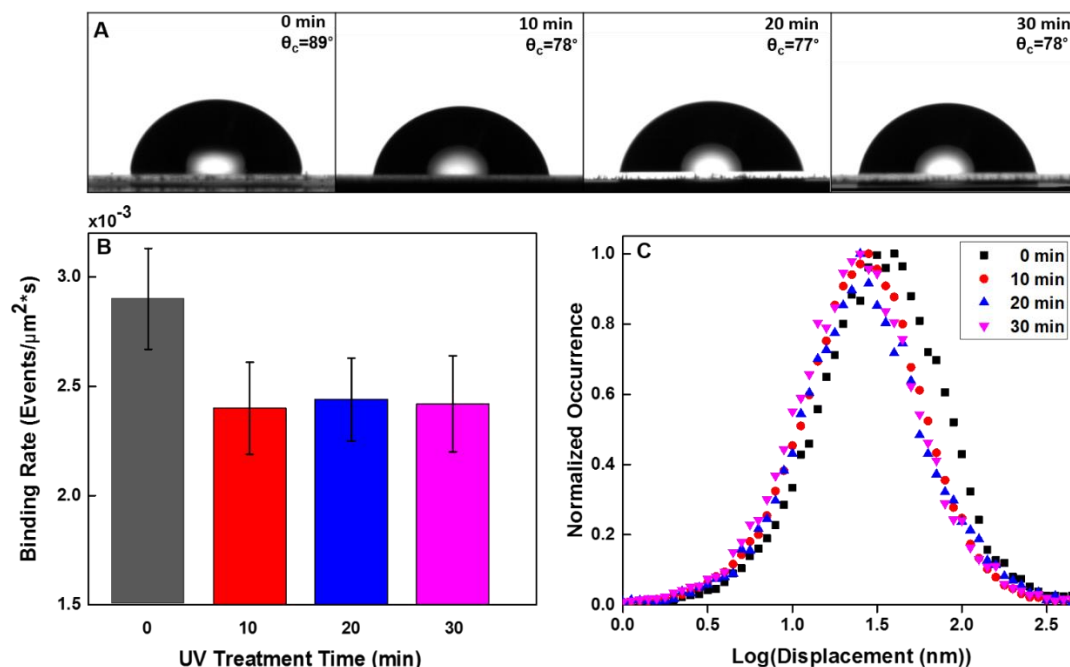


Figure 3.2 Lysozyme adsorption at UV-treated polystyrene interfaces. (A) Static contact angle measurements for polystyrene and UV treated polystyrene films with corresponding treatment times. Lysozyme binding rates (B) and single frame displacements distributions (C) for polystyrene and UV-treated polystyrene (10, 20 and 30 minute treatments). Error bars in (B) represent the standard deviation of the mean from at least 1,600 imaged adsorption events. Each condition in (B, C) represents at least 800 events worth of data.

UV-oxidized polystyrene decreases the binding rate of lysozyme proteins on the polymer surface (Figure 3.2B). The binding rates are determined by taking the average number of new events per frame from 6,000 frames of movies and dividing by the projected surface area ($205 \mu\text{m}^2$). It is well established that hydrophilic interfaces exhibit lower protein loading capacities than hydrophobic surfaces.^{30,199-200} The hydrophilic surface chemistry is thought to hinder lysozyme adsorption as water molecules must be displaced

for the lysozyme adsorption process to occur.²⁰¹ In contrast, lysozyme is highly mobile on the less hydrophilic native polystyrene, exploring large amounts of the surface with long-lived trajectories indicated by the time-dependent color gradient in Figure 3.1B. Inspection of trajectories in Figure 3.1B reveals lysozyme undergoes inter-site hopping along the heterogeneous polystyrene surface interrupted by brief periods of confinement indicative of a desorption mediated transport mode as seen by others at the single molecule level.^{181,82} This mode of non-Brownian surface diffusion is consistent with many other single molecule studies containing single molecule adsorption processes along heterogeneous interfaces and provides mechanistic details not capable of being observed with ensemble based methods.^{81,83-84,202}

The surface mobility is quantified by the single frame displacement distributions in Figure 3.2C. UV-induced oxidation decreases the lysozyme step size as it explores the polymer surface, indicated by the slight shift in the single frame displacements and confirms that smaller magnitude displacements are more likely to occur as the surface is oxidized by UV light. The histograms of displacement (Figure 3.2) represent the magnitude of frame to frame step size produced from single molecule trajectories, which did not produce any time dependent changes in the corresponding distributions for all treatment methods ruling out laser induced surface oxidation effects (Figure S4). Distributions are plotted on a logarithmic scale to represent the entire range of displacements measured for each condition which are lognormal as discussed in our previous work.^{81,85} Cumulative distributions of surface residence times are also compared (Figure S5) for all treatment conditions represented in Figure 3.2, indicating no significant

difference in surface residence times for lysozyme molecules on UV-exposed polystyrene. No changes in contact angle, binding rates, single frame displacements or surface residence times are present as a result of increasing the UV exposure time.

The decrease in step size upon UV treatment observed in Figure 3.2C indicated by the slight shift in the single frame displacement distributions averaged at 46 nm and 40 nm before and after treatment respectively suggests that desorption mediated transport of lysozyme is hindered as a result of surface oxidation. This is likely caused by a decrease in the number of available adsorption sites to which lysozyme can re-adsorb as the hydrophilic surface is more densely hydrated after UV-induced oxidation.²⁰¹ An increase in water density at the hydrophilic polystyrene surface thus induces a decrease in surface mobility. Also, as shown in Figure S6, the lysozyme trajectory's radius of gyration decreases from 74 nm on polystyrene to 54 nm after 10 minutes of UV exposure, further suggesting decreased lysozyme mobility on the oxidized surfaces. The trajectory's radius of gyration value represents the total area explored by a molecule over the evolution of a trajectory, specifically for molecules that exhibit non-Brownian surface transport modes where traditional diffusion coefficients would not adequately describe molecule mobility (Details in SI).^{85,203} Analysis of radius of gyration evolutions for individual trajectories shows periods of surface transport interrupted by random periods of immobility and confinement, indicated by plot slopes of 0 or less (Figure S8).²⁰³ This further confirms the desorption mediated diffusion of lysozyme at polystyrene interfaces (Figure S8).²⁰³

UV-induced oxidation mildly oxidizes the polystyrene, suggested by the relatively small ($\sim 10^\circ$) reduction in contact angle upon exposure. Our results are consistent with the

mild oxidation of the polymer chains with the likely introduction of hydroxyls and ethers.¹⁵⁷⁻¹⁵⁹ XPS analyses further support the mild oxidation of the polystyrene surface with ~1% increase in the oxygen content that did not increase as UV treatment time was increased (Figure S9 and Table S1). UV treatment times shorter than 10 minutes were not used here given the small change in surface oxygen induced to polystyrene (Table S1) and other surface properties discussed later. This mild oxidation did result in a small decrease in the surface residence times of adsorbed lysozyme molecules (Figure S5), likely caused by adsorbed lysozyme molecules undergoing desorption more readily as nearby adsorption sites are occupied by water molecules hydrogen bonded to alcohol and ether functional groups. As a result of water's propensity to hydrate and solvate hydrophilic polymeric interfaces²⁰⁴ the interactions of protein molecules and the interface become perturbed.¹⁹⁹⁻²⁰⁰ Adsorption sites on our polystyrene interface become occupied by water molecules for all surfaces in this work since the interfaces are becoming more hydrophilic. As a result, protein loading capacities of the interface are lowered in addition to hindered surface transport of lysozyme as shown in Figure 3.2. We attribute this effect to the adsorbed lysozyme molecules inability to readily disrupt hydrogen bond networks exhibited by nearby water molecules and adsorption sites. To further investigate the role of oxidation chemistries on lysozyme dynamics, a technique capable of achieving greater and tunable surface hydrophilicities must be employed.

3.4.2. Plasma Treatment

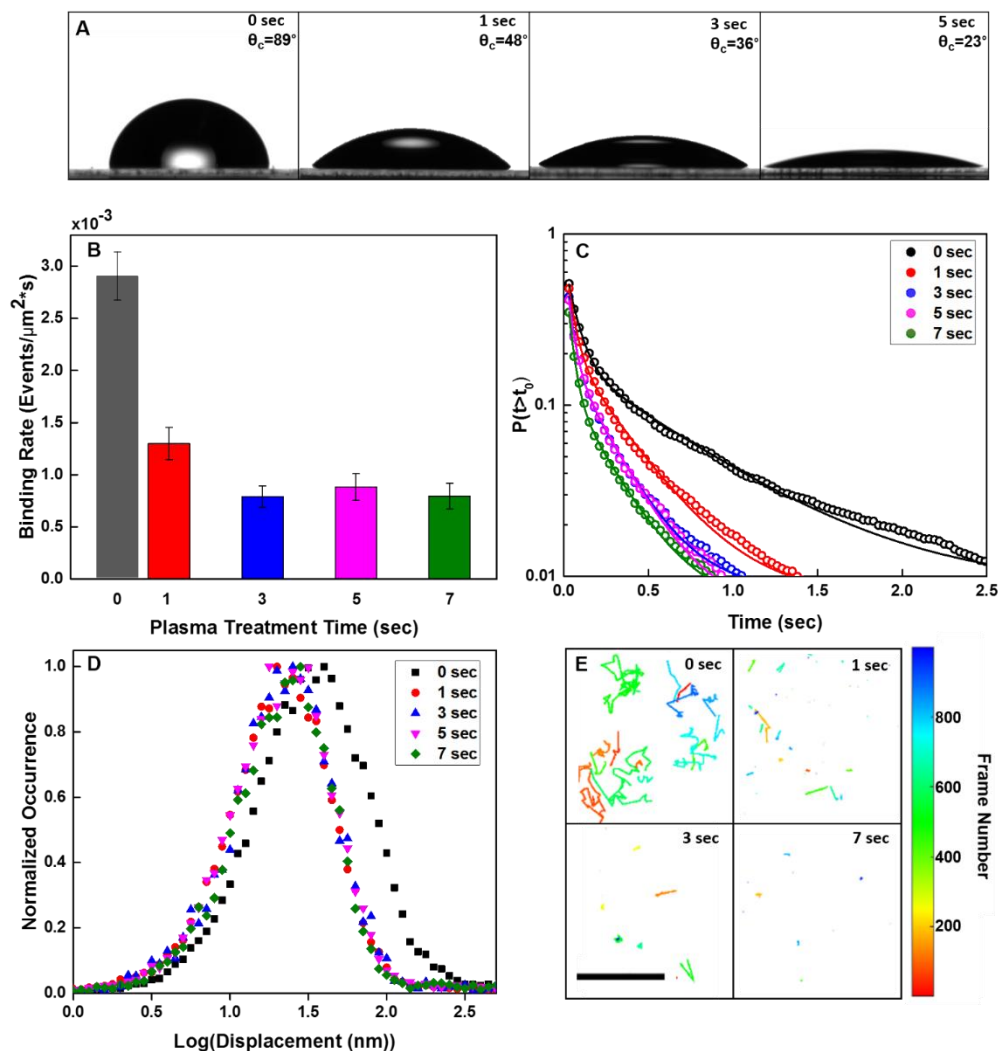


Figure 3.3 Lysozyme adsorption at plasma treated polystyrene interfaces. (A) Static contact angle measurements for polystyrene and plasma treated polystyrene films. **(B)** Binding rates of lysozyme onto polystyrene (0 sec.) and oxygen plasma treated polystyrene. Error bars for each treatment time represent the standard deviation of the mean from at least 1,600 adsorption events. **(C)** Cumulative distributions of surface residence times for respective treatment times outlined in (A). Distributions are fit to the sum of two exponentials indicated by solid lines. **(D)** Single frame displacement

distributions for respective treatment times in (A, B). (E) Representative time-dependent lysozyme trajectories from 1,000 frames of data from treatment times represented in (B-D) (Scale bar is representative of 2 μm). Each condition in (B-D) represents at least 800 events worth of data.

Oxygen plasma treatment of polystyrene allows tuning of surface hydrophilicity and lysozyme surface interactions (Figure 3.3). Increasing plasma treatment time greatly decreases the contact angles of polystyrene (Figure 3.3A, Figure S10) and respective binding rates (Figure 3B). After 1 second of plasma exposure, the contact angle decreases $\sim 40^\circ$, with roughly a two-fold decrease in the binding rate at the oxidized interface. Surface residence times of adsorbed lysozyme molecules also decrease as the surface becomes more hydrophilic (Figure 3.3C), represented as cumulative distributions shown by the Schwartz group³¹ to elucidate rare populations in single molecule adsorption processes. Results indicate that surface residence times of lysozyme can be tuned by varying plasma exposure time. Corresponding distributions are fit with the sum of two exponentials (Figure 3.3C) as previously shown by other biologically relevant single molecule studies,^{172,205} implying biological adsorption phenomena are complex.

Furthermore, lysozyme mobility is greatly hindered with plasma induced oxidation (Figure 3.3D-E). This effect is shown with a shift and narrowing of corresponding single frame displacement distributions shown in Figure 3D. Displacement distributions shifted from an average of 46 nm to 31 nm after 1 second of plasma exposure of did not vary at longer exposure times. Lysozyme immobility is further supported by a decrease in the trajectory's radius of gyration from 74 nm on polystyrene to 37 nm after 1 second of plasma exposure (Figure S11). Representative trajectories for 1,000 frames of varying plasma

exposure times are shown in Figure 3.3E. Visual examination additionally supports a decrease in trajectory step size and lysozyme mobility on the plasma treated polystyrene interface.

Oxygen plasma treatment harshly oxidizes polystyrene and introduces carboxylic and carbonyl moieties to the outmost layer of the film^{156,158,206} supported by increased surface hydrophilicity (Figure 3.3A, Fig S9). Increasing plasma exposure time increases the density and oxidative states of hydrophilic species on the polymer interface. XPS analyses indicate that oxygen surface content increased 10.7% after 1 second of exposure and continued to increase to 19.1% after 7 seconds of plasma treatment (Table S1); therefore lowering the number of accessible adsorption sites for lysozyme as a result of the increasing water-interface interactions via hydrogen bonding and other weak interactions shown by Whitesides and coworkers.¹⁹⁹⁻²⁰⁰ These hydration layer effects are supported with a decrease in binding rates (Figure 3.3B), tunability in the surface residence times (Figure 3.3C), and a decrease in lysozyme mobility (Figure 3.3D-E, Figure S11) at the oxidized polystyrene interface. The unique tunability in surface residence is likely caused by nearby adsorption sites strongly interacting with water molecules thus hindering the reabsorption process as the lysozyme undergoes surface diffusion. The decrease in surface residence times at longer plasma treatment times indicates that adsorbed lysozyme molecules are desorbing more rapidly from the interface. Although adsorption sites do still exist on these highly oxidized surfaces, increasing the density of highly oxidized species along the polystyrene interface hindered the native transport dynamics of lysozyme.

Lysozyme exhibits an overall net positive surface charge at pH of 7.1,²⁰⁷ while the native and functionalized polystyrene interfaces exhibit negative surface charges.²⁰⁸ In order to assess the role of electrostatics in the varied surface interactions seen in the work presented here single molecule experiments were conducted in HEPES buffer solutions of sodium chloride (10 mM and 100 mM) to shield any electrostatic interactions relevant in varied lysozyme dynamics. At these salt concentrations no structural conformational changes to lysozyme have been seen by others.²⁰⁸ No appreciable change in single molecule observables was shown at the polystyrene or functionalized polystyrene (Figure S12). Thus the dominating force in varied adsorption dynamics is likely driven by hydrophobic effects. To explore the role of the specific oxygen containing chemistries to lysozyme surface interactions, a technique that controls the specific species introduced to the surface must be implemented.

3.4.3. Ligand Grafted

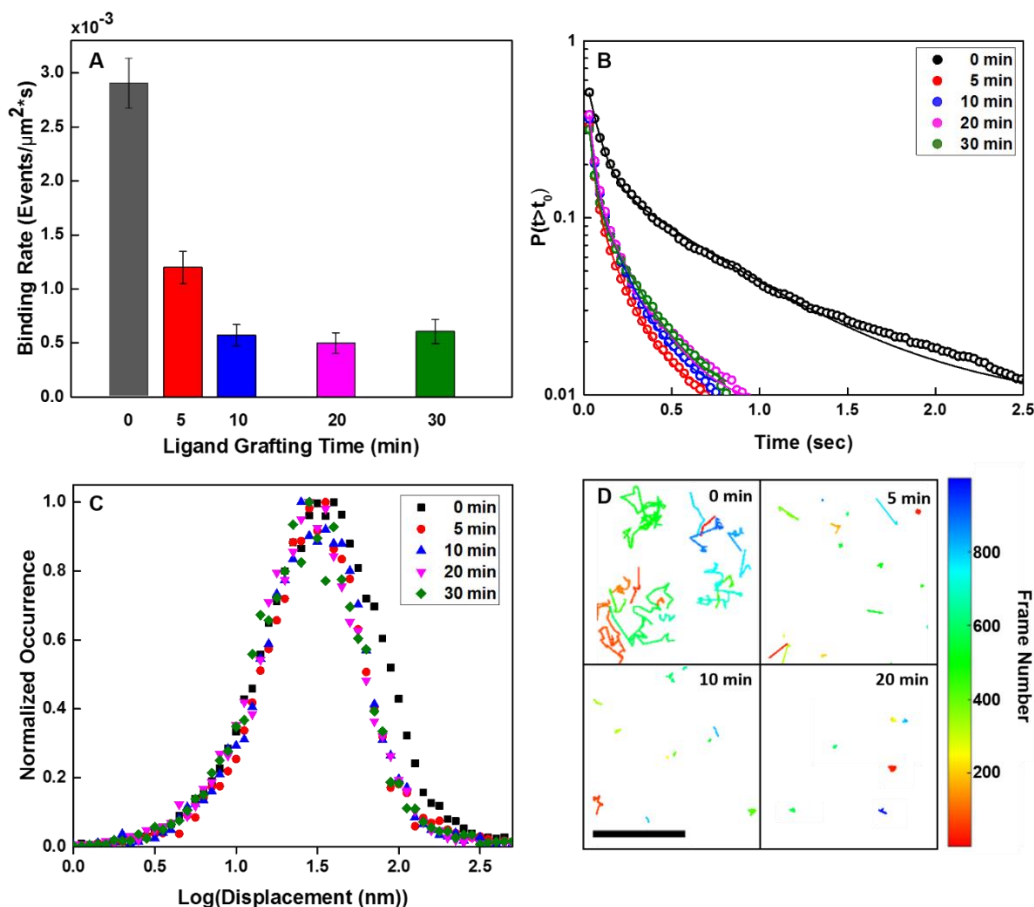


Figure 3.4 Lysozyme adsorption at ligand grafted polystyrene interfaces. (A) Binding rates of lysozyme onto polystyrene (0 min.) and ligand grafted polystyrene. Error bars for each treatment time represent the standard deviation of the mean from at least 1,600 adsorption events. (B) Cumulative distributions of surface residence times for respective grafting times outlined in (A). Distributions are fit to the sum of two exponentials indicated by solid lines. (C) Single frame displacement distributions for ligand grafted polystyrene surfaces represented in (A, B). (D) Representative time-dependent lysozyme trajectories from 1,000 frames of data from treatment times represented in (A-C) (Scale bar is representative of 2 μm). Each condition in (A-C) represents at least 800 events worth of data.

Ligand grafting, in contrast to UV and plasma treatments, gives direct control of the oxygen containing species introduced to the surface (Figure S13) and produces the greatest increase in surface hydrophilicity (Figure S14). The large increase in surface hydrophilicity and wettability induced from this technique is due to the large grafting site density chemically introduced to the polymer surface with corresponding contact angles of less than 5° (Figure S14).¹⁸⁹ XPS analyses indicated that after 5 minutes of ligand grafting an 38% increase in oxygen content was induced to the polystyrene interface (Table S1). The ligand grafting method is comprised of two steps that allow control of the grafting site density and chain lengths individually.¹⁸⁹ Grafting sites are formed in the first step via UV induced radical formation in the presence of the photoinitiator benzophenone. In the second step monomeric units of our ligand polymerize at each grafting site under UV irradiation.¹⁸⁹ Here the grafting site density was held constant and the chain length was increased as grafting time was increased in the second polymerization step.

Results indicate lysozyme adsorption dynamics exhibit grafting time independent and dependent observables (Figure 3.4). As grafting time increases, there is an initial two-fold decrease in the binding rate of lysozyme followed by a gradual saturation (Figure 3.4A). In addition, surface residence times of lysozyme molecules remain unchanged after an initial decrease from the native polystyrene (Figure 3.4B). Lysozyme surface mobility is hindered on the ligand grafted interface, shown with an initial narrowing of single frame displacement distributions (Figure 3.4C) and by visual examination of representative trajectories for various grafting times (Figure 3.4D). Displacement distributions shifted 5 nm from the average of 46 nm on the untreated polystyrene (Figure 3.4C). Surface

confinement of lysozyme is further supported by linear correlation in the trajectory's radius of gyration values as grafting time increases (Figure S15), suggesting the area explored by adsorbed lysozyme molecules can be controlled by varying grafting time.

The decrease in binding rates and surface residence times of lysozyme (Figure 3.4A), is likely the result of chemical and structural effects induced by ligand grafting. As grafting time increases the effects of hydration layers is likely increasing, given that ligand chain length is increased linearly as a function of grafting time introducing more hydrophilic chemistries to the interface.¹⁸⁹ In addition, the steric effects of longer hydrated ligand chains at the polymer interface can restrict the number of accessible adsorption sites for lysozyme. Thus, both effects are feasible for decreasing the rate of lysozyme adsorption. The high saturation of hydrophilic functionalities chemically induced with this method confirmed with XPS (Table S1) did not vary the surface residence times after an initial decrease (Figure 3.4B), likely a direct result of consistent grafting site densities.

Hindered lysozyme surface mobility is shown with narrowed step size distributions (Figure 3.4C) and decreasing trajectory's radius of gyration values by 19% after 5 minutes of ligand grafting (Figure S15). However, no shift in the step size distributions indicates that the introduction of low oxidative species has a less severe effect on lysozyme step size. However, trajectory's radius of gyration values indicate that increasing ligand chain lengths causes lysozyme molecules to explore less area of the interface (Figure S15). One possible explanation for this tunability in the trajectory's radius of gyration is steric confinement effects in hydrated ligand chains. This is further supported given the relative binding rates from 10 minutes to greater grafting times does not statistically change (Figure

3.4A), however the area lysozyme molecules explore decreases (Figure S15). Thus the number of adsorption sites is not changing as grafting time increases, rather hydrophilic ligand chains likely sterically confine adsorbed lysozyme molecules.

3.4.4. Functionalization technique comparison

Lysozyme adsorption dynamics and polystyrene surface chemistries are dependent on the method used to functionalize the interface. Single molecule results indicate that the lowest binding rate is achieved with the ligand grafting method, due to the large amount of oxygen containing groups introduced to the surface (Table S1) and the resulting water hydrogen bonding networks that have been shown to form at these interfaces.^{209,196} Surface residence times of lysozyme molecules decrease as a result of plasma and ligand grafting treatments. However, a comparison of plasma treatment and ligand grafted results indicate that both surface hydrophilicity and induced functional group densities dictate surface residence times.

Surface confinement of lysozyme molecules is also dependent on the functionalization technique. Surface oxidation produces smaller trajectory step sizes and a decrease in trajectory's radius of gyration values for all treatments used in this study. A correlation coefficient of 0.70 was calculated from all measured contact angles from each treatment method and the corresponding radius of gyration values indicating that overall surface hydrophilicity is strongly correlated to lysozyme surface mobility (Figure S16). Plasma treatment causes the most severe case of hindered mobility with a large shift in single frame displacement distributions and lowest trajectory's radius of gyration values.

This difference in lysozyme confinement is caused by the highly oxidized states of oxygen chemistries introduced with this treatment method and the increasing the role of water hydration layers at this interface this was supported with XPS analyses (Figure S9). We hypothesize that greater degrees of water hydrogen bonding networks at the oxidized polystyrene interfaces is causing varied lysozyme mobility at these interfaces. In particular the greater degree of lysozyme immobility seen with the higher oxidized plasma treated polystyrene in comparison to the ligand grafted surfaces. This hypothesis is supported by Tu and coworkers recent work²⁰⁹ which experimentally showed that carboxylic terminated interfaces have greater water loading capacities and more dense water hydration layers than alcohol terminated surfaces. The plasma treated surface did however exhibit larger contact angles than the ligand grafted surface due to the relative densities of functional groups induced to the surface as shown by XPS with lower oxygen content on the plasma treated surface (Table S1). In addition Lyulin *et al.*¹⁹⁶ showed that greater degrees of induced oxygen to polystyrene surfaces increases the number of water hydrogen bonds and density of water molecules at the interface of polystyrene surfaces. Here we propose these effects seen by Tu and others²¹⁰ is playing a direct role in the greater degree of lysozyme immobility for plasma treated interfaces in comparison to the more hydrophilic ligand grafted surfaces. Therefore, the greater degree of water hydrogen bonding capabilities dictated by the amount of oxygen and the oxidation state of the moieties on the polystyrene are playing a direct role in the varied lysozyme transport dynamics in addition to the overall surface hydrophilicity. This highlights the role of oxidative states chemistries and its direct effect on interfacial transport for lysozyme. The effects of hindered single molecule

transport on surfaces exhibiting different hydrophilicities and surface chemistries has also been witnessed by others.^{106,86} To access the role of steric effects in hindered lysozyme transport surface morphology of the polystyrene interfaces must be investigated.

3.4.5. AFM Surface Roughness Analysis

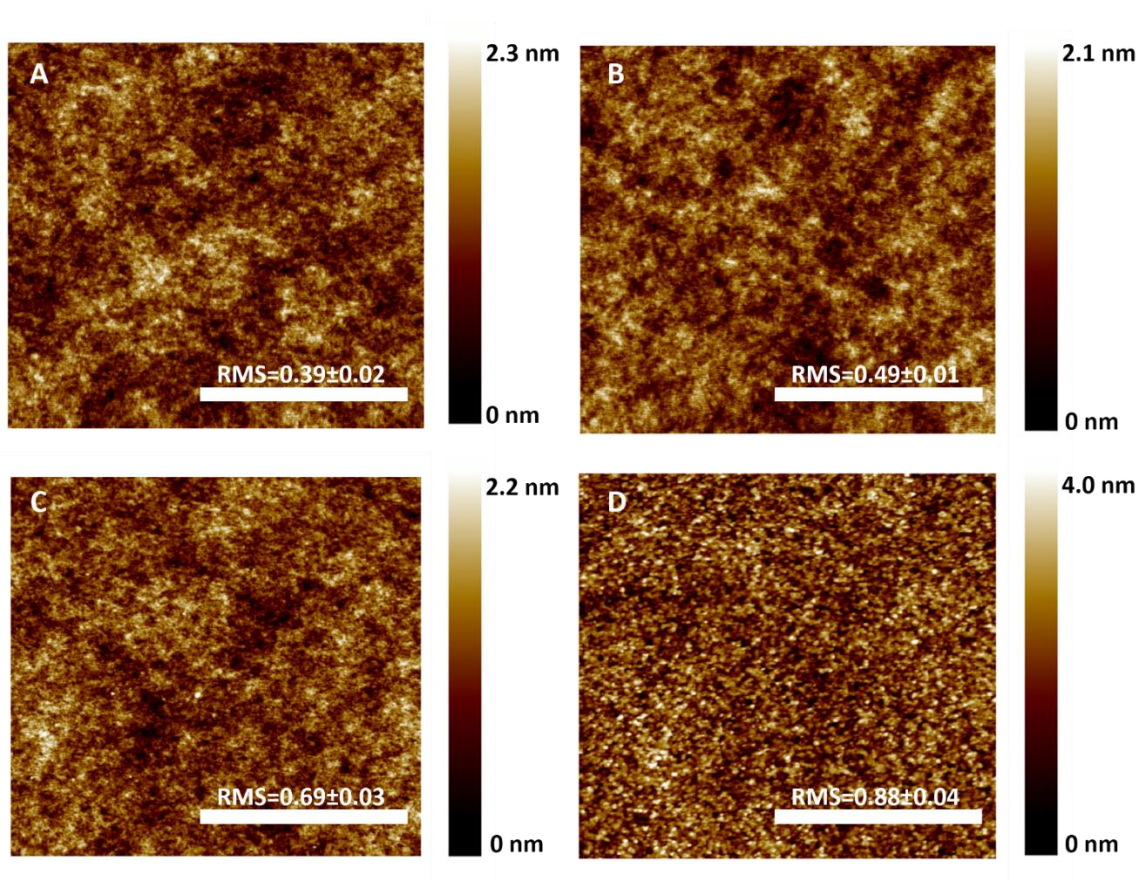


Figure 3.5 Atomic force microscopy analyses of surface roughness on as prepared and oxidized polystyrene samples, all images shown are $1 \times 1 \mu\text{m}^2$ area (Scale bar = 500 nm). Samples (A-D) are representative of: (A) native polystyrene (B) UV treated polystyrene (30 min.) (C) plasma treated polystyrene (7 sec.) and (D) ligand grafted polystyrene (30 mins). Root Mean Squared (RMS) surface roughness values (nm) were determined by taking surface roughness measurements using Nanoscope analysis software (Version

1.5) and measuring $2 \times 2 \mu\text{m}^2$ iteratively on 5 separate regions of two samples for each treatment. Error is the standard deviation of sampled data for each method.

Atomic Force Microscopy is utilized to uncover functionalization induced surface changes and access its role in variable lysozyme surface interactions. Polystyrene surface roughness increases as a result of all treatment techniques used in this work (Figure 3.5). Although nucleation and growth effects are often dominant in surface modification our AFM analyses do not spatially resolve these types of surface morphologies.

Corresponding surface roughness values for each treatment time is shown in Figure S17 with the most severe rate of roughness increase produced from the ligand grafting treatment followed by plasma treatment and UV treatment. The ligand grafting produced a 32% increase in surface roughness after 5 minutes in comparison to a 6.3% increase from 1 second of plasma treatment and only a 3.2% increase after 10 minutes of UV treatment. The surface roughness increase compared to increasing surface hydrophilicity produces a correlation coefficient of -0.76 for all treatment methods (Figure S16). Thus the increase in polystyrene surface hydrophilicity is correlated to increasing surface roughness but also originates from water hydration layer formation at various oxygen species as previously discussed.

Results introduce the possibilities of steric hindrance playing a role in decreased lysozyme binding rates and confined lysozyme surface transport surface dynamics. However, this is unlikely given the ligand grafting method produces the largest roughness increase but only results in a narrowing of single frame displacement distributions and a

gradual decrease in trajectory's radius of gyration values in comparison to the other methods. These results do however support steric entanglement effects leading to trajectory's radius of gyration tunability on the ligand grafted surface that allowed us to directly control the functional groups induced to the surface. Additionally, the surface features seen in AFM analyses are much larger in size in comparison to the small globular structure of lysozyme ($R_H \sim 19 \text{ \AA}^{211}$).

AFM analysis in combination with single molecule tracking highlights the large variation in interfacial chemistry and surface morphology of oxygen containing polystyrene interfaces. Resulting variations in lysozyme surface transport are dependent on the surface hydrophilicity and the specific oxygen containing species introduced to the polystyrene surface.

3.5. Conclusion

Single molecule spectroscopy uncovers hindered lysozyme transport at oxidized polystyrene interfaces. This is supported by a decrease in single frame step size and trajectory's radius of gyration values for all treatment methods utilized in this study. The functionalization methods in this study introduce unique oxygen containing moieties producing varying degrees of surface hydrophilicity and roughness. Although similar trends are uncovered in the adsorption dynamics of each treatment method, each technique results in unique dynamics, specifically the tunability in surface residence times for plasma treatment and trajectory's radius of gyration tunability for ligand grafting. This emphasizes the significance of the densities and oxidative states of

functional groups introduced to polymer interfaces and how that dictates the adsorption and desorption dynamics of biological macromolecules along polymer interfaces. These findings are likely due to the role of hydrophobics in interfacial water hydration layers and how that effect is exacerbated with increasing density of hydrophilic modalities. Furthermore, the oxidation state of species introduced to the interface also determine the strength and viscosities of water hydration layer formation. Although water adsorption and organization at these interfaces plays a crucial role in the observed lysozyme surface dynamics, water does not dictate the efficacy of modified polymer coatings in biological environments. Rather, non-specific protein adsorption that induce protein accumulation and unfolding on the polymer interface reduce the efficacy of the modified polymer over time. Therefore understanding the complex interactions of functionalized polymer and proteins is essential to function specific polymer design.

Although we concluded that hydrophobic effects are the dominant force accounting for changes in surface transport dynamics, it does not exclude the minor roles of electrostatics, Van Der Waals forces and hydrogen bonding are always present in protein adsorption dynamics. Single molecule techniques can be further implemented to uncover the adsorption and transport dynamics of other complex macromolecules, baring significance in many other applications.²¹²⁻²¹⁴

A mechanistic examination of salting out in protein-polymer membrane interactions

ΔThis work was published and is reproduced here with permission in the Proceedings of the National Academies of Science of the USA: Moringo, Nicholas A., Logan DC Bishop, Hao Shen, Anastasiia Misiura, Nicole C. Carrejo, Rashad Baiyasi, Wenxiao Wang, Fan Ye, Jacob T. Robinson, and Christy F. Landes. "A mechanistic examination of salting out in protein–polymer membrane interactions." *Proceedings of the National Academy of Sciences* (2019): 201909860.

4.1. Abstract

Developing a mechanistic understanding of protein dynamics and conformational changes at polymer interfaces is critical for a range of processes including industrial protein separations. Salting out is one example of a procedure that is ubiquitous in protein separations yet is optimized empirically because there is no mechanistic description of the

underlying interactions that would allow predictive modeling. Here, we investigate peak narrowing in a model transferrin-nylon system under salting out conditions using a combination of single-molecule tracking and ensemble separations. Distinct surface transport modes and protein conformational changes at the negatively charged nylon interface are quantified as a function of salt concentration. Single-molecule kinetics relate macroscale improvements in chromatographic peak broadening with microscale distributions of surface interaction mechanisms such as continuous time random walks and simple adsorption-desorption. Monte Carlo simulations underpinned by the stochastic theory of chromatography are performed using kinetic data extracted from single-molecule observations. Simulations agree with experiment, revealing a decrease in peak broadening as the salt concentration increases. The results suggest that chemical modifications to membranes that intrinsically decrease the probability of surface random walks could reduce peak broadening in full scale protein separations. More broadly, this work represents a proof-of-concept for combining single-molecule experiments and a mechanistic theory to improve costly and time-consuming empirical methods of optimization.

4.2. Significance

Membrane based protein separations are utilized broadly, and increasingly, to purify proteins for research and biopharmaceuticals. Like all steps in the purification process, the salt concentration is adjusted empirically in the mobile phase to elute a desired component of a protein mixture. There is insufficient quantitative description about the salting out process to allow for predictive optimization. By quantifying the

interactions and kinetics of single proteins at the surface of a membrane as salt concentration is increased, we relate mechanistic nanoscale observables to an improvement in the peak broadness observed in real separations. This result suggests that simulations, informed by small scale single-molecule observations, could be used to optimize separation conditions leading to more efficient separations.

4.3. Introduction

Protein separation and purification are the dominant expenses in biological drug development, largely because they are optimized empirically.^{4-5,7} Mechanistic insight into protein separations would allow the predictive optimization of macroscale separations^{13,215-216} and broadly impact everyday healthcare products²¹⁷⁻²¹⁸ and biosensing devices.^{145,219-222} A common process in protein separations is ‘salting out’, in which high salt concentrations are introduced to the mobile phase to improve elution efficiency.²²³⁻²²⁴ Salting out is thought to aid in separations by altering protein-stationary phase interactions through ionic shielding^{65,225} and/or precipitating proteins from the mobile phase as predicted by the Hofmeister series leading to faster elution.²²⁶⁻²²⁸ Acquiring micro- and nanoscale details about protein/stationary phase interactions during salting out is crucial because the ionic conditions can be related to macroscale peak broadening in protein separations.^{66,229-231} Understanding the dynamic temporal changes occurring at separation interfaces is of critical societal importance as recently reported by the National Academies of Sciences.¹

Structure-function relationships between target proteins and the stationary phase under salting out conditions are not well understood and are experimentally challenging to

quantify *in situ*.²²³⁻²²⁴ Common methods for monitoring protein-surface interactions include surface plasmon resonance,²³² isothermal titration calorimetry,²³³ and atomic force microscopy.²³⁴ Although these experimental techniques provide new insight into complex protein-polymer interactions, they suffer from ensemble averaging and lack high spatiotemporal resolution necessary to develop a physiochemical mechanism of protein-stationary phase interactions. Moreover, proposed models extracted from these techniques likely oversimplify the underlying mechanism of interfacial adsorption-desorption, surface diffusion, and surface induced protein unfolding effects.²³²⁻²³³ Single-molecule microscopy is well suited to directly visualize protein mass transport at a wide array of complex interfaces one molecule at a time with a high spatiotemporal resolution.^{20,24,235-238} However, atomistic details of protein surface domains and/or substrate chemistries interacting during protein physisorption is not resolved in comparison to atomistic modeling techniques.²³⁹ Heterogeneous protein surface kinetics and transport can be quantified in experimentally challenging systems^{53,172} as a result of advancements in single-molecule tracking algorithms,²⁷⁻²⁸ point spread function engineering techniques,^{23,25,240-241} and the increased sensitivity of scientific cameras.²⁰

Herein, Total Internal Reflectance Fluorescence (TIRF) widefield single-molecule tracking is used in combination with ensemble fast protein liquid chromatography (FPLC) to relate tracking observables to ensemble elution profiles. Additionally, circular dichroism (CD) spectroscopy is utilized to quantify structural changes of proteins at the stationary phase support and relate to TIRF and FPLC results. TIRF single-molecule tracking has been recently shown to reveal interfacial protein dynamics on a range of surfaces, including

natural and synthetic polymers^{52,70,81,85,242} and is ideal for measuring interfacial dynamics as it intrinsically suppresses background signal from emitters diffusing in the bulk solution. TIRF microscopy has been applied in many other systems including nanoparticle catalysis,²⁴³⁻²⁴⁵ DNA hybridization kinetics,²⁴⁶⁻²⁴⁸ and protein transport in live cells.²⁴⁸⁻²⁴⁹ These examples also highlight the robust nature of single-molecule tracking for investigating multiplexed and highly heterogeneous systems.^{87,181}

The dynamics of single transferrin proteins, a well-studied target cancer therapeutic protein,²⁵⁰⁻²⁵¹ at the interface of nylon 6,6 is used to examine the mechanistic origin of changes in chromatographic peak width during salting out in FPLC. CD results lend insight into the structural changes induced to transferrin at the nylon interface during salting out and are related to single-molecule tracking and FPLC observables. Increasing salt concentration is used to emulate salting out conditions used in membrane chromatography. Nylon is chosen as a stationary phase material as it is commonly used in protein membrane separations and is a known hydrophilic antifouling surface.²⁵²⁻²⁵³ Membrane based separations have garnered recent interest given the reduced mass transfer resistance, increased surface area for adsorption, and lower column costs in comparison to traditional bead packed columns.²⁵⁴ Additionally, nylon is a chemically robust and optically transparent polymer stable under laser illumination,^{23,255} and utilized in many consumer products.²⁵⁶ Surface transport modes and kinetics of transferrin are quantified at the single-molecule level and used to explain the reduction of peak broadening observed in ensemble separations. Single-molecule kinetics further inform Monte Carlo simulations that agree with FPLC results, predicting peak narrowing at higher salt concentrations. For the first

time, single-molecule observables link ensemble separations based on a mechanism that is supported by simulation.

4.4. Materials and Methods

4.4.1. Single-molecule tracking

A home built wide field epifluorescence microscope (Zeiss body, Tube lens $f=165$ mm) is used for all single-molecule experiments. TIRF excitation of fluorescently labeled transferrin is achieved with a continuous wave 532 nm diode laser (Coherent, Compass 315M-100SL) focused at the edge of a high numerical aperture oil immersion objective (Carl Zeiss, NA=1.45, 100X, Alpha Plan-Fluar) resulting in a critical angle of roughly 78° . TIRF excitation produces an exponentially decaying evanescent field that propagates from the nylon-buffer interface roughly 85 nm into the bulk solution,³² thus only exciting transferrin molecules located near the nylon surface. The refractive index of nylon (1.58) closely matches glass (1.51), in contrast to the refractive index of aqueous HEPES buffer used in the protein dilutions (1.33).⁵³ Refractive index mismatch at the buffer-nylon interface meets the TIRF condition. Experimental confirmation of the TIRF condition at the buffer-nylon interface is previously shown in our past work.⁵³ Evanescent field excitation improves the signal-to-noise ratio by suppressing excitation of transferrin molecules in the bulk solution. Excitation power density at the nylon interface is 0.10 kW/cm^2 for all single-molecule acquisitions. Collected

fluorescent light is magnified by 2.5X and is filtered using a dichroic filter (Chroma, z532/ rpc633), notch filter (Kaiser HPNF-532), and band pass filter (Chroma, ET585), ensuring all laser light is removed from the final image. Images are collected on an electron-multiplying charge coupled device (Andor, iXon 897) operated at -70°C. All movies are collected with an integration time of 50 ms and a gain of 300. A previously published tracking algorithm is used to track single-molecules on the nylon interface and is explained in further detail in the *SI Appendix*.²⁸ A minimum of 10,000 transferrin trajectories are analyzed for each presented condition.

4.4.2. Nylon Film Preparation and Microfluidic Assembly

Borosilicate microscope coverslips (Fisherbrand, No. 1) are sonicated for 30 min in 200 mL baths of cleaning agents: soapy water (Liquinox 2%), deionized water ($>1\text{M}\Omega\bullet\text{cm}$), methanol (Sigma, ACS grade), and acetone (Sigma, ACS grade) sequentially. Coverslips are then chemically etched in a base piranha solution heated at 80°C for 20 min and then rinsed under a stream of DI water prior to drying under a stream of nitrogen (Airgas, Ultra Pure).

Nylon 6,6 pellets (Sigma, zeta potential -21 ± 1 mV, *SI Appendix*) are dissolved in formic acid (Sigma, ACS grade) to produce a 1.5 w/w % solution. 100 μL of the nylon solution is drop cast on a coverslip and spin coated at 3000 RPM (SPI KW-4A) for 1 min. A dilute concentration of gold nanorods (Nanopartz, 50×100 nm) are spin coated on the nylon film to act as fiducial markers. Microfluidic

assemblies (Grace BioLabs, Hybriwell Chamber) are then attached to the nylon interface with tubes (Scientific Commodities, 0.03" internal diameter) attached at the inlet and outlet to supply a constant solution of 100 pM labeled transferrin at 50 $\mu\text{L}/\text{min}$ in 10 mM HEPES buffer (pH= 7.2).

4.4.3. Nylon Film Ellipsometry

Nylon film thickness is quantified (129.0 ± 0.3 nm) using ellipsometry (Gaertner 7109-C370B, SI *Appendix*, Fig. S1). Nylon films are spin coated on clean silicon wafers (Ted Pella, 100) for ellipsometry measurements.

4.4.4. Fluorescent Protein Solution Preparation

Rhodamine B labeled transferrin (Nanocs) is dissolved in 10 mM HEPES buffer and is diluted to 100 pM for all single-molecule experiments presented in this work. Mass spectrometry confirms the purity and absence of contaminant proteins and/or free-dye molecules in the purchased protein powder (SI *Appendix*, Fig. S2).

4.4.5. Nylon Bead Preparation

A 1.5% w/w formic acid solution of nylon 6,6 is sonicated for roughly 24 hours and then slowly added to water under continuous stirring. The resulting precipitate is filtered using an 8 μm filter (Whatman) to remove large nylon aggregates.

4.4.6. Ensemble Fast Protein Liquid Chromatography

Ensemble separations are conducted on a home-built FPLC system. Flow is controlled using a peristaltic pump (Watson-Marlow, 120 Series) and absorbance is monitored at 280 nm using a UV detector (Spectrum Chromatography) and recorded on a digital recorder (Hantek, 365E) controlled by Hantek 365 software. The 280 nm absorbance wavelength is commonly used for chromatographic protein measurements.²⁵⁷ Solutions of 70 μ M Transferrin (Sigma, >98%) with varied ionic concentrations are prepared in 10 mM HEPES buffer (Sigma, pH 7.2). Approximately 300 μ L of each solution tested is injected into the FPLC system. All separations are performed at an average flow rate of 1.7 mL/ min. The salt concentration of the feed HEPES buffer is identical to each tested condition, ensuring the salt concentration of the injection solution matched the salt concentration of the feed solution. For all separations, a series of four nylon 6,6 membrane filters (Biomed Scientific, 25 mm diameter, 21 mm thick, 3.9 cm² filtration area, non-sterile) are connected in series to the FPLC setup. Surface identity of nylon 6,6 membranes and nylon 6,6 used in single-molecule experiments is confirmed to be chemically identical with X-ray photoelectron spectroscopy (SI *Appendix*, Fig. S3). A series of membrane filters is chosen given recent commonplace in downstream separations.^{254,258}

4.4.7. Monte Carlo Chromatographic Simulations

The underlying principles of our Monte Carlo method stems from the original Giddings and Eyring formula¹⁸ that establishes the total retention time (T) of a single molecule to be the combination of the time spent in the mobile phase (t_m) and the time spent at the stationary phase (t_s).²⁵⁹⁻²⁶¹ Here we assume t_m remains a constant value to reduce the complexity of the system. However, we expand t_s as the sum two exponentially distributed surface residence times with a specific prevalence and desorption rate constant at each salt concentration informed by single molecule kinetics.²⁶² Expanding t_s produces Equation 4.1:²⁶³⁻²⁶⁵

$$t_s = \sum_i^m \sum_j^n \tau_{i,j}$$

Equation 4.1 Time spent at stationary phase support as per Giddings and Eyrings statistical model.⁶⁶

where T is the total elution time, t_m is the amount of time spent in the mobile phase and $\tau_{i,j}$ is the desorption time of the i^{th} desorption event via the j^{th} desorption pathway. Each exponential describes one of m different desorption pathways differing in some physical or chemical aspect that alters transferrin's interaction with the stationary phase. Stationary phase effects are tuned by altering the number of desorption pathways (m), the relative prevalence of these pathways in the column, and the difference in k_d between each pathway. Simulating the motion of

500,000 molecules down the column and quantifying their retention times via histogram generates an ensemble chromatogram from each of the single molecule histories.

Monte Carlo simulations examine the time taken for a series (500,000 for each condition) of molecules to migrate the length of the column, alternating between periods of motion (mobile phase) and periods of stagnancy (stationary phase). Adopting a description from Giddings' book,²⁶⁶ the process of motion down the column is an alternation of the molecule between the adsorption state and mobile state with some rate of exchange defined by k_{des} . Extending the number of adsorption states simulates the existence of multiple adsorption pathways in the column. Tuning exchange between mobile and adsorption states, probability of entering an adsorption state, and number of cycles through the model probes contributions of heterogeneous adsorption sites due to kinetic irregularities,^{70,267} surface site availability/porosity,²⁶⁸ and overall column length.²⁶⁹ Predictive design would be achieved through collecting kinetic parameters via experiment,²⁷⁰ modeling kinetic effects with the described framework, then applying these insights to generate an optimized stationary phase.

Simulated chromatograms using kinetics extracted from single-molecule tracking experiments are performed using custom Python scripts based on the mathematical construction of Giddings and Eyring.¹⁸ Simulation sets are initialized to contain two desorption pathways ($m = 2$), adopting the calculated desorption rate and prevalence of each desorption pathway from single-molecule kinetics.

Elution is simulated by assuming 500,000 molecules all migrate down a column with 100 possible adsorption events, averaging 50 adsorption events per molecule. Desorption times from each event are summed together with a constant mobile phase time (t_m) to calculate the retention time of each molecule. Simulated chromatograms are then created by binning the molecule retention times to the time resolution of the simulated clock. All scripts used to run the simulations are available for download at <https://github.com/LandesLab?tab=repositories>.

4.4.8. Processing and fundamental workings of Simulated Chromatograms

The fundamental unit of time, tracked in the form of elementary steps (δt , measured in ms), establishes a clock across all molecules adaptable to any standard unit of time.²⁶³ A simulated trajectory of length 1000 steps has $t_m = 1000 \delta t$ constant travel time, thereby guaranteeing that all asymmetry effects are driven by the difference in kinetics. The probability that a molecule interacts with the stationary phase in each step is a fixed value independent of the column position ($P(\text{ads}) = 0.5$).^{18,271} As such, the distribution of adsorption events in the column is a Gaussian distribution centered at $n = 500$.

The simulation examines the situation where two desorption scenarios are present in the column ($m = 2$) as kinetic heterogeneity has been shown to cause tailing in previous work, both experimentally and theoretically.^{63,65-66,272} Our simulations feature one short (k_1) dominant scenario occurring more frequently and one longer (k_2) pathway occurring less frequently. Presented chromatograms were

generated by binning retention times of each molecule with bin widths equivalent to $\delta t = 500$ ms (resolution of FPLC detector). Post-processing of each chromatogram involved filtering with a Savitzky-Golay filter²⁷³ and fitting with a cubic spline using open-source code provided by SciPy. Height intercepts used to calculate are calculated using the fit to determine the FWH of each chromatogram.

Statistical information is drawn from the raw molecule counts before any data processing. Simulated chromatographic curves are smoothed using a Savitzky-Golay filter²⁷⁴ as provided by the Python SciPy package. The smoothed data is then fit using a cubic spline to transition the curve shape to a polynomial form. FWHM error is calculated by performing simulations of only 100,000 molecules five times and reporting their deviation shown in Figure 4.5.

4.5. Results and Discussion

4.5.1. Transferrin surface dynamics

Single-molecule tracking resolves two distinct modes of transferrin surface dynamics at nylon, which are tuned by salt concentration. One population exhibits a continuous time random walk (CTRW) on nylon while the second population undergoes single site adsorption-desorption (Figure 3.1A-C). Proteins exhibiting a CTRW display periods of immobile physisorption disrupted by surface exploration to nearby adsorption sites.⁸² CTRWs, present in transferrin-nylon interactions, can be identified by waiting time distributions that fit a power-law (SI Appendix, Fig. S4).⁷⁹⁻⁸⁰ The prevalence of transferrin

molecules undergoing CTRWs decreased as salt concentration increased, resulting in more single site adsorption-desorption. However, CTRWs remained the dominant mode of transferrin surface transport (Figure 4.1A-C). Representative single-molecule trajectories at varied ionic conditions in Fig. 1B illustrate the two modes of dynamics that transferrin displays at nylon. The dynamics are spatially resolved below the diffraction limit of light.^{28,275} Spatial trajectory filtering is applied to quantify and classify dynamics as either CTRW (Figure 4.1B, cyan) or single site adsorption-desorption (Figure 4.1B, magenta). In short, if a transferrin molecule moved >22 nm from the initial localization position during a trajectory, a length scale greater than our localization precision, the trajectory is classified as CTRW (details in *SI Appendix*).^{32,53} The relative percentage of the two populations as a function of salt is shown in Figure 4.1C. Tracking results show that increased salt concentrations resulted in a relative decrease of $18\pm3\%$ in CTRW of transferrin at nylon. Although the transition to pure adsorption-desorption is not complete, the observed salt-dependent changes in surface dynamics hold important implications for the ensemble elutions and simulations presented later. Though transferrin surface diffusion is non-Brownian, diffusion coefficient values are calculated and compared with bulk diffusion measurements (*SI Appendix*, Table S1). Additional mechanistic details are also revealed by analyzing frame to frame displacements, discussed next.

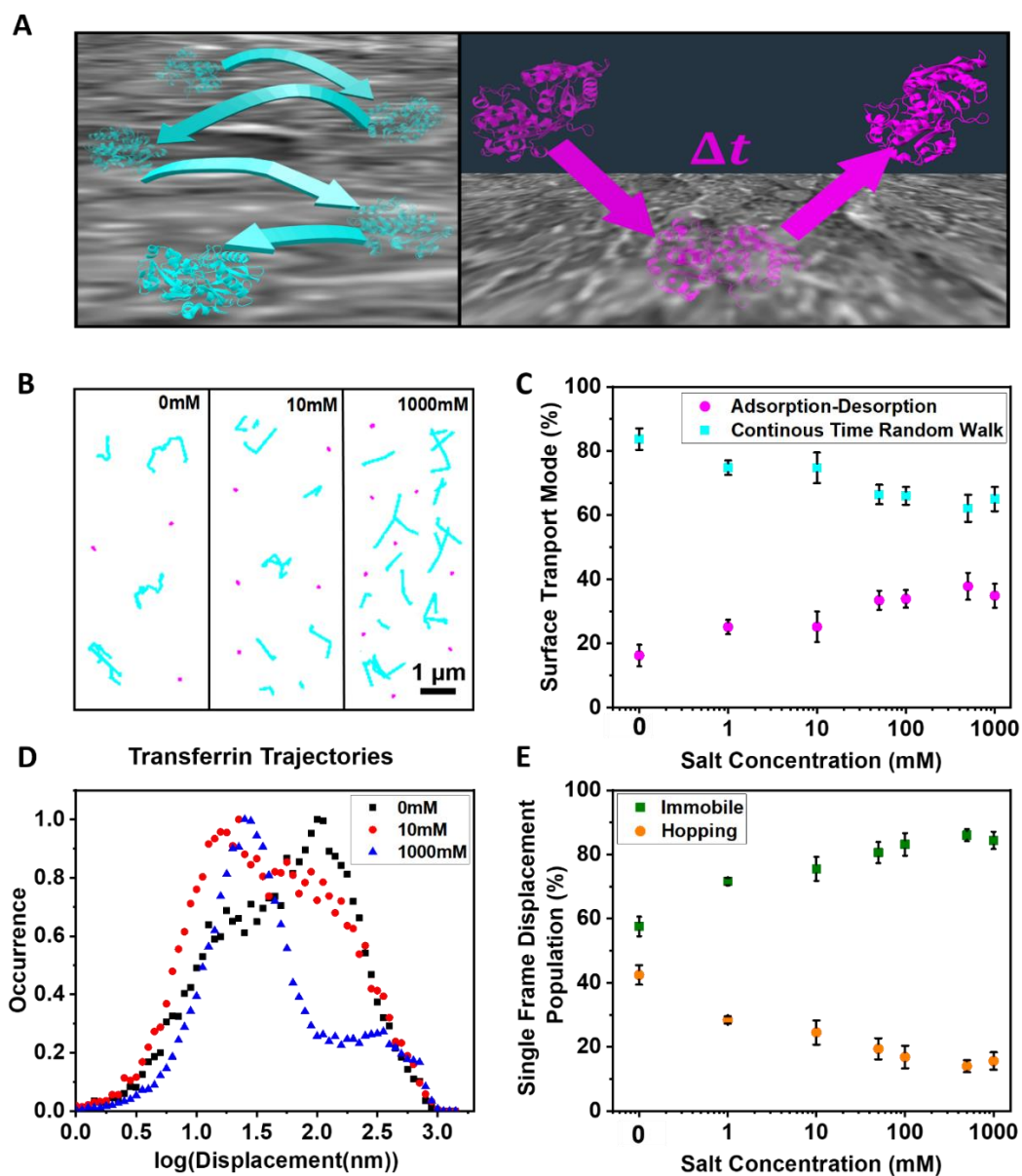


Figure 4.1 Transferrin surface dynamics at nylon at varied ionic strengths. (A) Cartoon representation of two modes of transferrin-nylon interaction, CTRW (cyan) and single site adsorption-desorption (magenta) (PBD: 1D3K²⁷⁶). **(B)** Representative single-molecule transferrin trajectories at nylon interface undergoing a CTRW (cyan) and single site adsorption-desorption (magenta). **(C)** Percentage of transferrin molecules exhibiting CTRW vs. simple adsorption-desorption. **(D)** Single frame displacement distributions at varied

ionic strengths. (E) Percent of single frame displacements contributing to immobile and hopping surface transport from sampling distributions in C. The 0 mM condition is shown on logarithmic scale in (C, E) in order to display entire range of salt concentrations.

Single frame displacement distributions quantify the shift towards immobile adsorption events at high salt concentrations (Figure 4.1D). Two spatially resolvable populations of displacements have been reported before in dye-multilayer polyelectrolyte interactions²⁷⁷ but never in the case of protein-polymer interactions to our knowledge. Single frame displacement distributions are histograms quantifying the distance a molecule travels frame to frame. It must be noted that a single protein trajectory can contribute to both populations observed in Figure 4.1D if a molecule experiences periods of confinement and hopping. A previously published Markov Chain Monte Carlo (MCMC) algorithm quantifies both the relative percentage and the mean hop distance of the two distinct populations in the single frame displacement distributions (Fig. 1D, *SI Appendix*, Fig. S5).²⁷⁷ The MCMC algorithm removes any statistical bias attributed to selected distribution bin sizes by generating distributions that model the experimental data.²⁷⁷ Analysis of the single frame displacements indicate that a $27\pm3\%$ decrease in frame to frame hopping is observed as salt concentrations are increased from 0 mM to 1000 mM in a tunable fashion (Figure 4.1D-E). Displacement distribution results are independent of the order in which salt is introduced, indicating transferrin transport is reversible under the steady state flow conditions used here (*SI Appendix*, Fig. S6). Single frame displacement analyses indicate that after the initial adsorption of a transferrin molecule the likelihood of transferrin exploring nearby sites is decreased at high salt concentrations. The combination

of trajectory spatial filtering and single frame displacement distribution analyses reveal that single site adsorption-desorption behavior of transferrin increases, accompanied by a lower probability of surface exploration. Single-molecule tracking lends mechanistic insight into the multifaceted surface transport of transferrin at nylon and also quantifies kinetic changes in transferrin-nylon interactions.

4.5.2. Single-molecule Transferrin Kinetics

Transferrin adsorption rates increase on the nylon interface at higher salt concentrations, reaching roughly a tenfold increase at a salt concentration of 500 mM (Figure 4.2A). The rate of adsorption is quantified by counting the number of new identified molecules that arrive at the interface per unit area and time. Increases in adsorption rates at increased ionic strengths correlate to more transferrin molecules imaged at the surface (Figure 4.2A). Quantifying the *absolute* adsorption rates is often experimentally unachievable, but can easily be quantified with single-molecule tracking.²⁷⁸⁻²⁷⁹ One explanation for the increased binding at higher salt concentration is a decreased solubility of transferrin molecules in the mobile phase as predicted by Hofmeister^{227,280}, but this theory is widely debated to date.²⁸¹⁻²⁸² Similar increased adsorption kinetics observed with Hofmeister salts at the single-molecule level predicted that increased hydrophobic interactions lead to higher rates of adsorption.²⁷⁸ Another possible driving force in transferrin-nylon interactions is the electrostatic screening of repulsive interactions between transferrin (pI 5.6)²⁸³ and nylon (zeta potential -21 ± 1 mV), both of which carry a negative charge at pH 7.2.²⁸⁴⁻²⁸⁶ Electrostatic forces dominating the

adsorption rate changes of proteins at interfaces has been explored by Schwartz and coworkers in addition to short-range interactions dictating desorption kinetics.²⁷⁹ Increased adsorption rates indicate that the transferrin molecules exhibit a greater attraction for the nylon interface as salt is increased in the mobile phase. In addition to adsorption kinetics, single-molecule results also elucidate desorption kinetics of transferrin, as discussed next.

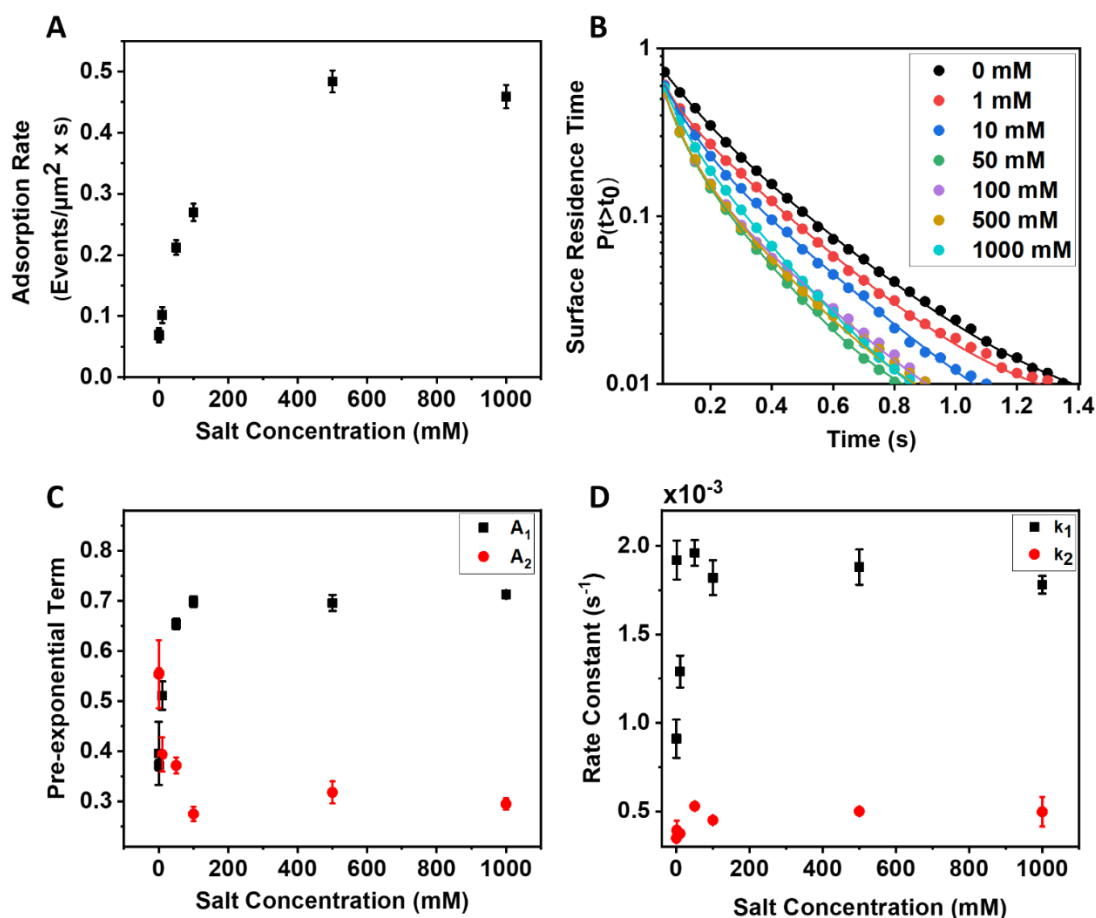


Figure 4.2 Transferrin kinetics at nylon at varied ionic strengths. (A) Rate of adsorption. (B) Surface residence time distributions represented in a cumulative distribution and fit to a double exponential decay with solid lines

(Equation 4.2). (C) Pre-exponential coefficients from fitting results in (B). (D) Desorption rate constants from fits in plot (B).

Surface residence time analyses uncover two distinct populations of transferrin desorption from the nylon interface, revealing an overall increase in desorption rates accompanied by a decrease in rare long-lived events. Surface residence time distributions (Figure 4.2B) are represented as cumulative distribution functions (CDF) to uncover rare long lived binding events,³¹ which have a large influence on protein separation efficiencies as discussed in later sections.^{66,287-288} Surface residence time distributions are fit to a two-term exponential decay Equation 4.2:

$$P(t) = A_1 e^{-k_1 t} + A_2 e^{-k_2 t}$$

Equation 4.2 Two term exponential for desorption rate constants

to identify the desorption kinetics of transferrin molecules. Exponential decays are used to quantify single-molecule interfacial desorption kinetics from surface residence time distributions.²⁴⁶ CDF plots are shown for all salt conditions tested with corresponding fits to Equation 4.2 in Figure 4.2B. Visual inspection of the tails of CDF distributions highlights that increasing salt concentration decreases the number of rare long-lived adsorption events at nylon (Figure 4.2B). CDF fitting is used to calculate the respective prevalence (Figure 4.2C) and desorption rate constants for the two individual populations of surface residing transferrin molecules (Figure 4.2D). The dominant desorption pathway of transferrin is changed at salt concentrations greater than 10 mM (Figure

4.2C). Desorption is dominated by fast dynamics at salt concentrations greater than 10 mM, in comparison to slow kinetics in the lower and no salt conditions (Figure 4.2C). Spatial filtering described above is applied to show the fast desorption population is dominated by molecules undergoing single site adsorption-desorption given they desorb quicker from nylon in comparison to transferrin molecules undergoing a CTRW. (SI *Appendix*, Table. S2). This is also supported by the decrease in the prevalence of CTRW motion at higher salt concentrations (Figure 4.1A-C) and the decrease in the prevalence of A_2 as the salt concentration is increased with a calculated correlation coefficient of 0.91 (Figure 4.2C). CDF fit results show the desorption rate constant (k_1) for the fast population increased as a function of salt, whereas the slow population desorption rate constant (k_2) is unchanged leading to an overall increase in desorption (Figure 4.2D). The conformational stability of transferrin is quantified with a denaturation experiment (SI *Appendix*, Fig. S7), showing that conformation is more robust with increased salt concentration. Stability increases could account for increased desorption rates observed from nylon at higher salt conditions discussed in the proceeding section. These results highlight the utility of single-molecule techniques to quantify kinetic metrics in highly dynamic and complex chromatographic systems.^{71,73,124}

4.5.3. Ensemble Circular Dichroism

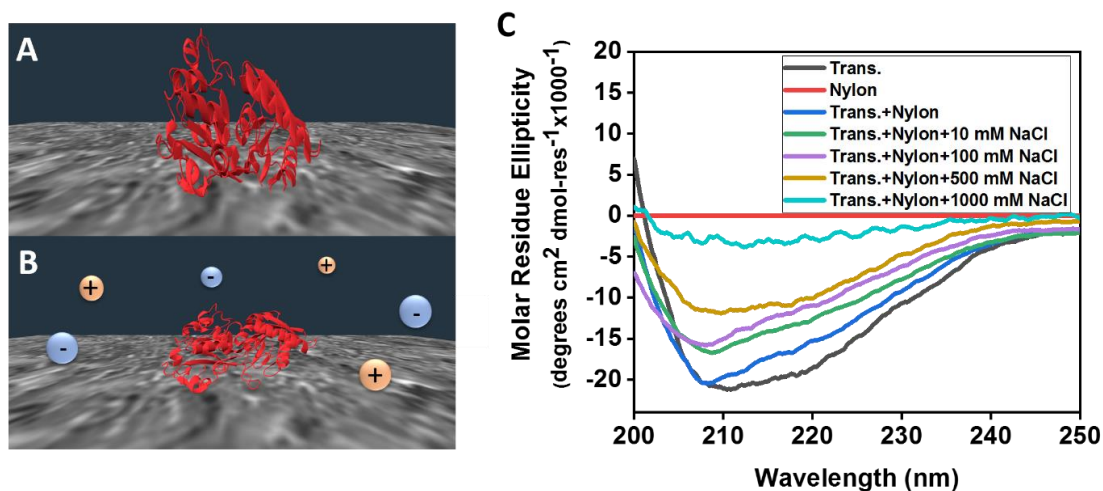


Figure 4.3 Structural examination of transferrin at nylon surface under varied ionic conditions. Cartoon depiction of folded transferrin (A) and unfolded transferrin (B) at nylon in the presence of salt (PBD: 1D3K²⁷⁶). (C) Ensemble CD spectroscopy of transferrin at varied ionic conditions in the presence of nylon microspheres.

Transferrin adsorption to the nylon interface induces the partial unfolding of transferrin, which is enhanced at higher ionic strengths (Figure 4.3A-C). CD spectroscopy is utilized to interrogate the secondary structural motifs that are present in a proteins structure.²⁸⁹ CD results show that a reduction in the alpha helical secondary structure is observed for adsorbed transferrin molecules on nylon microspheres, suggesting that transferrin adopts a partially unfolded conformation at nylon interfaces in the absence of salt (Figure 4.3C, blue). A further reduction in alpha helical structure is observed in a tunable fashion with increased salt concentrations (Figure 4.3C). This transferrin

unfolding appears to be a surface induced phenomenon as unfolding is only observed in the presence of nylon microspheres and is not induced by salt alone (*SI Appendix*, Fig. S8). Surface induced unfolding of proteins and a resulting change in transport dynamics has been observed at the single-molecule level by others.^{80,290} Surface induced structural changes would not alter adsorption kinetics under our conditions (Figure 4.2A) since unfolding is a surface induced effect. However, structural changes of transferrin likely play a dominant role in the observed varied surface transport modes (Figure 4.1) and surface desorption kinetics (Figure 4.2B-D), given the large CD signal modulation as salt conditions are tuned. We predict and confirm that single site adsorption-desorption at nylon is dominated by unfolded transferrin molecules by quantifying surface dynamics of chemically unfolded transferrin molecules (*SI Appendix*, Fig. S9). We also confirm that the unfolded structure of transferrin contributes to the increased desorption rates observed at high salt concentrations with the observed desorption kinetics from chemically unfolded transferrin molecules. (*SI Appendix*, Fig. S10). Waiting time analyses, which quantify the time spent per site, confirm that although overall transferrin desorption rates increase with increased salt (Figure 4.2) the time spent per site increases (*SI Appendix*, Fig. S11) but at fewer sites (Figure 4.1D-E). Increased residence times once a protein unfolds on a surface has been well studied by others.⁸⁰ Salt-induced structural changes to nylon are ruled out as a major contributor to our observed transferrin dynamics because the timescale on which salt alters nylon hydration occurs over hours.²⁹¹ Therefore, transferrin unfolding has a direct effect on the surface transport dynamics of transferrin both spatially and kinetically under salting out conditions. CD results are also conducted with rhodamine B labeled

transferrin used in single-molecule experiments, confirming the addition of rhodamine labels does not alter transferrin interactions with nylon (SI *Appendix*, Fig S12).

4.5.4. Fast Protein Liquid Chromatography

We suggest that increased transferrin desorption kinetics and transferrin conformational changes upon adsorption presented above provide a mechanistic explanation for the utility of salting out in protein elutions (Figure 4.4). Ensemble FPLC of transferrin on nylon 6,6 membranes at increasing salt concentrations exhibits peak narrowing (Figure 4.4A). The decrease in broadening is compared in Figure 4.4B with the full width half maximum (FWHM) of the chromatograms, which is one way to compare peak widths in chromatographic studies.²⁹² The decrease in mean retention time observed (Figure 4.4A, inset) aligns with the increased desorption kinetics observed at the single-molecule level (Figure 4.2B-D). Constant salt concentrations are used here because a single type of protein is being purified,²⁹³ in contrast to salt gradients, which are required for separating mixtures of proteins. It is important to note that constant salt concentrations are also used for discovering the appropriate concentrations for separating individual analytes from a mixture when a salt gradient is employed.²⁹⁴ Overcrowding effects at nylon membranes is ruled out by separations performed with lower transferrin concentrations one order of magnitude above our detection limit (7 μ M). Similar line shapes and peak narrowing effects are observed at lower concentrations independent of the order of salt concentrations tested (SI *Appendix*, S13). Similar line shapes and fewer filters have been utilized by others performing protein FPLC, further ruling out overcrowding effects.²⁹⁵⁻²⁹⁶

The interaction of transferrin with nylon membranes is confirmed with CD measurements of an eluted fraction of transferrin at high salt (SI *Appendix*, S14). We observe unfolding, a surface induced effect, confirming transferrin adsorption at nylon in the FPLC system (SI *Appendix*, S14). A macroscopic theoretical model is necessary for linking single-molecule microscopic observables to FPLC results.

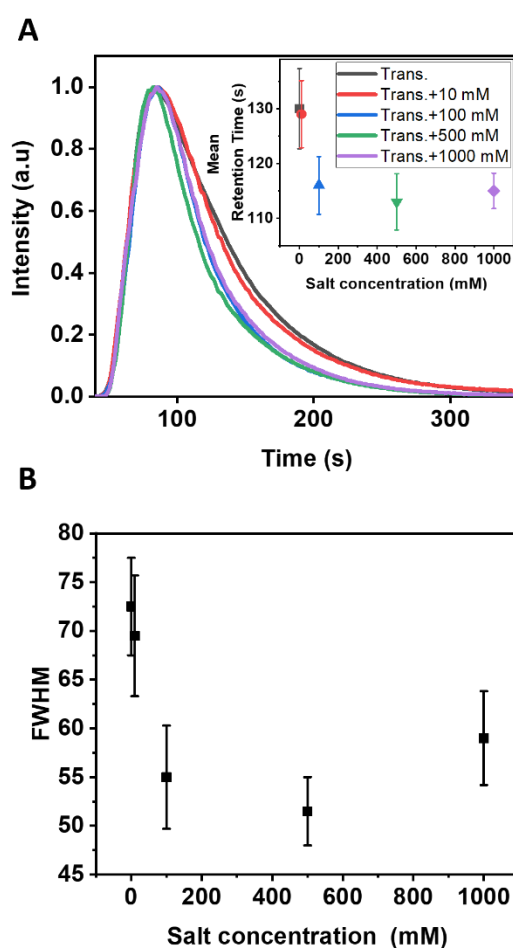


Figure 4.4 FPLC of transferrin with nylon membranes. (A) Transferrin chromatograms under salting out conditions with calculated mean retention times and standard deviation from triplicate separations (inset). (B) Full width half maximum of chromatograms shown in (A).

Importantly, the mechanistic link between the single protein kinetics presented in Fig. 2B and peak width is provided in Giddings' and Eyring's statistical theory of chromatography.⁶⁶ In the present work, increased desorption kinetic rates are observed at the single-molecule level in addition to the suppression of long-lived binding events dominated by the CTRW surface transport (Figure 4.2, SI *Appendix*, Table. S2). We predict that the suppression of CTRW lowered the probability of long-lived events leading to profile narrowing (Figure 4.4). This can be intuitively understood in the context of work by Schwartz and coworkers where a molecule exhibiting a CTRW will increase the probability of interacting with anomalously strong adsorption sites, thereby increasing the prevalence of long-lived events.¹⁸⁰ The observation of increased desorption kinetics reducing chromatographic tailing in liquid based separations has been reported by others.²⁸⁷ An overall decrease in the mean retention time of transferrin with increasing salt (Figure 4.4A, inset), accompanied with increased desorption rates observed at the single-molecule level (Figure 4.2), gives a microscopic explanation for macroscale separations with slating-out conditions, in which the analyte elutes more quickly with the addition of salt.²⁹⁷ Monte Carlo simulations based on single-molecule kinetics further support the conclusion of reduced broadening.

4.5.5. Monte Carlo Chromatographic Simulations

Monte Carlo simulations underpinned by the stochastic theory of Giddings and Eyring¹⁸ reveal that the kinetic data extracted from surface residence time fits (Figure 4.2B) predicts better resolved chromatographic peaks as salt increases. Simulated

chromatograms are generated using the pre-exponential coefficients (Figure 4.2C) and desorption rate constants (Figure 4.2D) found from the experimental fits of the surface residence time. Similar methods were employed by Dondi²⁹⁸ and Cavazzini²⁹⁹ to explore the effects of limited site availability as well as illustrate the equivalence of the stochastic theory and the macroscopic Lumped Kinetic Model. Increases in salt show a qualitative thinning of the profile and a visual decrease in the formation of a chromatographic tail (Figure 4.5B). Measurements of the FWHM of corresponding peaks support the conclusion that increasing the salt concentration of the mobile phase increases chromatographic efficiency via profile thinning (Figure 4.5C). Symmetric broadening/thinning is a direct result of the number of interactions that a protein has with the stationary phase surface. We deduce that profile thinning is driven by the reduction of CTRWs within the protein history, an effect that corroborates Giddings' theories.³⁰⁰ Simulations and experimental evidence corroborate previous studies showing that a decrease in long-lived adsorption events⁶⁵ observed here through increased salt content produce, narrower, more symmetric chromatographic peaks.^{63,66} The physical origin of the altered kinetics here are revealed in the single-molecule results which indicate that a decrease in CTRW dynamics (Figure 4.1A-C) at nylon decreases the prevalence of rare long-lived adsorption events (Figure 4.2B). The change in observed surface dynamics is facilitated by structural changes induced to transferrin at nylon (Figure 4.3, *SI Appendix*, Fig. S8). The combination of our simulations and single molecule results indicate that mobile phase effects are major contributors to peak symmetry. Other groups identified how heterogeneous mobile phase mixing among the components of the chromatographic

column introduces asymmetry/broadening.³⁰¹⁻³⁰² Examples of mobile phase effects include turbulent flow occurring at column junctions, including the injection port, column connection, and detector port, which can introduce profile broadening that varies between instruments.³⁰³

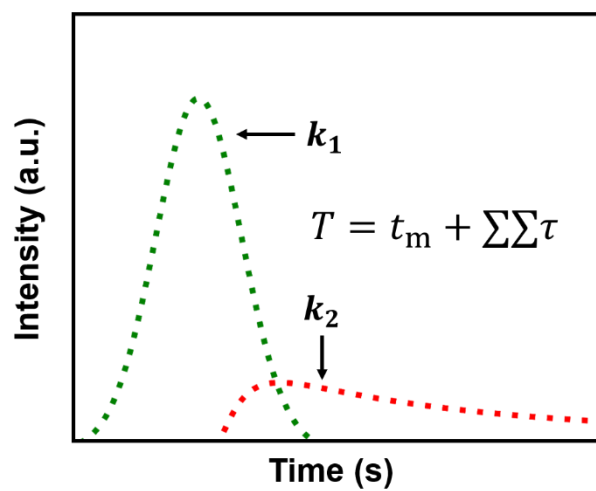
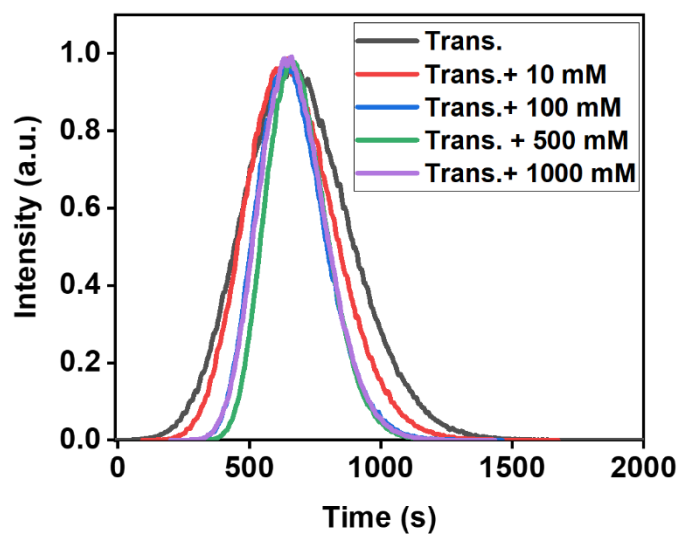
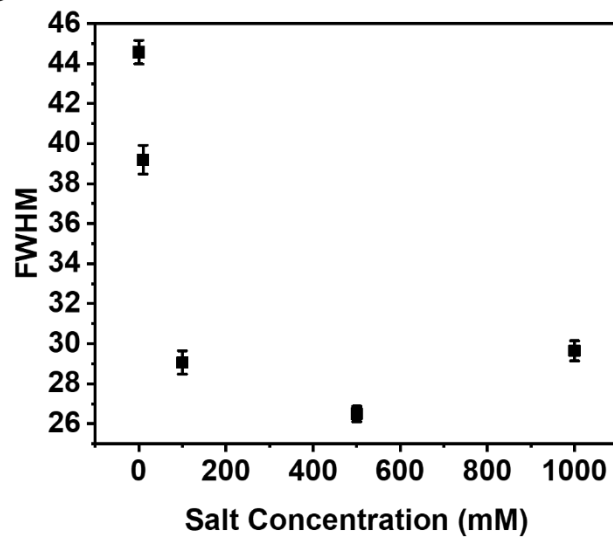
A**B****C**

Figure 4.5 Simulated chromatograms using Monte Carlo simulations. (A) Cartoon depicting contribution of two desorption rate constants on final elution profile line shape. (B) Peak aligned chromatograms simulated from 500,000 molecules using values extracted from CDF fits shown in Fig. 2B-D. (C) Measured FWHM of the peaks shown in B with error bars representing standard deviation of simulations performed five times with 100,000 molecules.

Our simulations illustrate broadening produced by our measured kinetic differences isolated from mobile phase effects. Experimental FPLC measurements (Figure 4.4) provide a convolution of both kinetic and mobile phase contributions to peak shape that cannot be separated empirically.³⁰³ By peak aligning, we remove elution contributions from the mobile phase time and varied retention times to emphasize the broadening effects predicted by desorption kinetics. Exclusion of other effects from the mobile phase guarantees that changes in the chromatographic shape arise from kinetic differences alone. Future advancements in the Monte Carlo model, as well as single-molecule tracking, will aid in deconvoluting instrumental contributions from chemical effects.

4.6. Conclusions

Single-molecule surface transport modes and kinetic analyses coupled with ensemble CD have guided a mechanistic explanation for increased separation efficiency observed in bulk separations during the salting out process. Predicting peak broadening from single-molecule kinetics is further supported by simulation of elution profiles. The increasing prevalence of single site adsorption-desorption of transferrin at nylon is directly

modulated with salt concentration (Figure 4.1). Increasing salt concentration led to an increase in adsorption and desorption kinetics at the nylon stationary phase (Figure 4.2). Electrostatic shielding likely dominated the adsorption rate increase, while the increased overall rate of desorption and increased waiting times are attributed to surface induced structural changes to transferrin induced at higher salt concentrations (Figure 4.3, SI *Appendix*, Fig. S8-10). Altered desorption kinetics from salting were not observed with fatty acid probe molecules,²⁷⁸ highlighting the complexity of large biomolecules that exhibit complicated dynamics such as unfolding . The reduction in chromatographic broadening found in ensemble separations of transferrin (Figure 4.4) is explained by a decrease in rare long-lived binding (Figure 4.2B) that drives a decrease in the CTRW motion (Figure 4.1). The utility of single-molecule tracking to mechanistically explain ensemble chromatographic observables is highlighted in our work. Further, our findings emphasize the importance of understanding the physiochemical changes salting out processes can have on protein behavior in bench-top and industrial scale separations. The design of stationary phase supports that suppress anomalous CTRW diffusion at the stationary phase will lead to improved separation efficiencies.

Polymer free volume effects on protein dynamics at polystyrene revealed by single-molecule spectroscopy

This work is under review at *Langmuir*.

5.1. Abstract

Protein-polymer interactions are critical to applications ranging from biomedical devices to chromatographic separations. The mechanistic relationship between the microstructure of polymer chains and protein interactions is challenging to quantify and not well studied. Here single-molecule microscopy is used to compare the dynamics of two model proteins, α -lactalbumin and lysozyme, at the interface of uncharged polystyrene with varied molecular weights. The two proteins exhibit different surface interaction mechanisms despite similar size and structure. α -lactalbumin exhibits interfacial adsorption-desorption with residence times that depend on polymer molecular weight. Lysozyme undergoes a continuous time random walk at the polystyrene surface

with residence times that also depend on the molecular weight of polystyrene. Single-molecule observables suggest the hindered continuous time random walk dynamics displayed by lysozyme are determined by the polystyrene free volume, a finding supported by thermal annealing and solvent quality studies. Hindered dynamics are dominated by short-range hydrophobic interactions where the contributions of electrostatic forces are negligible. This work establishes a relationship between the microscale structure (i.e. free volume) of polystyrene polymer chains to nanoscale interfacial protein dynamics.

5.2. Introduction

Advancing the understanding of structure-function relationships in protein-polymer interactions is critical in the design of biosensing devices,^{145,304} biocompatible implants,^{30,305} and protein separations.^{3,32,181} The adsorption of proteins to a polymer alters the material's function because the outermost layer of the material is comprised of proteins.³⁰ Polymers often experience protein accumulation when exposed to protein-rich environments, which has been shown to cause harmful side effects for patients³⁰⁶⁻³⁰⁷ or reduced functionality in everyday health care products, such as contact lenses.³⁰⁸⁻³⁰⁹ Surface modifications such as ligand grafting and UV exposure are used to suppress protein adsorption, while keeping the bulk polymer properties unchanged.^{158,160,310} Polymer chain architecture and packing densities are also used to modify polymer surface chemistries to reduce protein interactions,^{242,311-312} but further work is needed to understand and control the underlying polymer chemistry and physics that control protein surface interactions.

Polymer free volumes are the naturally occurring voids that are present in a polymer material, and depend on polymer chemistry and deposition conditions. The free volume of a polymer can have a dramatic effect on many physical characteristics such as the glass transition temperature,³¹³⁻³¹⁴ diffusivity in the polymer matrix,³¹⁵⁻³¹⁶ and the aging process.³¹⁷ Polymer free volume can be altered by mechanically compressing the polymer, thermally annealing,³¹⁸ and changing the molecular weight (MW) (i.e. chain length) of the polymer used to develop a film.³¹³ It has also been shown that using poor solvents with low solubility to dissolve polymers before deposition or spin casting can influence the free volume in bulk polymers.³¹³ However, there is little knowledge about how polymer free volumes effect protein dynamics at polymer interfaces. Understanding the relation between microscale polymer packing and protein behavior at polymer films could be invaluable in guiding the fabrication of improved materials.

Quantifying nanoscale protein dynamics at the surface of polymers is experimentally challenging. Many common techniques suffer from ensemble averaging^{26,319} or require *ex-situ* sample conditions to measure.^{114,320} Single-molecule fluorescence spectroscopy is a robust method for studying protein-polymer interactions allowing for many proteins to be tracked in real time below the diffraction limit of light.^{53,70,321} For example, Schwartz et al. showed how poly(ethylene glycol) (PEG) brush grafting decreased fibronectin adsorption, but longer PEG chains lead to more unfolding and longer residence times for adsorbed fibronectin.¹⁰¹ Other single-molecule studies have established relationships between the microstructures of polymer brushes^{182,310,322} and self-assembled monolayers^{81,86} with molecular probes, but a relationship between thin film

polymer packing and protein dynamics is lacking. Using total internal reflectance geometry^{24,124,244} achieves increased signal-to-noise by suppressing emission from molecules diffusing in the bulk. The utility of single-molecule fluorescence microscopy also has broader application to nanoparticle catalysis,²⁴³ live-cell imaging,³²³ and improving chromatographic separations.^{20,324-325}

In this study, we compare the surface dynamics of two oppositely charged proteins, lysozyme (Lys, positive)³²⁶ and α -lactalbumin (α -LA, negative)³²⁷ at thin uncharged polystyrene (PS)³²⁸ films with varied free volumes. Lys and α -LA are of interest given their common use as model proteins^{23,80,329-331} and their similarities in size and structure.³³²⁻³³³ PS is chosen because the variation in PS free volume is well studied^{18, 47-48} and because of its use in common applications.^{186,188,334} Lys and α -LA are found to exhibit different types of motion at PS surfaces. α -LA undergoes single site adsorption-desorption at PS, with a MW dependence on surface residence times. Lys undergoes non-Brownian surface transport known as a continuous time random walk (CTRW), where adsorption occurs at non-specific sites for random periods of time interrupted by desorption to nearby sites.^{242,335-336} The Lys CTRW dynamics depend on the MW of the PS film, with fewer hops and smaller hop sizes at higher MWs. We propose the observed MW dependence on Lys dynamics is caused by the free volumes among PS chains in the deposited films.³¹³ This interpretation is supported by thermal annealing studies as well as changing solvent quality. Lastly, PS is doped with a hydrophilic polymer (methoxypolyethylene glycol) to determine that short-range hydrophobic interactions dominate the hindered Lys dynamics on PS with varied free volumes.²⁷⁹ Further, tracking results under varied ionic conditions

suggest that electrostatic forces do not contribute to varied Lys dynamics at PS. We envision this single-molecule approach can be widely applied for the observation of many protein surface interactions to develop more robust materials for specific applications in protein-rich environments.

5.3. Materials and Methods

5.3.1. Preparation of polymer films

Borosilicate glass coverslips (22 × 22 mm, VWR) are thoroughly cleaned by sequentially sonicating in water, ethanol, and acetone. Coverslips are then placed in a piranha bath (28% NH_4OH and 30% H_2O_2) heated at 80°C for 20 min. After rinsing with deionized water ($>1 \text{ M}\Omega\cdot\text{cm}$) and drying with N_2 gas (Ultrapure, Airgas), the coverslips are further treated with oxygen plasma (Harrick Plasma, PDC-32G) for 2 min. Thin PS films are prepared by spinning coating (SPI KW-4A) a 1 w/w % of PS/toluene or PS/cyclohexane solution at 3,000 rpm for 1 min. PS of various MWs 3k (Polymer Source, PDI:1.09), 36k (Polymer Source, PDI: 1.05), and 1500k (Polymer Source, PDI:1.10) are prepared using the spin coating protocol. The surface roughness of resulting films is measured by atomic force microscopy (Bruker, Multimode 8) operated in peak force tapping mode.

5.3.2. Polymer thickness and refractive index characterization

For all molecular weights (3k, 36k, and 1500k), annealed PS, and solvent adjusted films solutions of 1 w/w % PS/toluene or cyclohexane are coated (100 μ L) at 3000 RPM for 1 min onto cleaned silicon wafers (Silicon Quest Int'l, Prime Grade) with a spin coater (Laurell WS-650MZ-23NPPB). Resulting film thicknesses and refractive indices are measured with a J.A. Woollam M-2000 ellipsometer scanning from 350 nm to 1050 nm. Data was fit with Cauchy thin film model resulting in a mean squared error of less than 5 percent for all measurements and the results are presented in Table S1.

5.3.3. Film annealing and modification

A hotplate is placed inside a glove bag filled with N₂ gas (Ultrapure, Airgas). After placing the PS samples onto the hotplate, the temperature is elevated to 120°C for 4 hrs. Once finished, the PS samples are cooled to room temperature under an N₂ atmosphere.

5.3.4. mPEG Doping of PS

The hydrophilic films are prepared by spin coating clean coverslips with 1 w/w % toluene solution containing PS and methoxypolyethylene glycol (mPEG) with a weight ratio of 9:1, using the same conditions described above for the pure PS samples. AFM imaging (Bruker, Multimode 8) of mPEG/PS films is performed in tapping mode to acquire phase images for determining the spatial surface coverage of mPEG domains (Fig. S1). Results indicate mPEG domains are highly uniform in the mPEG/PS films.

5.3.5. Protein Dilutions and fluorescence labeling

Lyophilized lysozyme (pI=10.7)^{211,326} that is labeled with rhodamine B (Structure Fig. S2) is purchased from Nanocs as previously described.²⁴² Alexa 555 (Structure Fig. S2) labeled α -LA (pI=4.2),^{327,337} previously purified and acquired from the Wilson Group at the University of Houston is used here.²⁴ For experiments, α -LA and Lys are diluted in 10 mM HEPES buffer (pH=7.2) to form 3.5 nM and 35 nM solutions respectively.

5.3.6. Protein surface charge and hydrodynamic measurements

A Malvern zetasizer (Zen 3600 Nanoseries) is used to measure the zeta potentials and hydrodynamic radii of α -LA and Lys in 100 mM HEPES at pH 7.2. Zeta potential experiments are performed in Malvern cuvettes (DTS1070) with the average and standard deviation of 35 measurements reported. Hydrodynamic radii values from 13 measurements are quantified with the average and standard deviation. All measurements are taken at 25 °C after 2 minutes of equilibration.

5.3.7. Single-molecule measurements

A custom-built total internal reflection fluorescence (TIRF) microscope is used for single-molecule fluorescence measurements. A 532 nm laser (Coherent, Compass 315M-100SL) is circularly polarized and passed through a 100 \times oil-immersion objective (Carl Zeiss, Alpha Plan-Fluar, NA=1.45) to excite the labeled proteins. The excitation light is focused onto a 30 \times 20 μm^2 area. The fluorescence signal from the proteins is collected

by the same objective, filtered by two filters (Kaiser, HNPF-532.0-1.0 and Chroma, ET585/65m), and then collected by an electron- multiplying charged coupled device (Andor, iXon 897) cooled at -70°C and operated at 33.33 Hz. The transmittance of PS is greater than 85%, with a refractive index of 1.58,³³⁸ therefore, TIRF excitation takes place at the PS aqueous interface as previously shown (Fig. S3).²⁴² The evanescent field in our TIRF geometry has a maximum penetration depth of 200 nm,⁵³ thus only fluorescent probes near the polymer surface are excited. Prior to measurements, the observation area is photobleached with laser excitation for 30 minutes removing any fluorescent signal from contaminants present in the film. For single-molecule experiments, either α -LA or Lys solution (1 mL) is drop-cast onto the polymer film covering an area greater than the area illuminated by laser light.

5.3.8. Protein molecule identification and tracking

An established tracking algorithm is used to identify and track both α -LA and Lys molecules.³³⁹ This Matlab-based program has three fundamental steps for tracking single-molecules below the diffraction limit of light: increase signal-to-noise, identify molecules, and utilize a maximum likelihood algorithm to generate single-molecule trajectories.³³⁹ The TROIKA tracking program is available at <https://github.com/LandesLab/Troika-Single-particle-tracking>.

5.4. Results and Discussion

5.4.1. α -LA adsorption and dynamics at PS surface

Super-localization imaging of α -LA adsorption events shows that α -LA undergoes interfacial adsorption/desorption at the PS surface, with a localization uncertainty of 20 nm (Figure 5.1).⁵³ Individual adsorbed negatively charged α -LA molecules ($\zeta = -18 \pm 7$ mV)³²⁷ are observed at the PS surface once α -LA solution is added to the PS (Fig. S3). Adsorption events appear to be stationary over multiple frames, and within our spatial resolution^{180,325} before disappearance due to desorption,⁵³ suggesting the α -LA molecules adsorb to nonspecific surface sites on the PS. For adsorption events lasting more than one frame, each corresponding point spread function is fit to a 2D Gaussian distribution in each individual frame to extract the central localizations (Figure 5.1A). To increase statistics, the central localizations from 20 different α -LA molecules are compiled by aligning their centers of mass (Figure 5.1B).³⁴⁰⁻³⁴¹ The resulting 2D histogram is further fit by another 2D Gaussian, resulting in a full width half maximum of 20 nm. This value is equivalent to the resolution limit of other commonly known super-resolution techniques such as PALM,⁴¹ STORM,³⁴² and mbPAINT⁶⁰ suggesting α -LA molecules are stationary at the PS surface. Single-molecule tracking also corroborates the super-localization findings, which are discussed next.

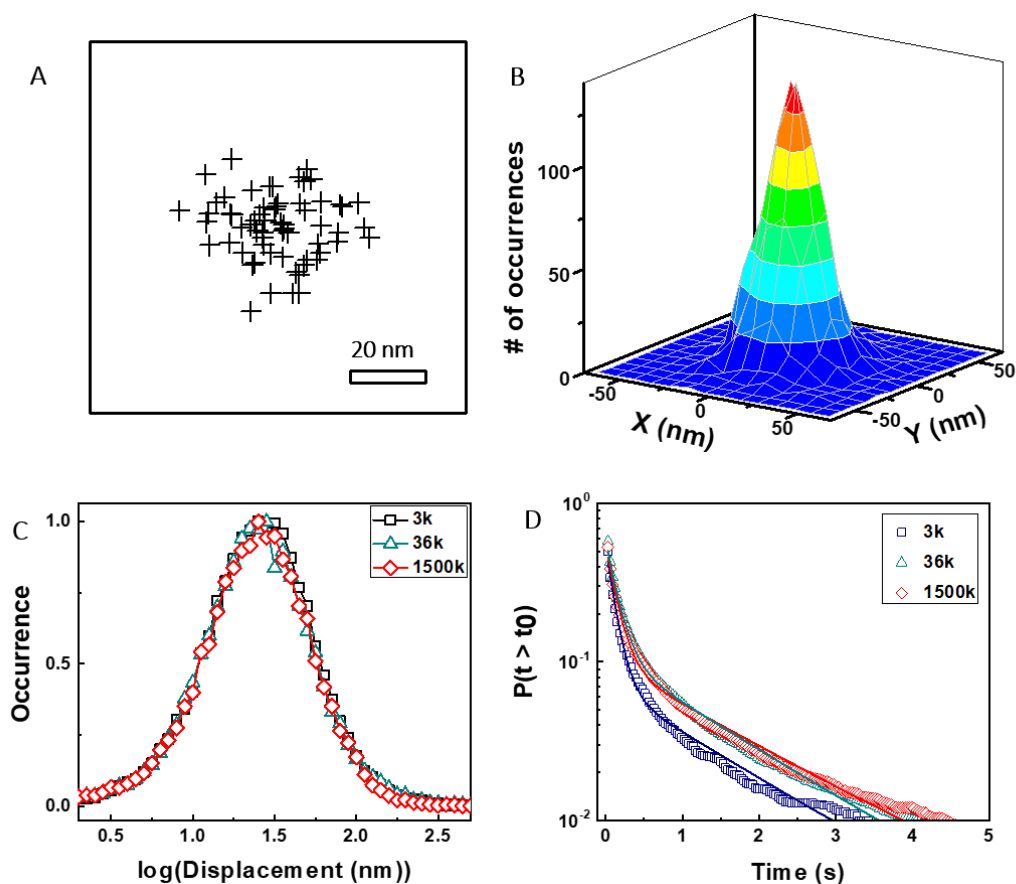


Figure 5.1 α -LA adsorption and dynamics at PS films. (A) The central localization for a single α -LA in 63 consecutive frames. (B) 2D histogram of combined central localizations from 20 α -LA molecules. (C) Single frame displacement distributions for α -LA adsorbed onto PS films with varied PS MWs. (D) α -LA surface residence time cumulative distributions fit to Equation 4.2 (solid lines).

Single-molecule tracking further confirms α -LA molecules are stationary over multiple frames, and within our resolution limit^{180,325} upon adsorption at PS independent of MW. The MW of the PS films is varied from 3k up to 1500k to assess the role of varied PS free volume on the immobile α -LA molecules.³¹³ Single frame displacement

distributions allow for the frame to frame displacements to be quantified from single-molecule trajectories (Figure 5.1C). The distributions of single frame displacements from hundreds of α -LA molecules result in one peak centered at 24 nm (inverse log, $10^{1.38}$), which is independent of the PS MW (Figure 5.1C). It is expected that the interfacial chemical identities of all three MW PS films are similar given the solvent, concentration, and spin coating processes are identical for all three MWs. Peak values from single frame distributions closely match our localization uncertainty results in Figure 5.1A-B and values reported in previous studies.⁸¹

α -LA surface residence times depend on the MW of the underlying PS, as shown in Figure 5.1D. The cumulative distributions of surface residence times for α -LA indicate that the time spent on the surface increases as the MW increases. Residence time distributions are fit to a two-term exponential: $P(t) = A_1 e^{-k_1 t} + A_2 e^{-k_2 t}$ (Equation 4.2)²⁴⁶ to extract desorption rate constants as a function of PS MW (Table S2). Two-term exponential decay fits to residence time distributions have been shown to resolve the kinetics of folded and unfolded proteins populations,³²⁵ resolve DNA hybridization kinetics,¹⁷² and quantify the desorption kinetics from weak and strong adsorption sites intrinsic on polymer surfaces.¹⁸⁰ Here it is likely that anomalously strong sites exist on the PS surface due to the chemical stability of the globular proteins used here.³⁴³ Decreased desorption rate constants observed at higher MWs suggest that longer PS chains induce stronger α -LA-PS interactions, thereby increasing the prevalence of long-lived adsorption events (Figure 5.1D). It has been shown that PS chains are more densely packed and more coiled as the MW of PS is increased in a deposited PS film (Table S1).³⁴⁴ Therefore, we

predict the number of short-range interactions (i.e. Van der Waals, hydrogen bonding, and hydrophobic interactions) present between α -LA and PS increases in the more coiled PS at higher MWs. This hypothesis is supported by the findings of Schwartz and co-workers, which suggests the desorption of proteins from interfaces is dictated by short-range interactions rather than long range interactions.²⁷⁹ Therefore, tracking results indicate that desorption kinetics of α -LA are related to interactions with the underlying microscale organization of PS chains.

5.4.2. Adsorption of Lys on pure PS surface

Lys dynamics at PS are non-Brownian, and exhibit CTRW behavior,³⁴⁵ with surface transport dynamics that are dependent on the MW of PS. This result is surprising given the similarity in sizes ($R_h=1.6 \pm 0.3$ nm and $R_h=1.5 \pm 0.2$ nm for Lys and α -LA respectively),^{211,337} structures,³³²⁻³³³ and biological ancestries³⁴⁶⁻³⁴⁸ of Lys and α -LA (Fig. S4). Representative trajectories are shown in Figure 5.2A to illustrate the CTRW motion of the positively charged Lys ($\zeta=12 \pm 6$ mV)³²⁶ at PS. The trajectories highlight the heterogeneity exhibited by individual Lys molecules at PS. Large areas of the PS surface are explored with brief periods of immobility at non-specific adsorption sites as is typical of CTRW dynamics. The difference in Lys and α -LA dynamics is likely driven by the decreased affinity Lys exhibits for the PS surface, allowing Lys to explore the PS surface. A tenfold higher concentration of Lys is needed to acquire similar surface coverage observed for α -LA at PS. The difference in adsorption strengths of α -LA and Lys are not attributed to the different dye labels used here (Fig S5). The CTRW mechanism of proteins

at polymers has been observed by others at the single-molecule level.⁸⁰ Lys waiting time distributions, the time spent at each adsorption site, are analyzed and fit to a power law to verify the presence of the CTRW mechanism (Fig. S6).⁷⁹ Waiting time distributions would be normally distributed if Lys surface motion were Brownian.³³⁶ CTRW transport displays periods of immobility interrupted by desorption into the bulk punctuated by the adsorption to a new surface site. Single frame displacement distributions quantify the hopping distances in the CTRW as Lys molecules travel to new sites on PS (Figure 5.2B). Single frame displacement distributions show a clear dependence on the MW of the underlying PS film (Figure 5.2B). The decrease in hopping distances as MW is increased indicates that the mobility of Lys at PS is highly dependent on the chain structure of PS. We suggest that the packing of the PS chains (Table S1) discussed in the context of free volumes has a direct impact on the distance between available adsorption sites on PS for Lys adsorption to occur (Scheme 1). The thicknesses of resulting PS films are quantified as a function of MW (Table S1) which shows that film thickness does not increase from 3k to 36k. An increase in film thickness is observed for the 1500k MW, however we conclude that film thickness may not play a major role in protein dynamics PS surfaces given no height change is observed from 3k to 36k accompanied with a decrease in Lys mobility (Figure 5.2B). It must be noted at the highest MW condition, Lys is still highly mobile in comparison to α -LA shown in Fig. 2B (black). In addition to the frame to frame displacements, hopping behavior is also quantified at the PS interfaces with varied MW.

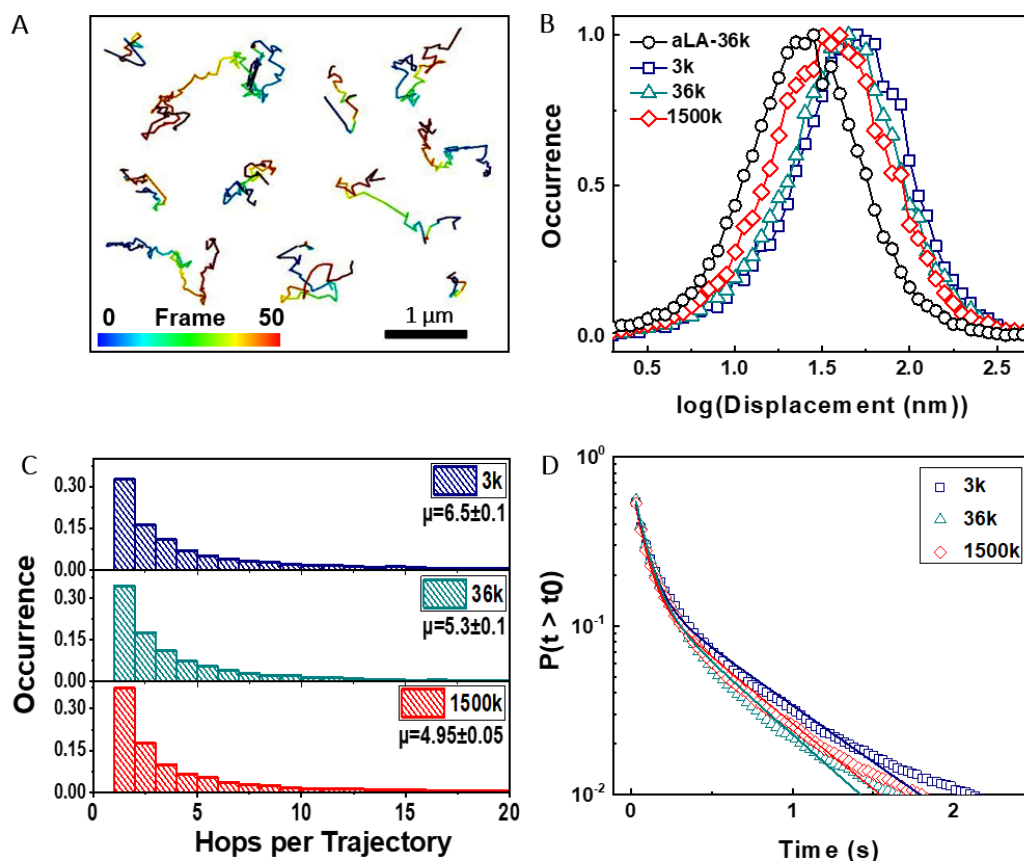


Figure 5.2 Lys adsorption and dynamics at PS films. (A) Representative trajectories of single Lys at the interface of PS (MW=36k) with color map representing frame number for each trajectory. (B) Single frame displacement distributions for Lys on PS films with varied MWs. $\alpha\text{-LA}$ distribution shown for comparison. (C) Lys hopping distributions with the calculated mean and standard error of the mean at each MW of PS. (D) Cumulative distribution of surface residence time for Lys with fits to Equation 4.2 shown in the solid lines.

Lys explores fewer adsorption sites at high MW PS with no change in the overall surface residence time, driven by an increase in waiting times at each adsorption site. The number of hops per trajectory is quantified in Figure 5.2C using the previously described

filtering process,³²⁵ where a hop is defined as a frame to frame displacement greater than our spatial resolution of 20 nm. Fewer hops per trajectory are observed in Figure 5.2C with increasing MW, indicating that Lys is less likely to readsorb to PS after desorption at higher MWs. Interestingly, the total surface residence time of Lys (Figure 5.2D) and the extracted desorption rate constants (Table S3) do not change as a function of MW. Waiting time analyses show that as the MW is increased Lys spends more time per site before desorbing to a nearby site (Fig. S6). Power law fits of waiting time distributions result in exponents of -2.02 ± 0.01 , -1.84 ± 0.02 , and -1.71 ± 0.02 for MWs of 3k, 36k, and 1500k respectively (Fig. S6). Although, Lys interacts with fewer adsorption sites during the CTRW as MW increases (Figure 5.2C) Lys spends more time at each site (Fig. S6) accounting for the same total residence times for Lys at all MWs (Figure 5.2D). Single-molecule tracking allows for mechanistic details in the Lys CTRW to be related to the underlying free volumes in the PS films. To further confirm the impact of polymer free volume on the CTRW exhibited by Lys, two well-known methods, thermal annealing and adjusting solvent quality, are utilized to vary PS free volumes.

5.4.3. Lys adsorption at Annealed and Cyclohexane developed PS films

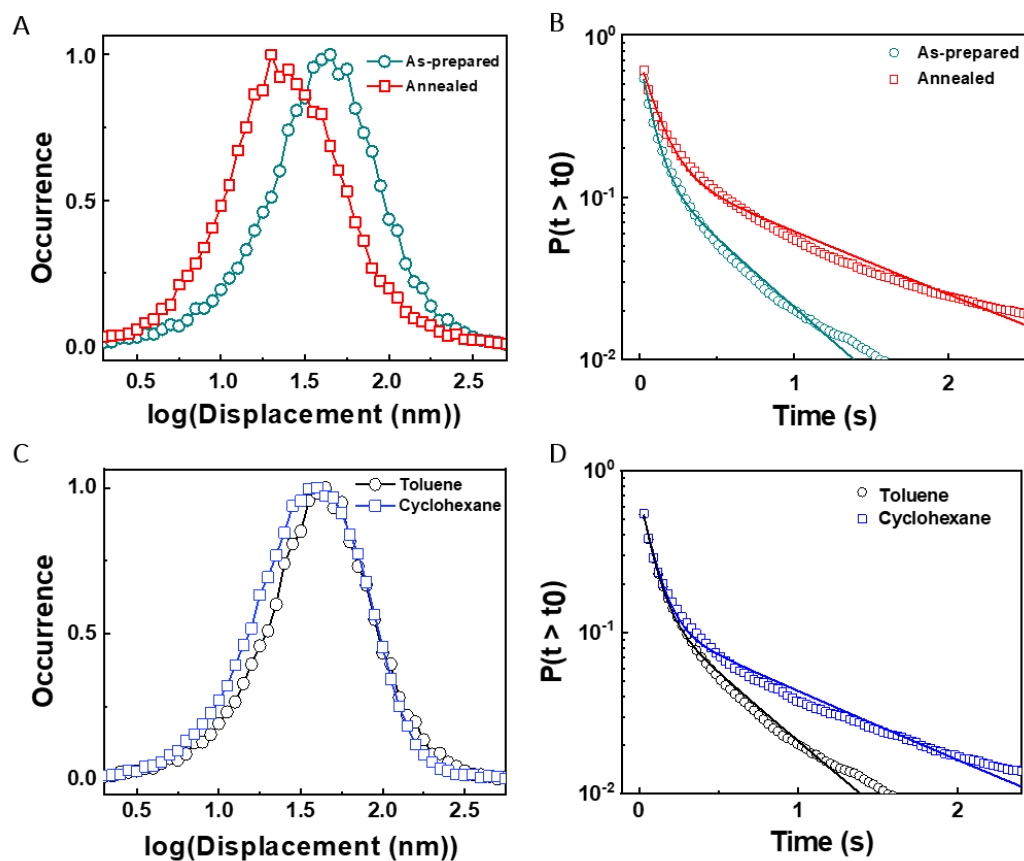


Figure 5.3 Lys dynamics at thermally annealed and cyclohexane developed PS films. (A) Single frame displacement distributions for as-prepared and thermally annealed PS films. (B) Surface residence time distributions for as-prepared and thermally annealed PS films with fit to Equation 4.2 shown with solid lines. (C) Single frame displacement distributions for toluene and cyclohexane developed PS. (D) Surface residence time distributions for toluene and cyclohexane developed PS films with fit to Equation 4.2 shown with solid lines.

Lys dynamics at annealed PS show decreased single frame displacements accompanied by increased surface residence times (Figure 5.3A-B). Thermally annealing PS films results in decreased free volumes through chain relaxation,³⁴⁹ similar to increased MWs discussed above. Annealing allows us to further establish the relationship between PS free volumes and varied Lys CTRW dynamics. The annealing process is performed in inert nitrogen in order to minimize any chemical modifications to PS but these effects cannot be completely ruled out. A shift in the single frame displacement distributions is observed from peak values at 44 nm and 20 nm for as-prepared (MW=36k) and thermally annealed PS films respectively (Fig. 3A, MW=36k). The shift in single frame hopping distances indicates that as PS chains pack more densely, Lys travels shorter distances to readsorb to the surface. The decrease in displacements with annealing (Figure 5.3A) is similar to the decrease observed with increased MW (Figure 5.2B), where decreased free volume leads to smaller displacements (Figure 5.2B). AFM imaging results indicate that mPEG domains are highly uniform within the PS films (Fig. S1). If long range hopping does exist as a result of large isolated mPEG domains it would not be detected given diffusion in the bulk would be faster than our detectors temporal resolution and/or outside of the evanescent field present in our TIRF illumination geometry.¹⁷² Annealing and MW displacement distributions confirm the hypothesis that as PS chains are packed more densely (Table S1) the distance between adsorption sites decreases, thereby leading to shorter displacements. Lys surface residence time increased as a result of thermally annealing PS (Figure 5.3B, Table S4). The increase in total Lys residence time with annealing (Figure 5.3B) is not observed in the case of increased MWs (Figure 5.2B).

Annealing PS could induce different surface morphologies,³⁵⁰ however, no statistical difference in surface roughness is found between the as-prepared and annealed PS surfaces (Fig. S7). One likely explanation for observed increases in residence times on the annealed PS is the result of a greater reduction in PS free volume with annealing in comparison to increased MW (Figure 5.2), thereby leading to more short-range interactions between Lys and PS (Scheme 1). This hypothesis is supported by the more severe shift in displacements observed at annealed PS centered at 20 nm (Figure 5.3A) in comparison to 39 nm in the highest MW condition (Figure 5.2B). Additionally the largest refractive index was measured for the annealed PS films confirming the greatest increase in chain density which can be related to decreased free volumes in thin films.³⁵¹ Minimal film thickness changes were observed as a result of annealing. To further support the structure-function relationship in PS free volume to Lys CTRW dynamics a poor solvent is investigated for the development of PS films.

Decreased Lys hopping distances are observed on the PS films developed in a poor solvent in addition to an increased surface residence time, aligning with the observations seen in the annealing conditions. Decreasing solvent quality to decrease polymer chain free volumes is well studied, in particular using cyclohexane to develop PS films.³⁵²⁻³⁵³ Decreased free volumes in resulting PS films using a poor solvent is driven by decreased PS solubility in the cyclohexane. A decrease in hopping distances from a peak maximum at 44 nm to 39 nm is observed from the toluene (MW=36k) to cyclohexane deposited PS respectively (Fig. 3C, MW=36k). Our observations of Lys surface dynamics establish that the distance between adsorption sites for Lys is dictated by the size of free volumes present

in a PS film. The change observed for single frame displacements with cyclohexane deposited PS is the same magnitude observed in the case of varied MW (Figure 5.2B). However, we observe an increase in residence time of Lys as the PS chain density is increased (Figure 5.3D, Table S5) similar to that observed on the thermally annealed PS (Figure 5.3B, Table S4). We predict increased residence time is driven by an increased number of short-range interactions between the PS chains and Lys. To further develop the mechanistic understanding of hindered CTRW dynamics exhibited by Lys at PS, the dominant short-range interaction driving hindered CTRW dynamics is investigated next.

5.4.4. Lys dynamics at mPEG doped PS films

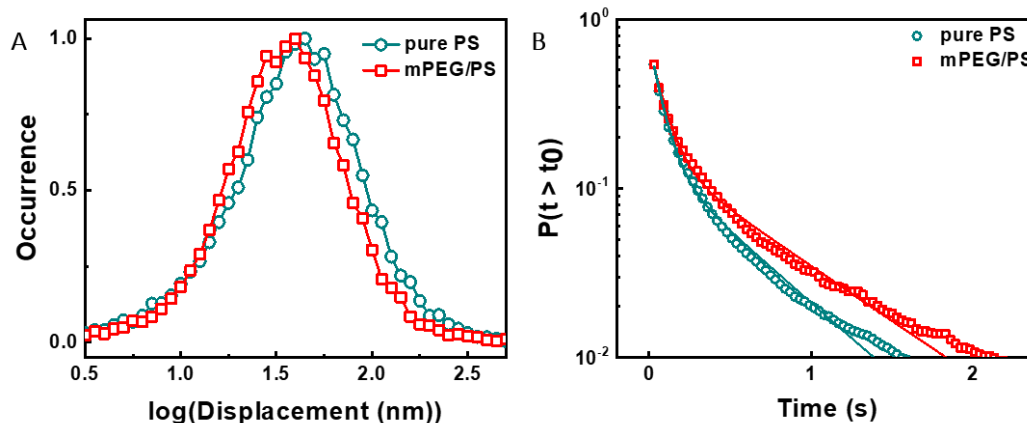


Figure 5.4 Comparison of Lys dynamics at as-prepared and mPEG doped PS films. (A) The distributions of single frame displacements at as-prepared and mPEG doped PS films. (D) Cumulative distribution of surface residence time for Lys adsorption at as-prepared and mPEG doped PS films. Solid lines are fits to Equation 4.2.

Tracking results under altered solution and PS film chemistries suggest that hydrophobic effects, rather than electrostatic effects, are the primary driver of the hindered CTRW dynamics at PS. The contributions of electrostatics in our observed dynamics are tested with the addition of 20 mM and 100 mM NaCl during Lys tracking at the PS interface (Fig. S8). Although PS chains carry no charge,³²⁸ Lys carries a net positive charge at our experimental conditions (pH=7.2) and the presence of PS impurities could not be ruled out. Single frame displacement results indicate that electrostatics are not the dominant driving force in the observed CTRW Lys dynamics (Fig. S8). To evaluate the effect of hydrophobic interactions, PS (MW=36k) is doped with 10 w/w% mPEG to increase the hydrophilicity of the PS film.³⁵⁴ Single frame displacement distributions show a decrease from 44 nm to 39 nm as the surface becomes more hydrophilic with mPEG doping (Figure 5.4A). An increase in surface residence time is observed on the more hydrophilic doped PS film (Figure 5.4B, Table S6). Single frame distributions and residence time distribution changes with mPEG doping align well with observed Lys dynamics as a function of MW, thermal annealing, and solvent at PS surfaces. Therefore, we suggest hydrophobics to be the dominating force in the interactions of Lys at PS. Our previous study of Lys at functionalized PS interfaces also reveals that hydrophobics dominate hindered Lys CTRW dynamics as PS becomes more hydrophilic.²⁴² Previous work shows that hydrophobics can also play a large role in 3D transport dynamics in porous media.³⁵⁵ Here, a more careful look at single protein tracking results suggests that the underlying microstructure of PS yields similar effects without the introduction of new charge carrying chemistries to PS.²⁴² Although similar results and driving forces are at play in both cases, here we uncover a

structure-function relationship present in Lys dynamics at PS without modifying the overall hydrophobicity of the thin PS film (Figure 5.1-5.3). It must be noted that contributions from Van der Waals forces, changes in free volumes from mPEG doping, and hydrogen bonding cannot be ruled out as contributors as well. However, based on our single-molecule observables Van Der Waals forces and hydrogen bonding are likely minor contributors based on the decrease in hopping distances and the increase in residence times, which align with observables from MW, annealing, and solvent quality.

5.5. Conclusion

Here single-molecule tracking and super-localization microscopy are used to establish a relationship between the underlying PS free volume to the dynamics of two proteins α -LA and Lys. Super-resolution imaging, along with the single-molecule tracking, verify α -LA molecules are immobilized at nonspecific adsorption sites with increased residence times as PS free volumes decrease as a function of PS MWs. Although Lys is similar in size and structure to α -LA, Lys molecules exhibit a CTRW at PS. The mechanism of Lys CTRW transport, hopping dynamics, and single site waiting times are dependent on the underlying MW of PS. We propose the varied CTRW dynamics exhibited by Lys are likely caused by the variation in PS free volumes in the films with different MWs. This hypothesis is further supported by decreasing PS free volumes with thermal annealing and adjusting solvent quality, both resulting in smaller free volumes and increased PS chain packing. Displacement distributions at the annealed and solvent modified PS corroborate the relationship between hindered CTRW dynamics and decreased PS free volumes.

Longer residence times were observed for Lys at the annealed and decreased solvent quality PS attributed to more severe reductions in PS free volumes in comparison to varied MW, thereby introducing more short-range interactions between Lys and PS. Lastly, the dominant force driving hindered CTRW dynamics at PS as free volumes decreased is interpreted to be hydrophobics with minimal contributions from electrostatic forces. The distinct dynamics exhibited by two structurally and biological related model proteins on chemically identical surfaces illustrate the complexity in protein-polymer interactions. More specifically we highlight the relation between underlying free volumes in a commonly utilized polymer film, PS, to nanoscale protein transport dynamics. Our findings here can have broad impacts on the design of application-specific polymer materials³⁰ where suppressing anomalous surface diffusion would be advantageous for decreasing the prevalence of protein unfolding and denaturation at strong adsorption sites⁸⁰ and improving protein separation efficiencies.³²⁵

Conclusion and Future Outlooks

6.1. Overall Conclusions

In this thesis, single-molecule fluorescence microscopy is used to directly image the dynamics of proteins at industrially relevant stationary phase polymer supports. By quantifying protein dynamics at the solid-liquid interface of polymer supports we were able to resolve the heterogeneous interactions of proteins in a high throughput fashion removing the bias of ensemble averaging. Observations presented here allow for mechanistic details in protein-polymer interactions to be resolved at the nanoscale. These results can inform the design of polymer-based materials for specific applications, such as improving biological-based protein separations at the bench-top and industrial scales.

At the interface of PS, a commonly used polymer material, we showed that proteins will undergo non-Brownian surface transport known as a CTRW. The transport at PS was found to be highly dependent on both the surface chemistries used to functionalize PS and the overall hydrophilicity of the PS films. Overall as the

wettability of PS was increased the mobility of the CTRW dynamics was greatly hindered, leading to highly immobile interactions at the PS interface. The hindered dynamics were attributed to short-range interactions, such as hydrophobics and the formation of water hydration layers, not long-range electrostatic interactions.

Next, we showed that another protein, transferrin, undergoes both CTRW and single-site adsorption desorption dynamics at industrially relevant nylon 6,6. The ratios of transferrin molecules undergoing the two interaction types were tuned with the ionic strength to emulate salting out a chromatographic separation. As salt concentration was increased the prevalence of CTRW trajectories was decreased. This decrease in CTRW dynamics and the corresponding desorption kinetics were related to improved separation efficiencies observed in membrane based FPLC separations of transferrin. Structural changes induced to transferrin at the nylon interface were also observed as salt increased. For the first time improvements in separations at the bulk scale are related and confirmed theoretically with simulations informed by single-molecule kinetics.

Lastly, the underlying packing of polymer chains in PS films were shown to hinder CTRW dynamics similar to that observed with functionalization methods in a previous chapter. Using varied molecular weights, thermal annealing, and decreased solvent quality it was observed that the free volumes in thin films has a direct impact on the dynamics of proteins. These observables are important to further

expand the relation between polymer chemistries and physics to the behavior of proteins at these industrially relevant polymer materials.

6.2. Future Directions

The future of this project will use advanced microscopy methods to uncover the multiscale dynamics occurring in separation systems. This will likely include the use of 3D imaging and methods such as STReM²⁴ that improve the temporal resolution of single-molecule tracking in order to resolve fast dynamics that likely impact separations. With the advancement in sensitive photodetectors and optical techniques the spatial and temporal limits of the presented methods will likely be pushed to uncover transport dynamics in more complex materials used in separation. This can include stimuli responsive polymer materials and highly porous membrane networks heavily utilized in industrial biologic separations. Lastly, uncovering how protein competition effects separations and overall elution's by directly observing Vroman protein dynamics can further inform and help predict separations at the nanoscale, eliminating the need to empirically optimize industrial separations.

The methods covered in this thesis have a wide array of applications that can be applied to systems beyond biologic separations. This could include but not be limited to implant material development, anti-fouling materials, and advanced food storage materials.

SI Appendices

7.1. Appendix to Chapter 2: Variable Lys transport dynamics on oxidatively functionalized polystyrene films

Polystyrene Film Thicknesses

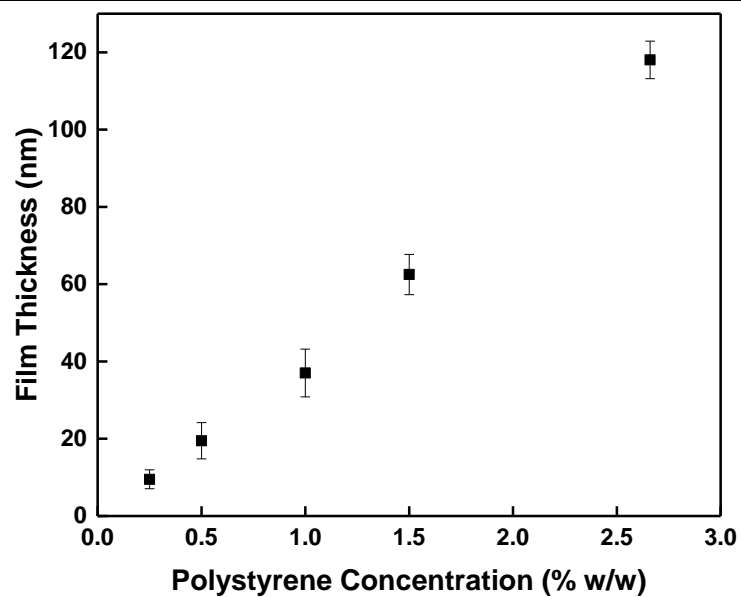


Figure S1. Polystyrene film thicknesses vs. polymer concentration in toluene solution represented in weight/weight percent. Error bars are the standard deviation of 12 measurements from different regions on at least four separate samples per data point.

Single Particle Tracking Algorithm

Our custom tracking algorithm was written in Matlab R2011b and has been previously published elsewhere.²⁸ In short, our data consisted of a three dimensional matrix for each stack of 1,000 frames, in which each slice of the matrix corresponded to one exposure time of our EMCCD camera capturing a 2D image. Our tracking algorithm analyzes the collected data series in three general steps. The first step increases the signal to noise ratio (SNR) of each frame within the data series by applying a local averaging method which utilizes a 3x3 matrix of ones to increase the SNR. This step results in roughly a 2 to 3 times increase in SNR. Next, the de-noised data is used in order to locate particles frame by frame. This is accomplished by determining a local background intensity on a 50 x 50 pixel region iteratively on each 512 x 512 image and applying a radial symmetry function to corresponding point spread functions of each emitter to achieve sub-pixel localization. Lastly, mapping of particle trajectories from frame to frame is performed using a nearest neighbor method. The search radius for the nearest neighbor mapping is user defined and was set to 6 pixels in our analysis. This was also combined with a trajectory length filter of 4 frames assuring that only trajectories lasting more than 4 frames were included for data analysis. These parameters were implemented in order to minimize false trajectory linkages in combination with low probe concentrations. Moreover, we justified these tracking parameters by randomly shuffling 10 stacks of data and determining the number of false trajectories identified based on search radius and filter size with less than a 5%

false identification rate in comparison to the original number of identified trajectories in each stack. This was implemented in addition to using very low probe concentrations throughout the study. A more thorough explanation of our tracking algorithm implemented can be found in reference 1.

Contact angle measurements for UV treated polystyrene

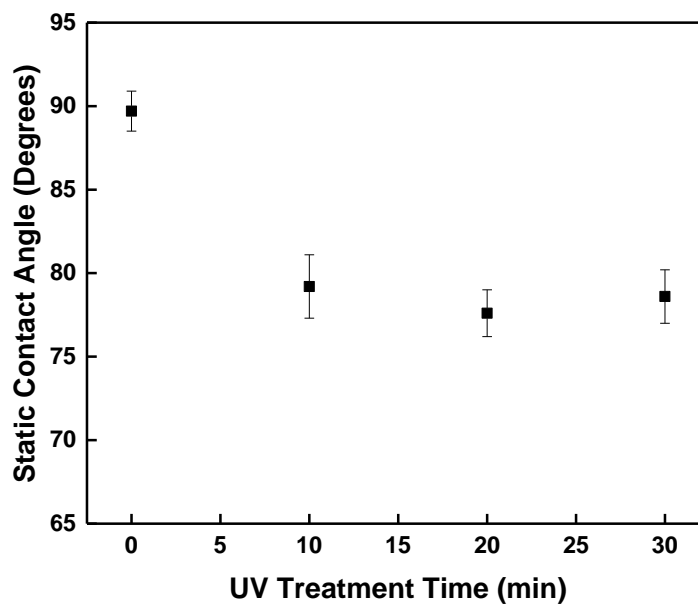
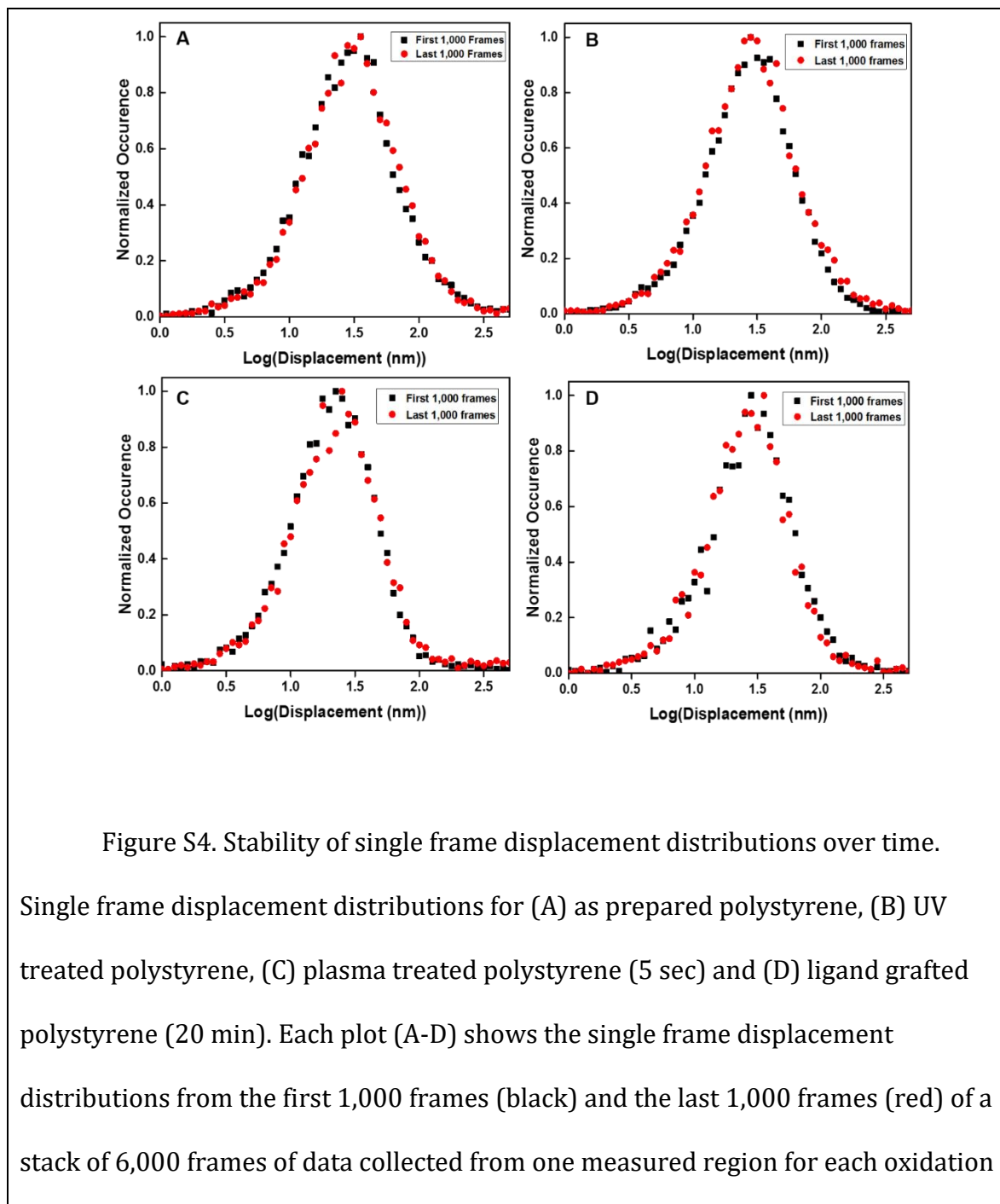


Figure S3. Static water contact angle for UV treated polystyrene films. Each data point represents contact angle from 8 measurements from two different samples. The error bars represent the standard deviation of all the measurements for each condition.

Single frame displacement distributions stability



method. This indicates that the distributions are not time dependent given the time between each data set represented is roughly 10 minutes.

Cumulative distribution of surface residence times for UV treated polystyrene

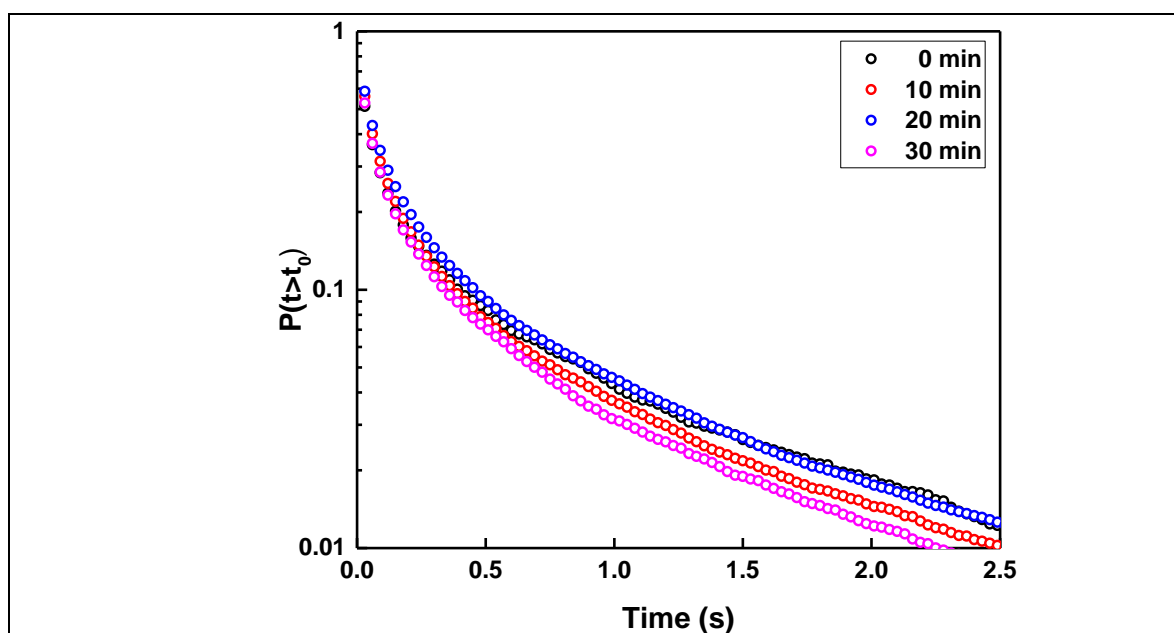


Figure S5. Cumulative distributions of surface residence times for lysozyme binding events on UV exposed polystyrene interface. Each condition represented here is at least 800 trajectories per treatment time and indicates a very small deviation in surface residence times of adsorbed lysozyme molecules after UV treatment of the polystyrene interface.

Lysozyme trajectories on UV treated polystyrene and Trajectory's radius of gyration values

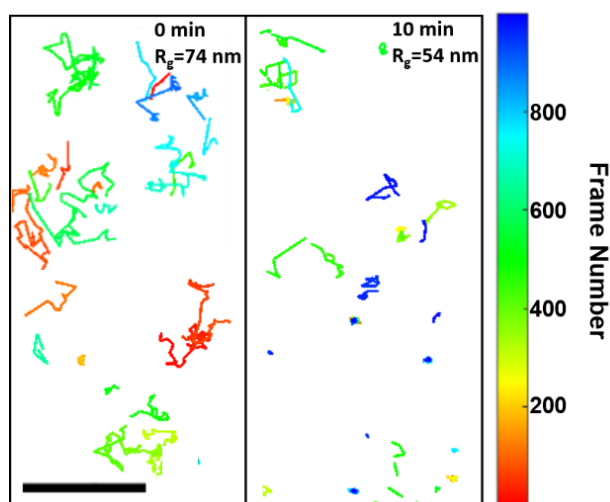


Figure S6. Representative time dependent lysozyme trajectories from 1,000 frames of data for corresponding UV treatment times (Scale bar is representative of 2 μm). Included is the average trajectory's radius of gyration for at least 800 trajectories for each condition.

Trajectory's radius of gyration Analysis Mathematics

A trajectory's radius of gyration can be used in order to determine the area explored by a tracked molecule. This method has been previously implemented in other single molecule studies undergoing non-Brownian motion.^{85,203,356} The trajectory's radius of gyration (R_g) is calculated for each step of a trajectory using the following Equation 7.1 and Equation 7.2:

$$R_g = \sqrt{R_1^2 + R_2^2}$$

Equation 7.1 Radius of Gyration

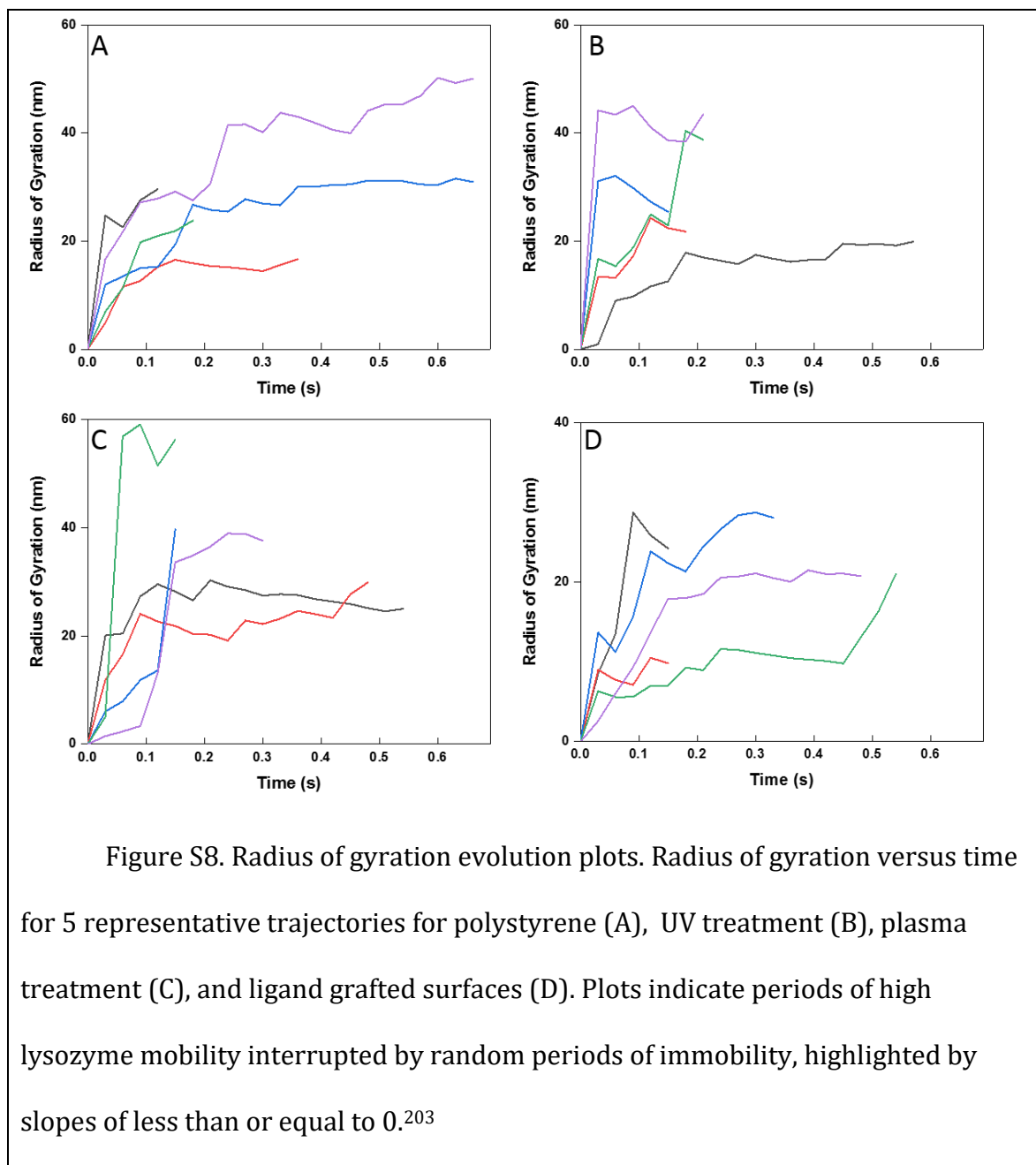
in which R_1 and R_2 are the major and minor eigenvalues of the two by two matrix tensor (T) for the trajectory's radius of gyration.

$$T = \begin{bmatrix} \frac{1}{N} \sum_{j=1}^N (x_j - \langle x \rangle)^2 & \frac{1}{N} \sum_{j=1}^N (x_j - \langle x \rangle)(y_j - \langle y \rangle) \\ \frac{1}{N} \sum_{j=1}^N (x_j - \langle x \rangle)(y_j - \langle y \rangle) & \frac{1}{N} \sum_{j=1}^N (y_j - \langle y \rangle)^2 \end{bmatrix}$$

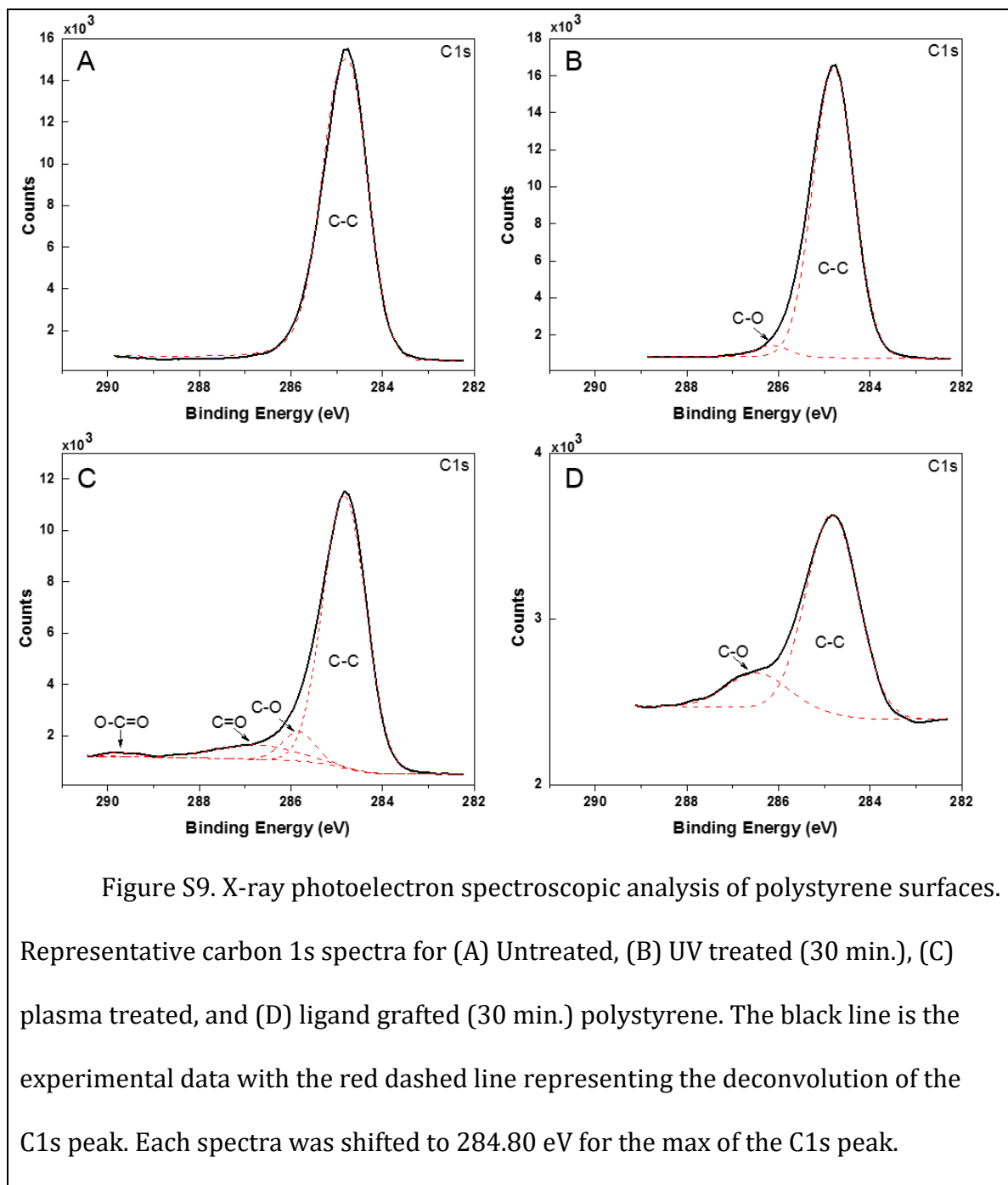
Equation 7.2 Radius of Gyration Tensor

In the tensor N corresponds to the number of steps taken over the entire trajectory and x and y are the locations of the molecule for that given step. In this study the trajectory's radius of gyration values reported are for the entire evolution for at least 800 lysozyme trajectories per condition reported.

Radius of Gyration Evolution Plots



X-ray photoelectron spectroscopy analyses



Elemental Composition analyses via XPS

Treatment	Time	Carbon %	Oxygen %
Polystyrene	0 min	99.6±0.1	0.4±0.1
UV	10 min	98.5±0.2	1.5±0.2
	20 min	98.6±0.7	1.4±0.7
	30 min	98.3±0.7	1.7±0.7
Plasma	1 sec	89±2	11±2
	3 sec	85.7±0.6	14.3±0.6
	5 sec	81±2	19±2
	7 sec	80.5±0.8	19.5±0.8
Ligand	5 min	61.9±0.7	38.1±0.7
	10 min	61.3±2	38.7±2
	20 min	60.5±0.5	39.5±0.5
	30 min	58.9±0.9	41.4±0.9

Table S1-Percent composition of carbon and oxygen at polystyrene interfaces for each treatment technique and corresponding treatment times. Values are the average of 3 separate areas on one sample with the error representing the standard deviation of the resulting measurements.

Contact angle measurements for plasma treated polystyrene

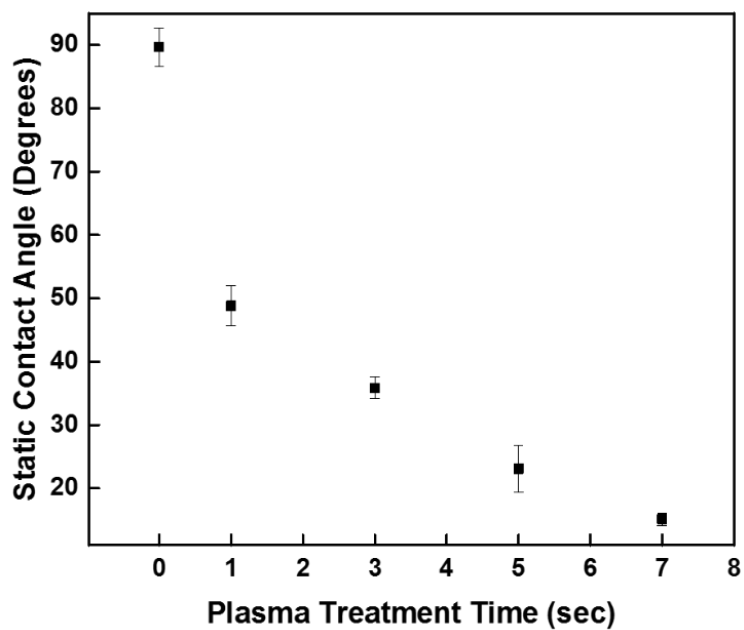


Figure S10. Static water contact angle for oxygen plasma treated polystyrene films. Each data point represents contact angle from 8 measurements from two different samples. The error bars represent the standard deviation of all the measurements for each condition.

Trajectory's radius of gyration results for plasma treated polystyrene

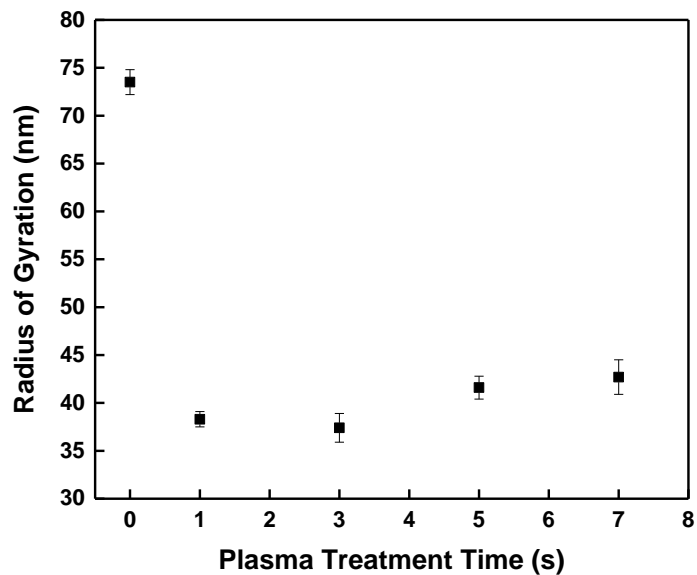


Figure S11. Trajectory's Radius of gyration values for lysozyme on oxygen plasma treated polystyrene films. Each data point is the average of at least 800 trajectories per condition represented with error bars indicating the standard error of the mean.

Salt dependence single molecule results

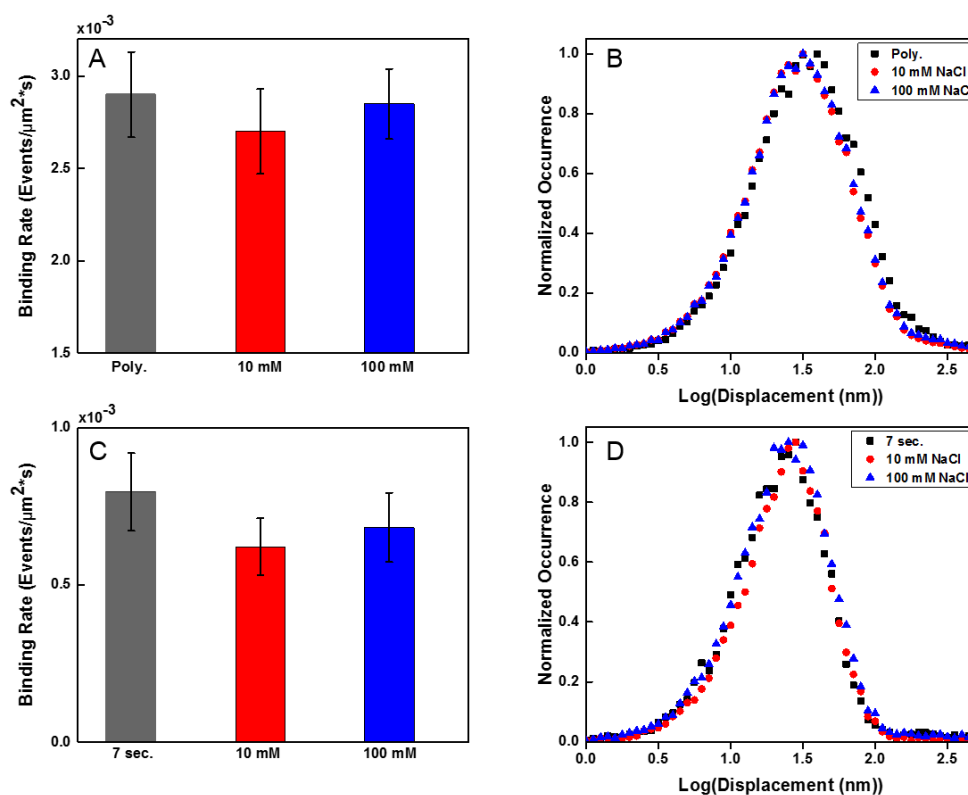


Figure S12. Adsorption and mobility of lysozyme under electrostatic screening.

Lysozyme binding rates (A) and single frame displacement distributions (B) at polystyrene in the presence of sodium chloride (10 mM and 100 mM). Lysozyme binding rates (C) and single frame displacement distributions (D) at 7 second plasma treated polystyrene (7 sec.) in the presence of sodium chloride (10 mM and 100 mM). Error bars in (A, C) represent the standard deviation of the mean from at least 1,600

adsorption events for each condition tested acquired from multiple samples. Each condition in (B, D) represents at least 800 events worth of data.

Ligand grafted chemical structure

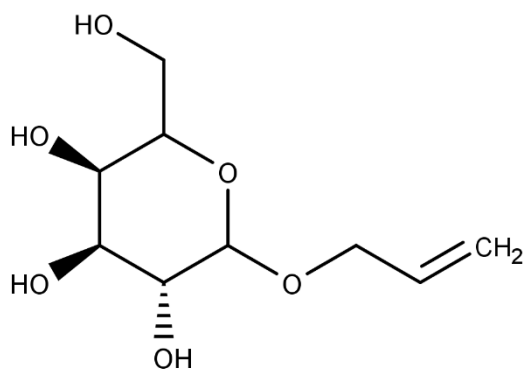
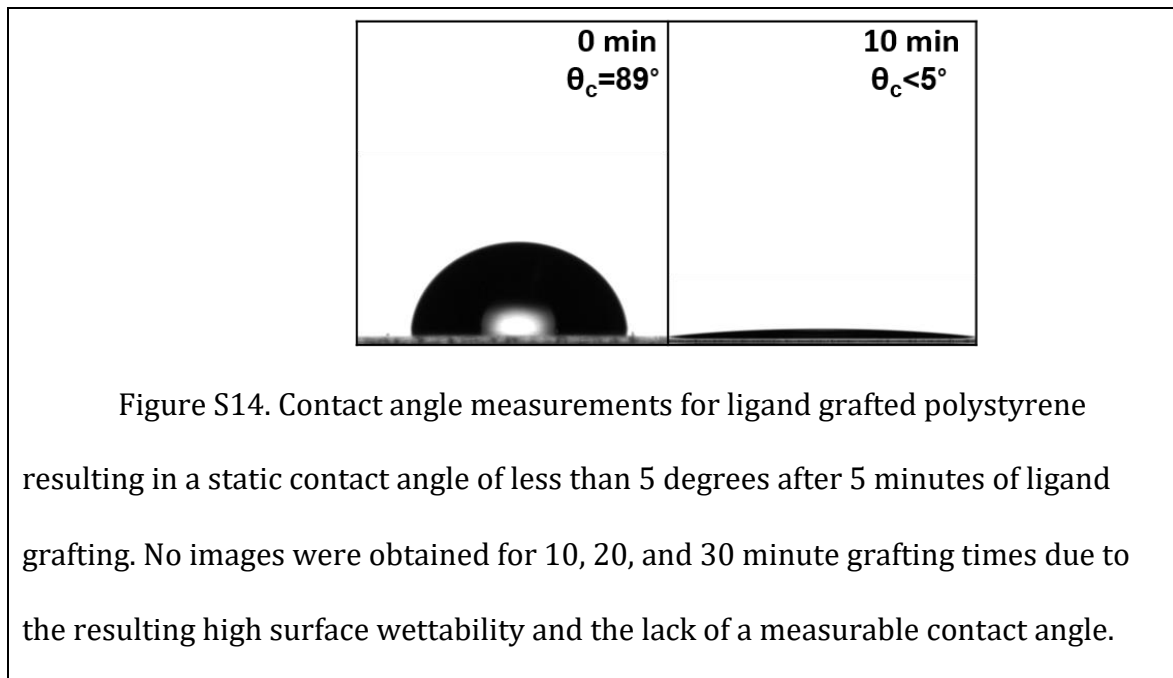


Figure S13. Structure for Allyl α -D-galactopyranoside ligand grafted to polystyrene surface. Generated using Marvin Sketch.

Contact angle measurements for ligand grafted polystyrene



Trajectory's radius of gyration results for ligand grafted polystyrene

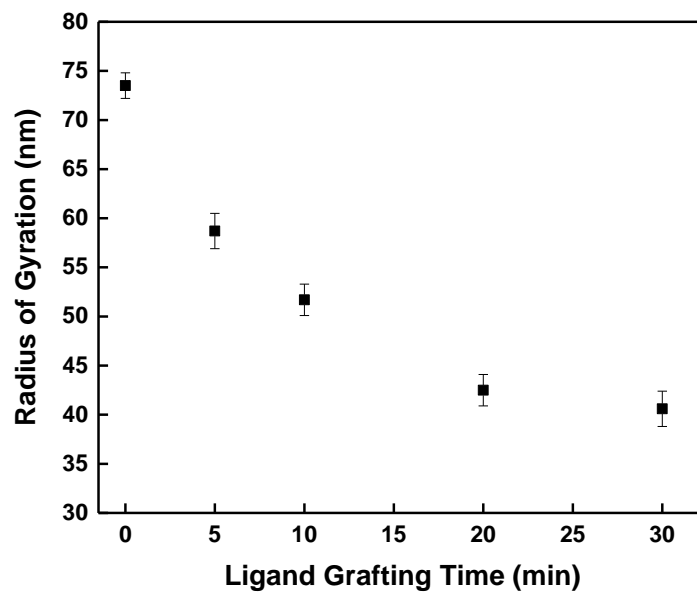
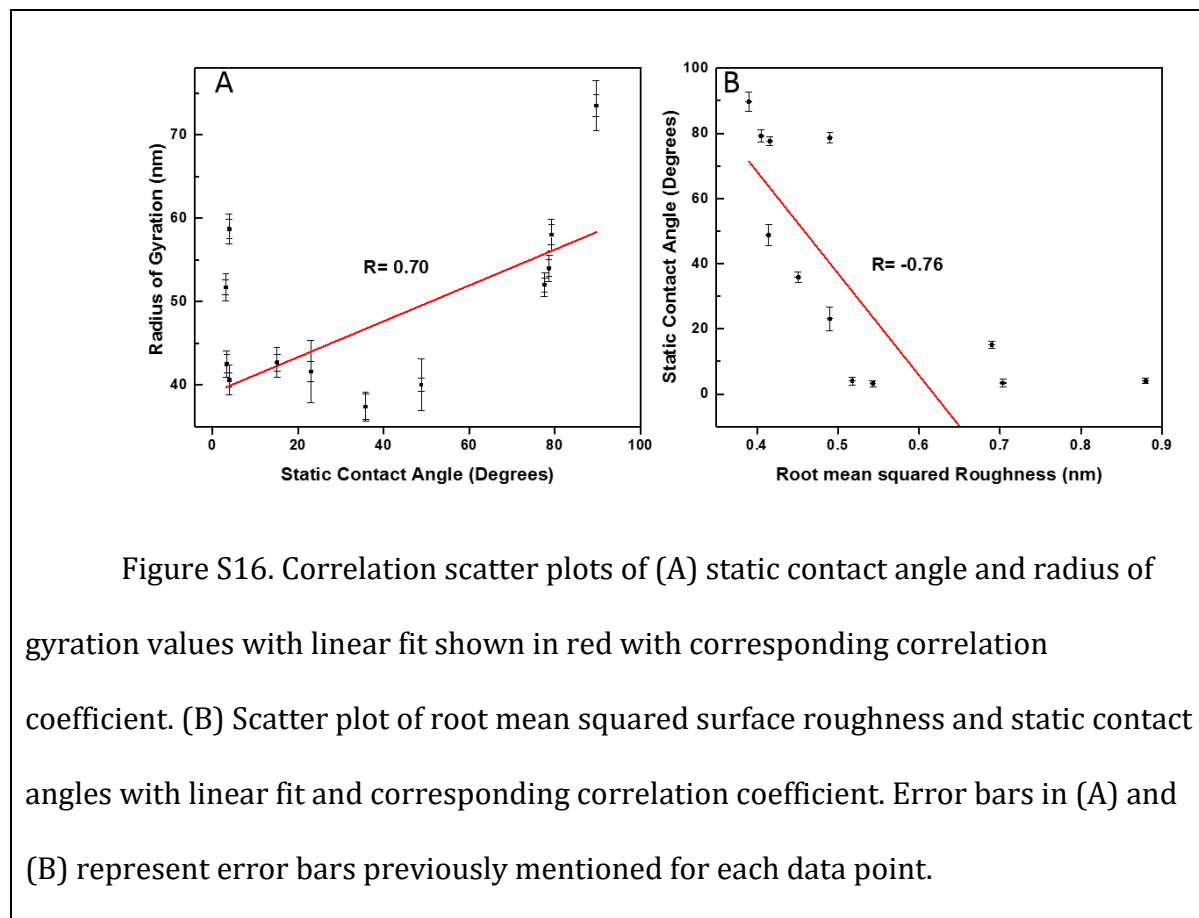


Figure S15. Trajectory's Radius of gyration values for ligand grafted polystyrene films. Each data point is the average of at least 800 trajectories per condition represented with error bars indicating the standard error of the mean.

Scatter Plots for Contact Angles vs Radius of Gyration and Root Mean squared Roughness



Atomic force microscopy surface roughness analyses

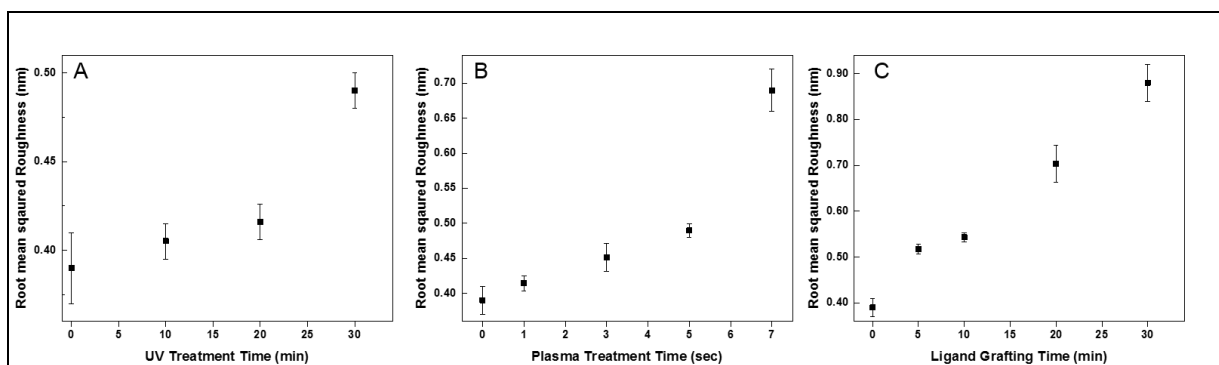


Figure S17. Surface roughness results from atomic force microscopy imaging.

Root mean squared surface roughness for (A) UV treated, (B) plasma treated, and (C) ligand grafted polystyrene interfaces. Error bars in A-C represent the standard deviation of 5 different analyzed areas of each respective treatment time.

7.2. Appendix to Chapter 3: A mechanistic examination of salting out in protein-polymer membrane interactions

Single Molecule Tracking Algorithm

Our previously reported single-molecule tracking algorithm, Troika, is utilized in order to produce single- molecule trajectories²⁸. Troika constructs single-molecule trajectories from movies in three sequential steps: increase signal-to-noise ratio (SNR) of each frame, localize emitters in each frame, connect localizations to construct trajectories. Firstly, the SNR is increased with a local averaging filter that performs a convolution with a three-by-three matrix of ones on each frame. Next, single-molecules are identified with a local background thresholding method. A molecule's peak intensity must be above the local noise plus three standard deviations of local noise in order to be identified. Identified molecules are then localized below the diffraction limit of light using a radial symmetry method. Lastly, trajectories are formed with a nearest neighbor method that connects frame to frame molecule localizations within a user defined search radius. Here the search radius is set to 8 pixels. This search radius along with filtering out trajectories that lasted only 1 frame allowed us to establish a 5% false trajectory linking based on frame shuffling analyses used previously^{242,277}. False trajectory linking was also minimized experimentally with a transferrin concentration of 100 pM.

Spatial Trajectory Filtering

Single-molecule trajectories are extracted using the previously described algorithm. The initial position (x_0, y_0) of each molecule is used as the center of a circular region with a radius of 22 nm. This distance is determined from our spatial resolution calculated from the immobile displacement distribution in single frame displacements shown later in Fig. S3. The displacement from (x_0, y_0) at each subsequent time point in a given trajectory is calculated and used to determine if the molecule exits the circular region over the course of the entire trajectory. Molecules that remain within the region are classified as undergoing single-site adsorption-desorption, while molecules that exit the region are classified as exhibiting a CTRW.

Ensemble Circular Dichroism Measurements

Protein secondary structure data is collected using a Jasco J-810 spectropolarimeter. All measurements are acquired from unlabeled 70 μM Transferrin (Sigma) solutions in 10 mM HEPES buffer from 200 to 250 nm with a scan speed of 20 nm/min in a 0.01 mm quartz cuvette. Buffer concentration is held constant with varied salt concentrations. Nylon beads, synthesis described in the main text, are dispersed at a constant concentration in solution for all nylon conditions. Data is obtained in millidegrees and is averaged over 10 accumulations with a data pitch of 0.1 nm. Millidegrees is converted to molar residue ellipticity $[\theta]$ using Equation 7.3:

$$[\theta] = \frac{\theta}{l \times N \times c \times 10}$$

Equation 7.3 Molar Residue Ellipticity conversion

where θ is ellipticity in degrees reported by the instrument, l is the pathlength of the cuvette in cm, N is the number of residues in the protein, and c is protein concentration (g/cm^3).

X-ray Photoelectron Spectroscopy

X-ray photoelectron spectroscopy (XPS) measurements of nylon 6,6 membrane filters and nylon 6,6 films are performed using PHI Quantera XPS spectrometer. Excitation source Al K α X-rays (1486.7 eV) is operated at 50 W, 15 kV and focused onto a 200 μ m diameter spot. Survey scans were collected at energies ranging from 0 to 1100 eV with a pass energy of 140 eV for each sample. High-resolution spectra of Carbon 1s, Oxygen 1s, and Nitrogen 1s are collected in 0.1 eV steps with a pass energy of 26 eV.

Surface charge and protein hydrodynamic radius measurements

A Malvern zetasizer (Zen 3600 Nanoseries) is utilized to measure the zeta potential of nylon 6,6 and hydrodynamic radius of transferrin. Granules of nylon 6,6 dispersed in water at pH 7.2 are measured with 50 repeats in Malvern cuvettes (DTS1070) and the average and variance were calculated. Hydrodynamic radius measurements of unlabeled transferrin are performed in 10 mM HEPES buffer. All measurements are taken at 25 °C after 2 minutes equilibration in the instrument.

Nylon Thickness vs. Polymer Solution Concentration

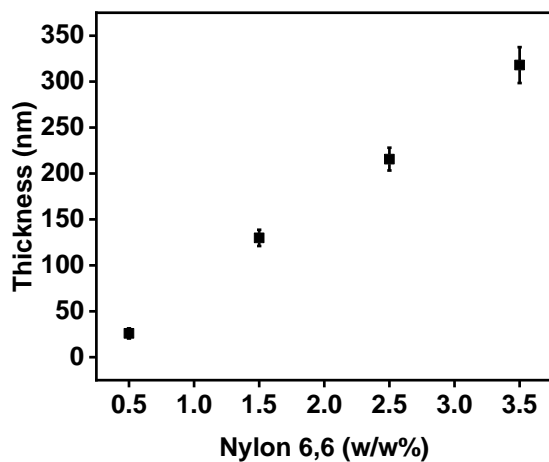
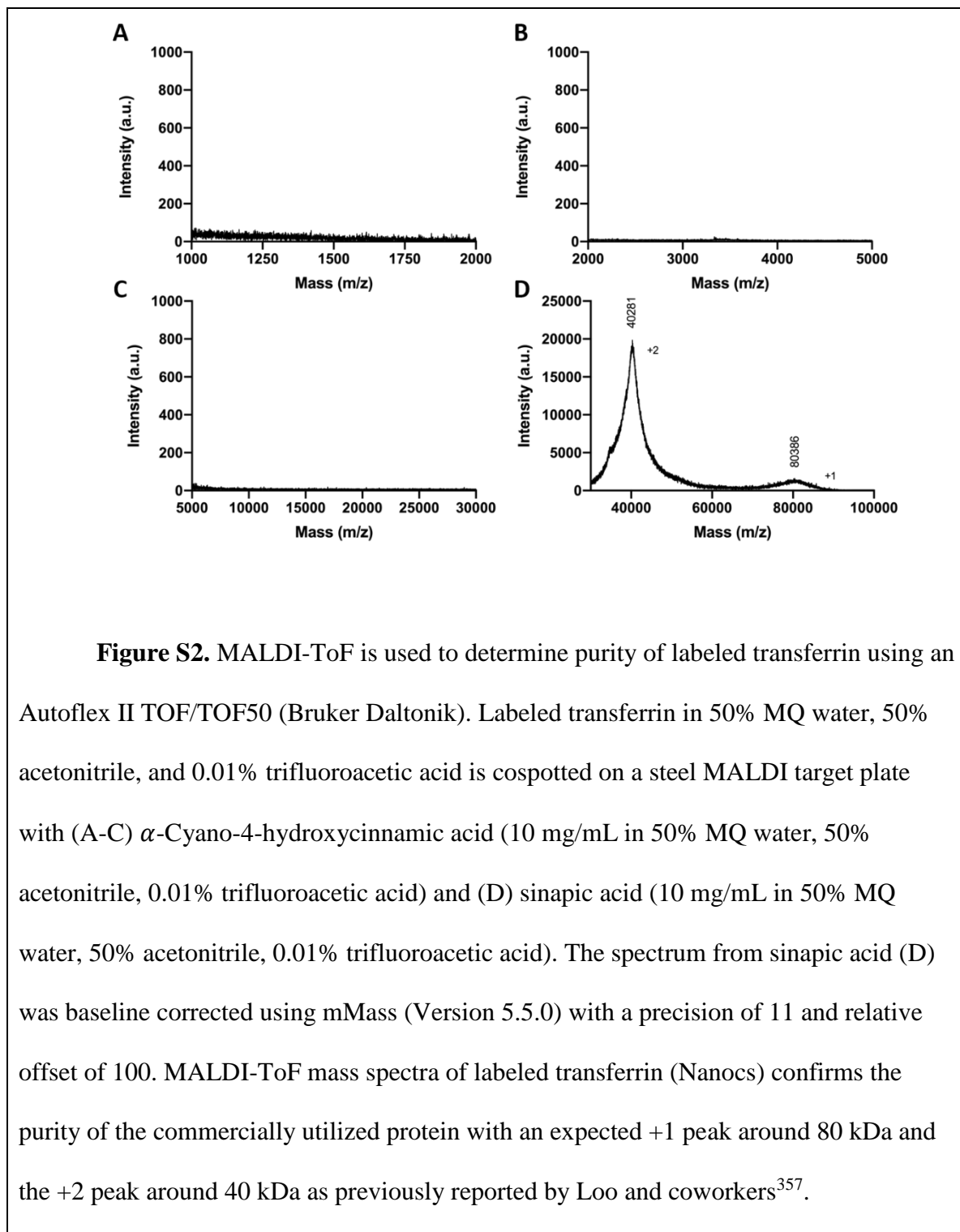
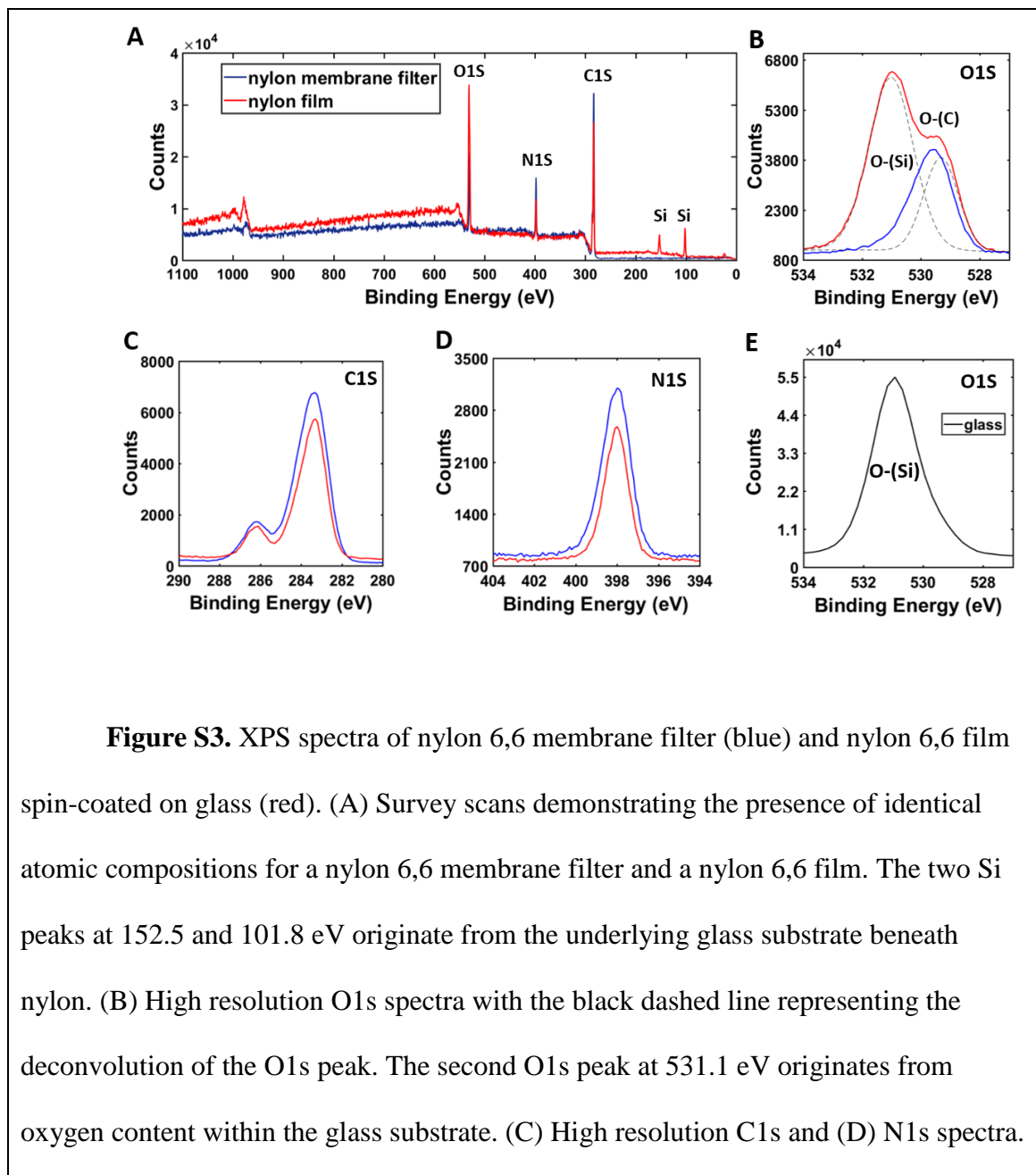


Figure S1. Nylon film thickness vs. nylon solution concentration in weight/weight percent. Film thicknesses are determined using ellipsometry as described in the main text. Error bars are standard deviation of measurements from 5 different areas on a sample. For single-molecule experiments the 1.5 wt/wt% solution is used resulting in a 129.0 ± 0.3 nm thick film.

MALDI-ToF Mass Spectrometry of Labeled Transferrin



X-ray Photoelectron Spectroscopy characterization of nylon membrane and film



(E) High resolution O1s spectra of bare glass, confirming the origin of the second peak at 531.1 eV for O1s spectra shown in (B). XPS analyses confirm the same chemical identity of membranes and films used in ensemble FPLC and single-molecule experiments, respectively.

Quantifying Continuous Time Random Walk Motion

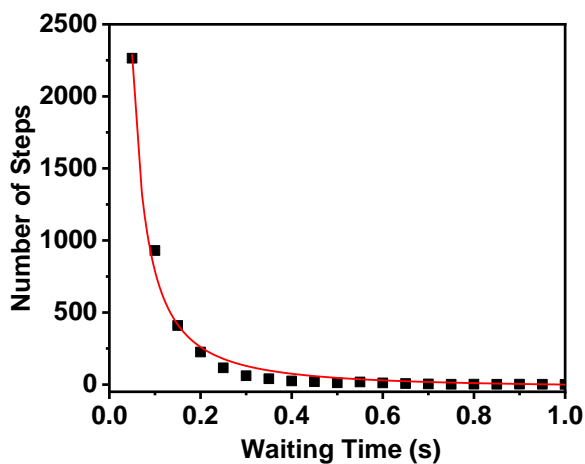


Figure S4. Waiting time analysis for CTRW dynamics. Hops are defined as any frame to frame transferrin displacements that are over 22 nm, a distance determined by our localization precision. Similar spatial filters have been previously applied by others for defining a hop⁸⁰. Roughly 4,000 hops are analyzed and fit to a power law function ($f(x) = ax^{-b}$) as described by others⁸⁰. The fitting results of waiting time indicate CTRW motion is present for transferrin at nylon.

Single frame displacement distributions and Gibbs Sampling

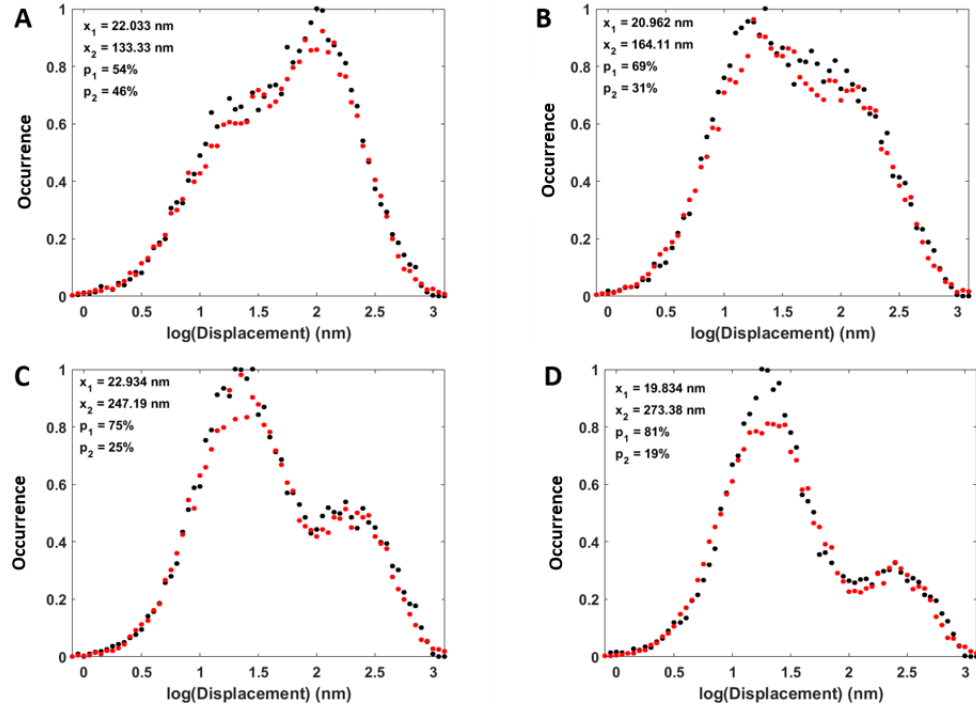


Figure S5. Single frame displacement distribution and sampling results from

previously reported Markov Chain Monte Carlo algorithm²⁷⁷. (A-B) Representative single frame displacement distributions (black) and sampling results (red).

Distributions shown in A,B,C, and D correspond to 0, 10, 500, and 1000 mM respectively. x_1 and x_2 values represent the mean of each distribution with the corresponding prevalence, p_1 and p_2 . Sampling results show the MCMC algorithms ability to capture the data in distributions accurately.

Single frame displacement reversibility

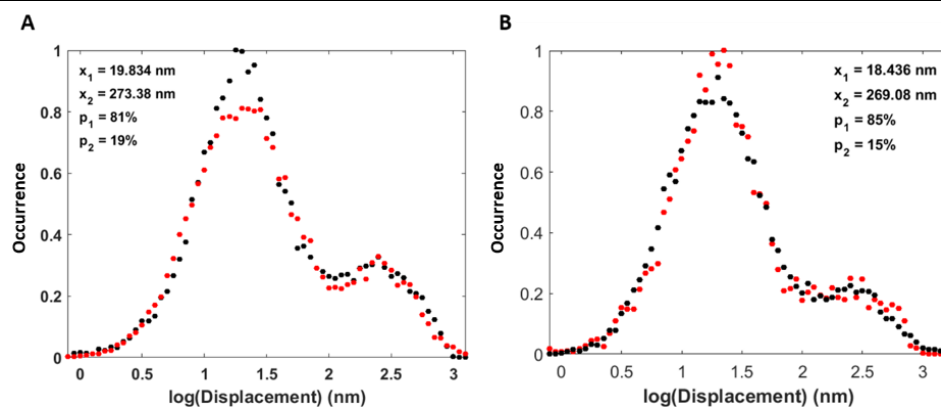


Figure S6. Reversibility of transferrin dynamics. (A) Single frame

displacement distributions (black) and sampling results (red) from data captured within 2 mins of high salt exposure (A, 1000 mM) and the resulting distribution (B) 11 hours after no salt exposure followed by high salt exposure again. This highlights the reversibility of the transferrin transport dynamics at nylon.

Transferrin stability in high salt conditions

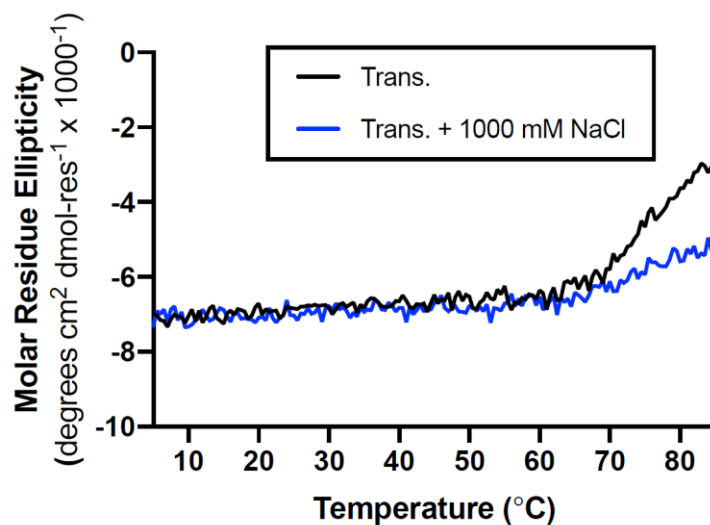


Figure S7. Transferrin stability in the presence and absence of salt is evaluated using a Jasco J-810 spectropolarimeter equipped with a Peltier temperature controller. Ellipticity was monitored at 222 nm as temperature was increased from 5 °C to 85 °C at a rate of 10 °C per hour for 3.5 μM Transferrin (black) and 3.5 μM Transferrin with 1000 mM salt (blue) both prepared in 10 mM HEPES buffer. Data pitch is 0.5 °C for both traces shown here. Data was obtained in millidegrees and converted to molar residue ellipticity. 222 nm is the chosen wavelength to monitor ellipticity based on previous studies of transferrin stability³⁵⁸. Results show transferrin unfolds less in the presence of salt and is therefore more stable at higher temperatures.

Circular Dichroism indicates unfolding is a surface induced phenomena

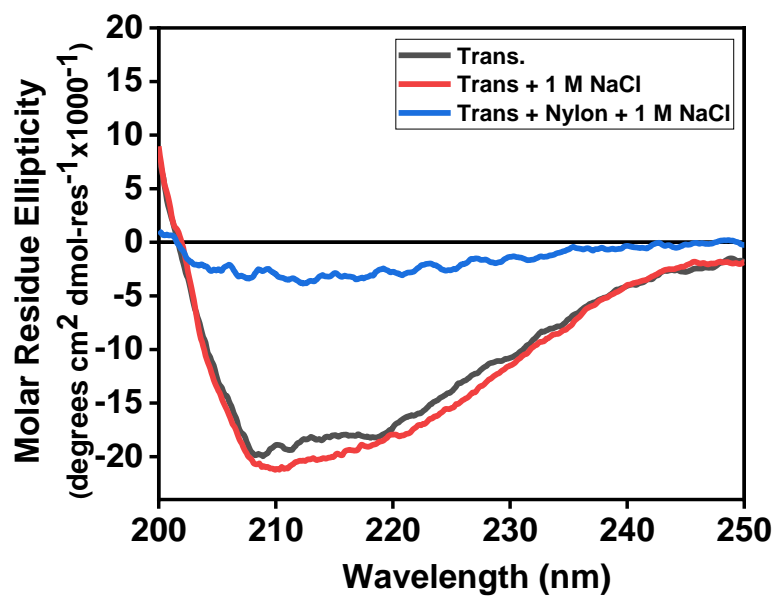
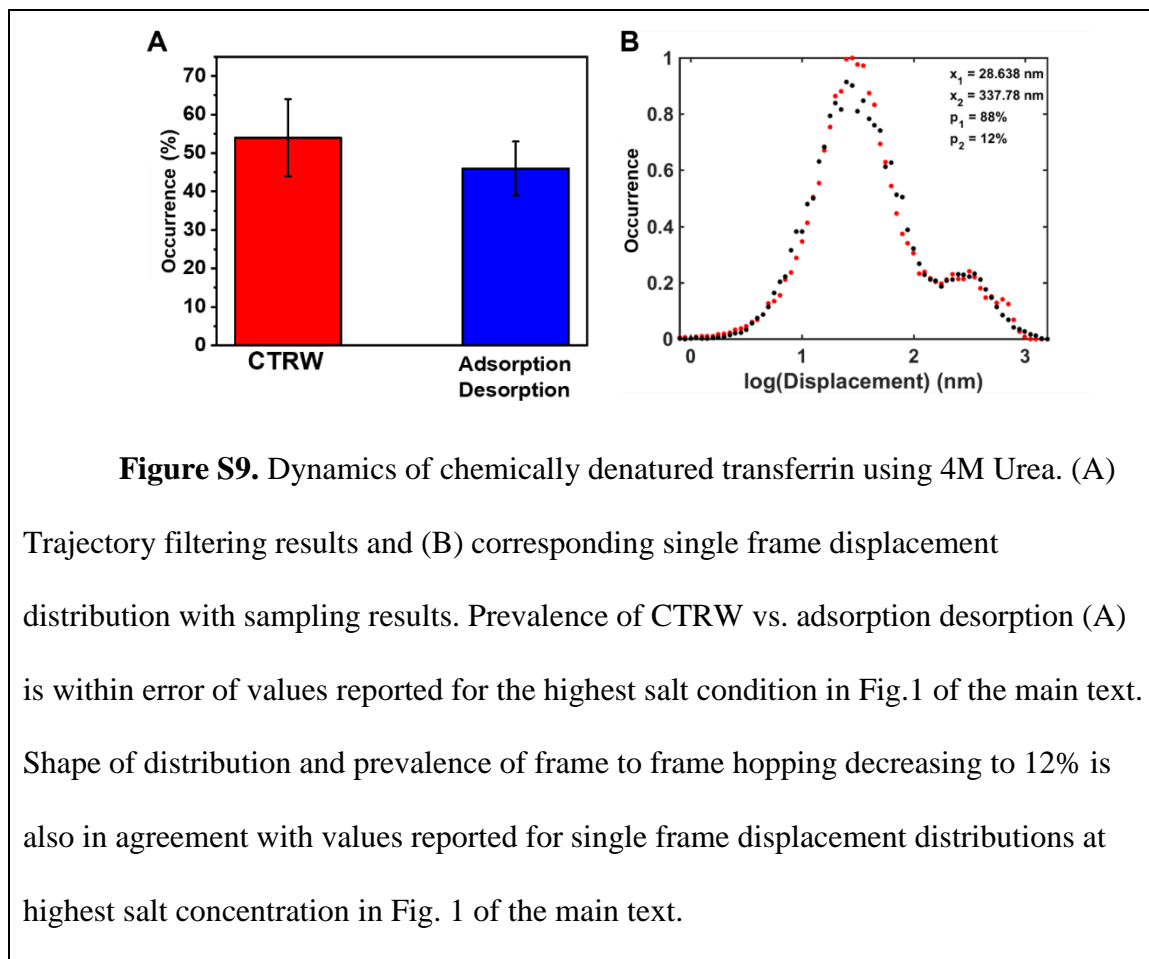


Figure S8. Circular dichroism results with transferrin and salt alone.

Unfolding is only observed in the presence of Nylon.

Chemically Unfolded Transferrin Transport Dynamics



Surface Residence time CDF's of Urea treated Transferrin

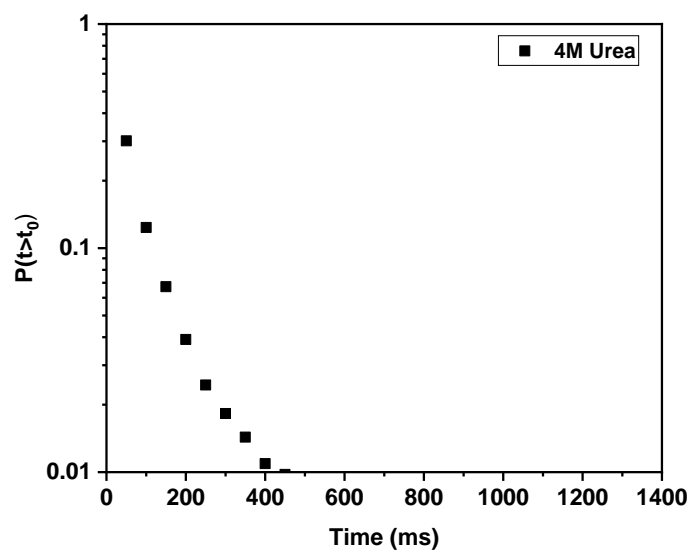


Figure S10. Surface residence time CDF plot of transferrin exposed to 4M Urea. Chemically denatured transferrin shows fast desorption kinetics in comparison to no salt conditions in Fig. 2B.

Waiting time analyses at varied ionic strength

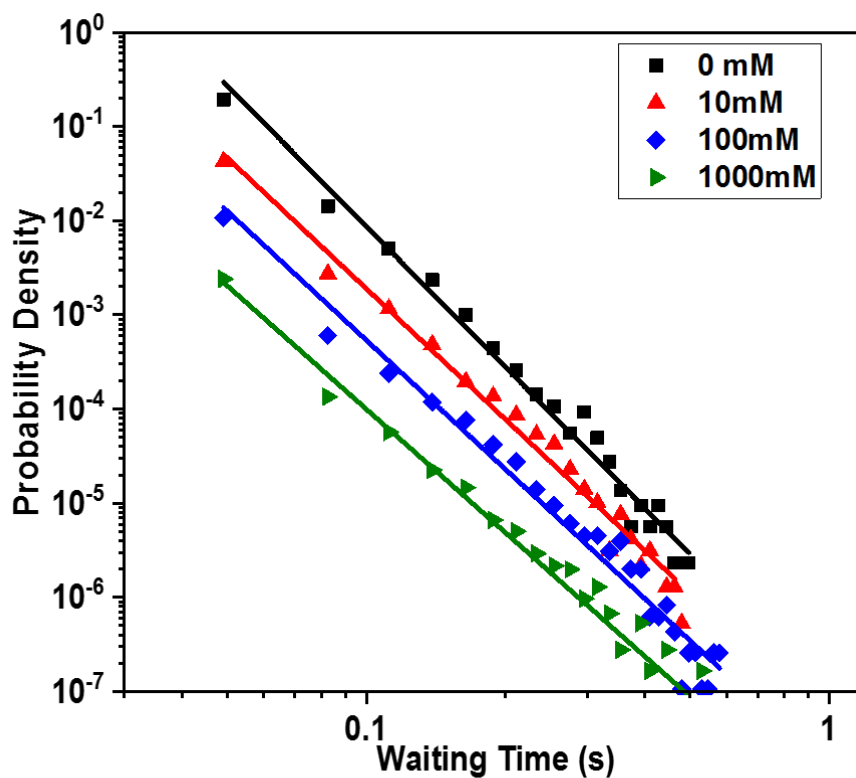


Figure S11. Waiting time distributions shown for experiments with increasing ionic strength. Waiting times are defined as the time transferrin resides at a site, which is determined by a spatial filter of 22 nm, previously described to determine the adsorption to a new site. Solid lines show fits to a power law function ($f(x) = ax^{-b}$) as described by others with slopes of -2.85, -2.71, -2.35, and -2.25 for 0 mM, 10 mM, 100 mM, and 1000 mM respectively. Fit results show waiting time distributions become broader as salt is increased, indicating longer waiting times occur at higher salt

concentrations. Data is offset on y-axis and plotted on log-log plot to show trends more clearly, similar to Schwartz and Kaar⁸⁰.

Circular Dichroism Spectroscopy of Unlabeled vs. Labeled Transferrin

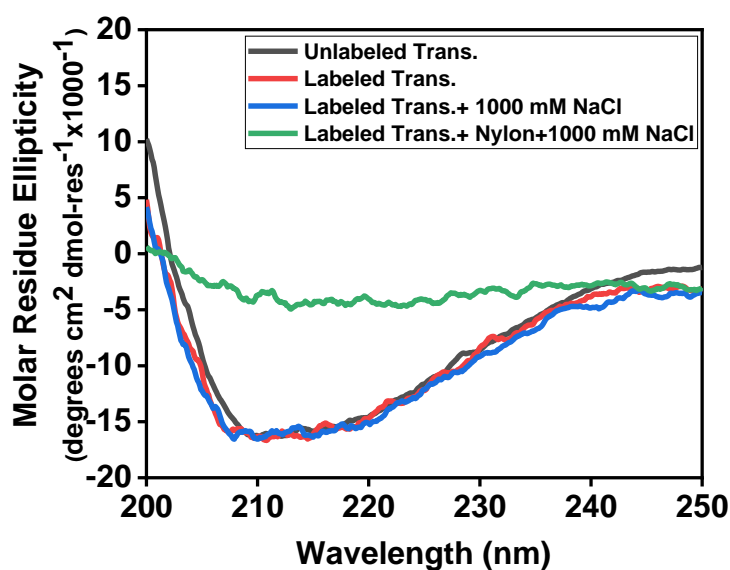


Figure S12. Circular dichroism of unlabeled transferrin compared to labeled transferrin. Results indicate the addition of Rhodamine B dyes to transferrin do not disrupt the overall structure of the protein. Moreover, unfolding is observed only in the presence of nylon and not with salt alone aligning with both results observed with unlabeled transferrin in Fig. S8.

Concentration dependent FPLC separations

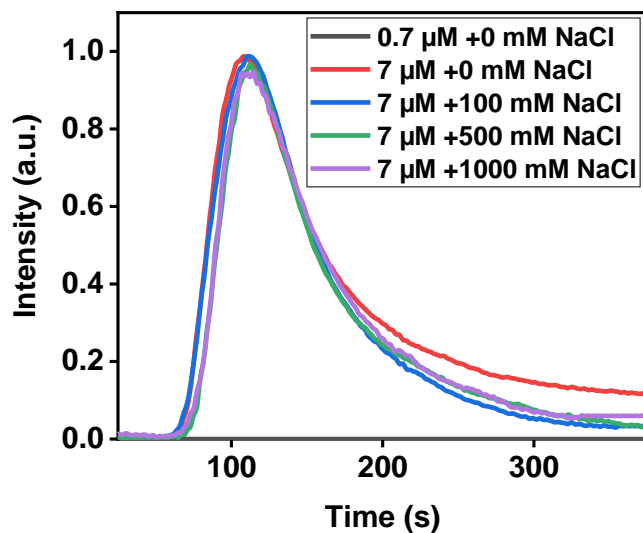


Figure S13. FPLC results of transferrin separations at 0.7 μM and 7 μM . The respective FWHM values are: 74, 71, 63, and 68 for increasing salt concentrations shown. No signal is detected with a 0.7 μM injection, indicating separations are being performed at the lowest detectable concentrations. Results indicate overcrowding effects are not the cause of peak narrowing or line shape.

Circular Dichroism of Eluted Transferrin

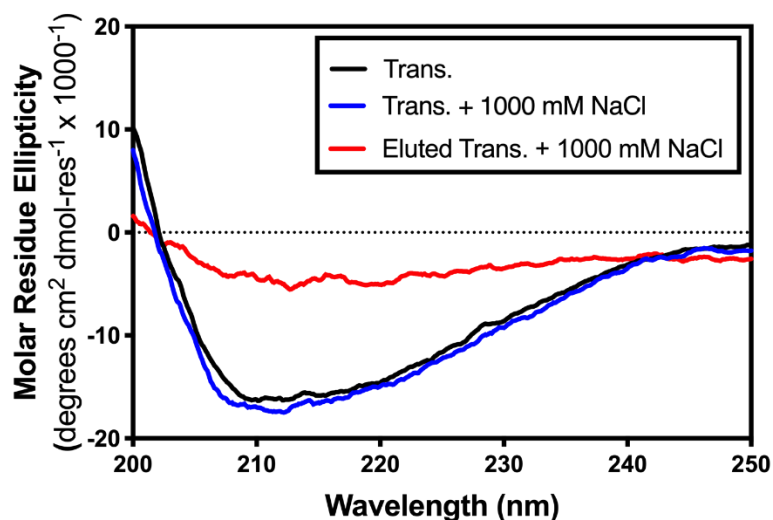


Figure S14. Circular dichroism measurement of eluted transferrin fraction from separation at 1000 mM NaCl in comparison to native transferrin structure with and without salt. Concentration of eluted fraction was measured using UV-Vis to correct for concentration differences between the two conditions shown. Results show eluted transferrin at high salt concentration is unfolded. Unfolding is a surface induced effect not induced by salt alone (blue trace), confirming transferrin adsorbs to the nylon membranes during FPLC experiments.

Table S1. Calculated surface transferrin diffusion coefficients compared to calculated in solution diffusion coefficient

Salt concent ration [mM]	0	1	10	50	100	500	1000
D surface (m ² s ⁻¹)	(2.8± 0.5) x 10 ⁻¹²	(3.1± 0.1) x 10 ⁻¹²	(3.1± 0.1) x 10 ⁻¹²	(2.7± 0.1) x 10 ⁻¹²	(3.0± 0.1) x 10 ⁻¹²	(3.0± 0.1) x 10 ⁻¹²	(3.0± 0.1) x 10 ⁻¹²
D solution (m ² s ⁻¹)	(3.3± 0.1) x 10 ⁻¹¹	-	-	-	-	-	-

Table S1. Calculated surface diffusion coefficients from at least 2,500 trajectories at nylon for each salt condition. Diffusion coefficients are calculated using our previously reported maximum likelihood estimation algorithm applied to trajectories produced from our tracking algorithm²⁹. Surface diffusion values of transferrin are compared to the calculated value using the Stokes-Einstein relation ($D_{solution} = \frac{kT}{6\pi\eta R_H}$) with the measured hydrodynamic radius ($R_H = 6.01 \pm 0.12$ nm) of transferrin

from dynamic light scattering (Malvern ZEN 3600). The calculated diffusion coefficient of transferrin in solution matches well with the value reported by others³⁵⁹. Surface diffusion coefficients do not show a dependence on salt concentration and the in solution diffusion coefficient is faster than that quantified at the surface of nylon, allowing us to image the surface dynamics while suppressing the in solution diffusion of transferrin.

Table S2. Desorption Rate Constants of CTRW vs. Single-site adsorption-desorption

Salt Concentration [mM]	CTRW (s ⁻¹)	Adsorption- Desorption (s ⁻¹)	k _{des} for A ₁ from Fig 2D (s ⁻¹)
0 mM	$(3.6 \pm 0.5) \times 10^{-3}$	$(5.8 \pm 0.5) \times 10^{-3}$	$(9 \pm 1) \times 10^{-3}$
1000 mM	$(5.9 \pm 0.5) \times 10^{-3}$	$(8.0 \pm 0.5) \times 10^{-3}$	$(1.8 \pm 0.1) \times 10^{-2}$

Table S2. Desorption rate constants of transferrin molecules undergoing CTRW and single-site adsorption-desorption. Desorption rates were determined using the inverse of average residence time ($\frac{1}{\langle \tau_{on} \rangle} = k_{des}$)^{53,360-361} for trajectories classified as CTRW or adsorption-desorption as described above in Fig. 1 of the main text. Desorption rate constant of fast (A₁) population from surface residence time CDF plots (Fig. 2) shown in final column for comparison. Error is the standard deviation of at least 4,000 trajectories for the CTRW and adsorption-desorption column. Error in final column is the fitting error.

7.3. Appendix to Chapter 4: Polymer free volume effects on protein dynamics at polystyrene revealed by single-molecule spectroscopy

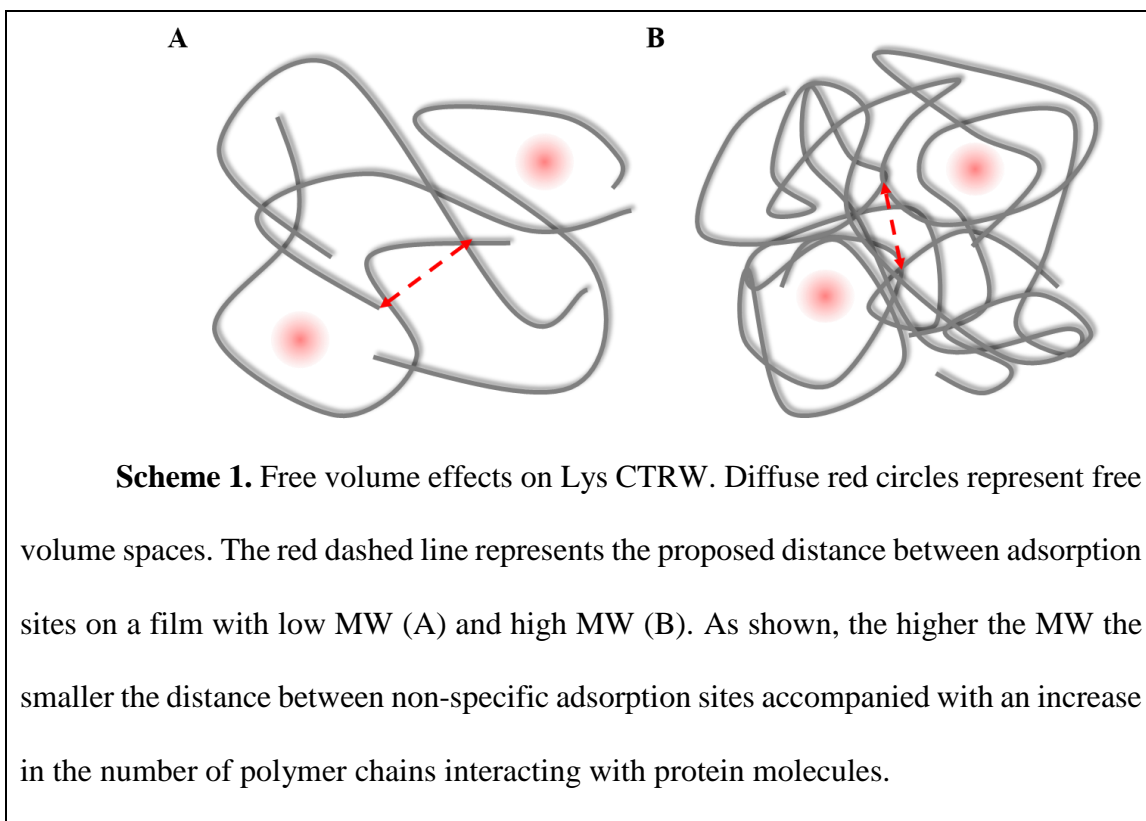
Polystyrene film thicknesses and refractive indices

Molecular Weight (g/mol) or Condition	Film Thickness (nm)	Refractive Index (n) at 632 nm
3k	43.8±0.2	1.534±0.001
36k	43.4±0.2	1.569±0.001
1500k	74.20±0.01	1.572±0.002
Cyclohexane (MW=36k)	100.3 ±0.2	1.593 ±0.003
Annealed (MW=36k)	40.8 ±0.2	1.63 ±0.01

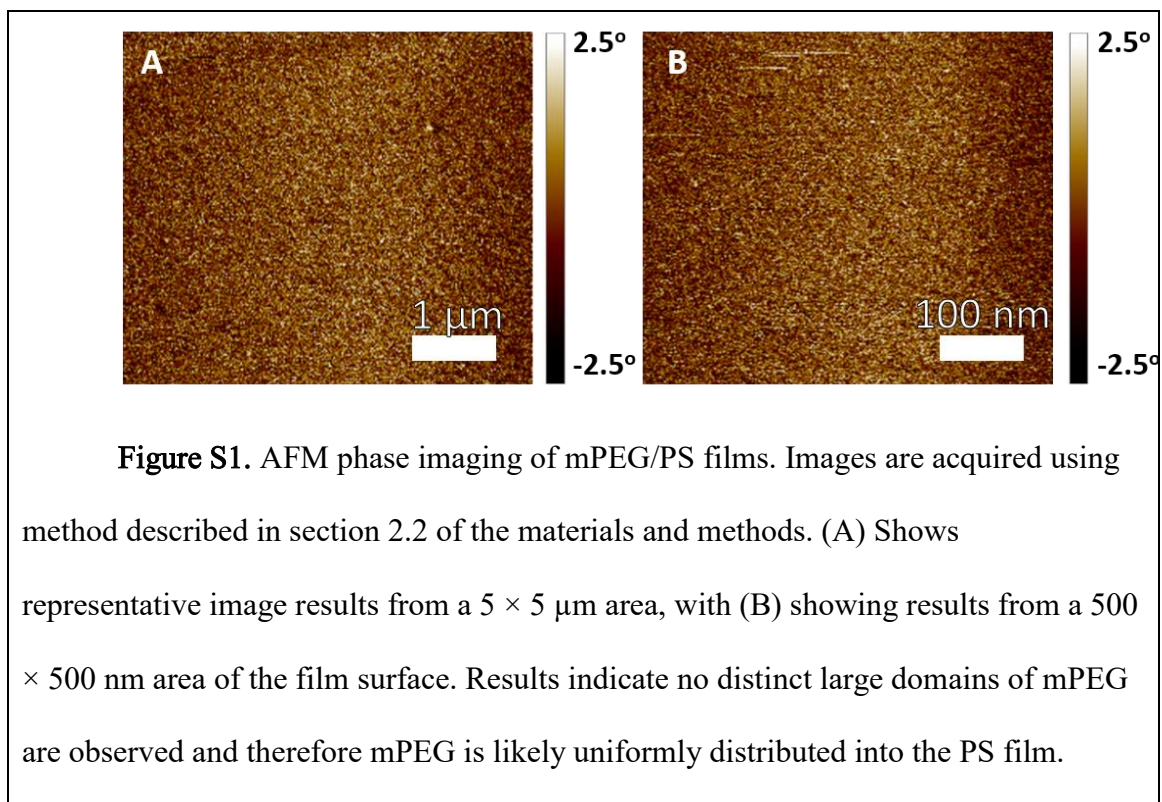
Table S1. Film thicknesses and refractive indices for various PS film conditions. Values acquired using ellipsometry as described in the main text (Materials and Methods Section 2.2). Results indicate a slight increase in thickness as molecular weight is

increased and increasing refractive index as MW is increased. Poor solvent quality and annealing produce the highest refractive indices.

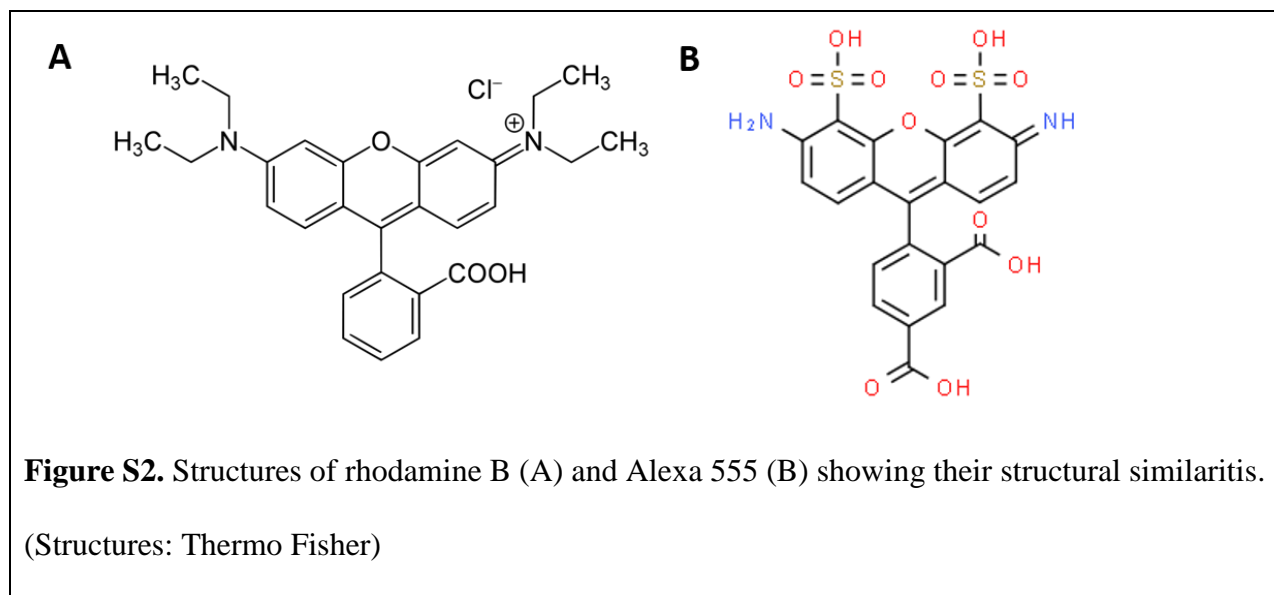
Lys. CTRW vs. chain density interaction scheme



AFM phase imaging of mPEG/PS films



Dye structures



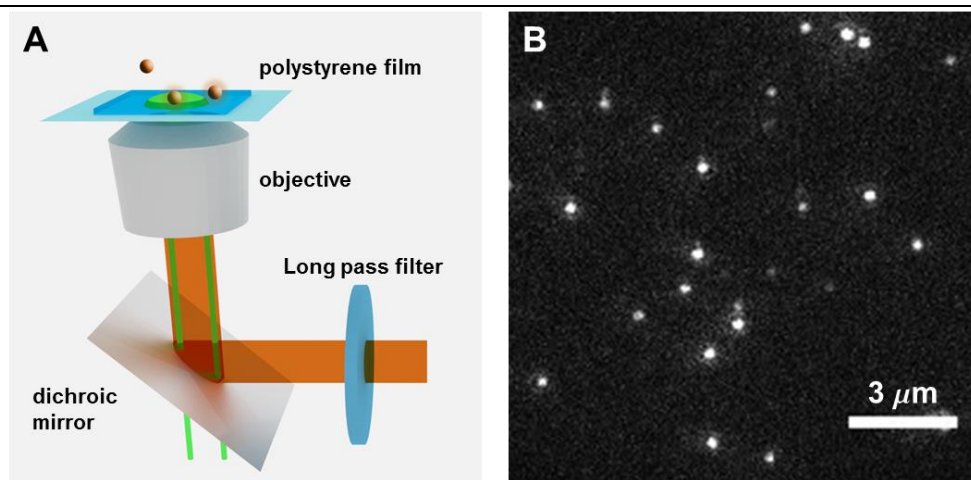
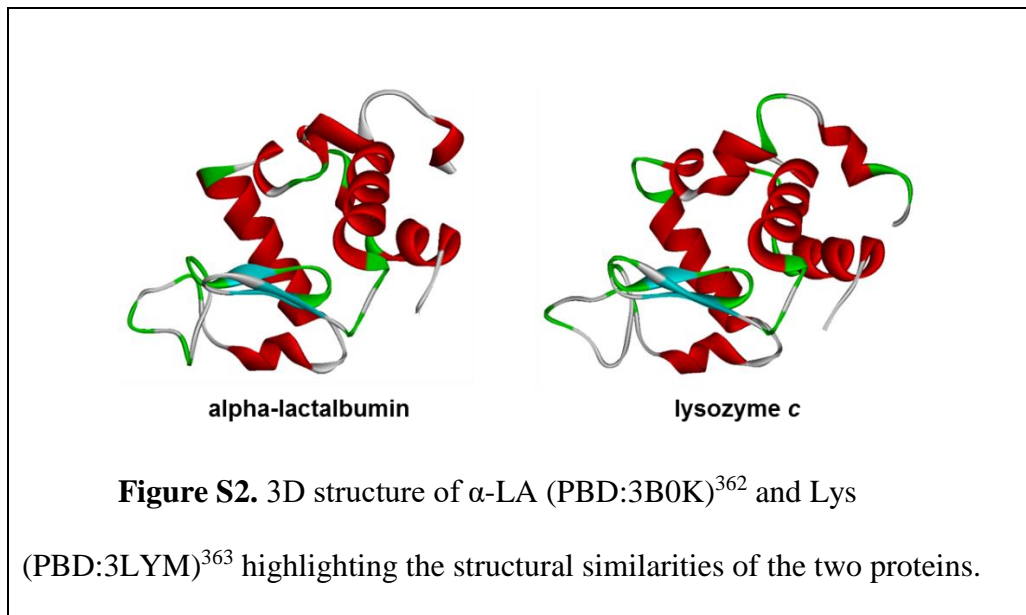
Single molecule TIRF Setup and Representative α -LA Image

Figure S1. (A) Experimental design based on a total internal reflection fluorescence (TIRF) microscope depicting the evanescent field propagating from the film-aqueous interface. Spheres depict the adsorption-desorption of α -LA molecules. (B) One representative frame captured on an EMCCD within the excited area in (A). Each discrete bright spot is a single Alexa 555 labeled α -LA molecule.

Alpha-lactalbumin and lysozyme structures



Lys residence time with varied dye labels

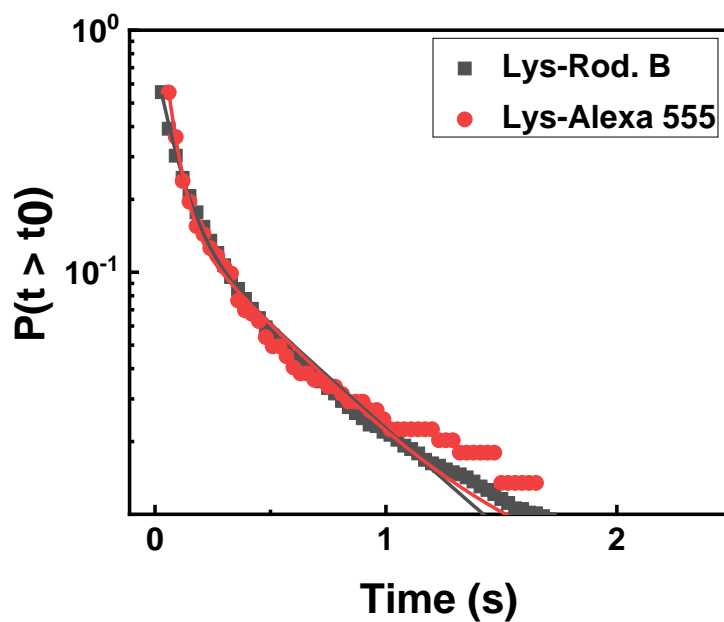


Figure. S5 Lys surface residence times with Alexa 555 and Rhodamine B labels.

Lys labeled with Alexa 555 (Nanocs) was diluted to same concentration as reported in Lys. Rhodamine B condition (35 nM, grey). Solid lines show fits to Equation 1. Results indicate that identity of the fluorescent label does not alter binding strength of Lys.

α -LA Surface Residence Time Fit Results

Molecular Weight	A ₁ (%)	k ₁ (s ⁻¹)	A ₂ (%)	k ₂ (s ⁻¹)
3k	46.4±0.5	8.53±0.09	7.03±0.09	0.69±0.01
36k	44.5±0.5	7.26±0.09	9.9±0.1	0.63±0.01
1500k	48.6±0.5	6.97±0.07	10.6±0.1	0.70±0.01

Table S1. Fit results from residence time distributions of α -LA from distributions in Fig. 1D using $P(t) = A_1 e^{-k_1 t} + A_2 e^{-k_2 t}$ (Equation 4.2).²⁴⁶ As molecular weight increases the observed desorption rate constant for the A1 population is decreasing indicating the overall desorption occurs more slowly on higher molecular weight PS.

Waiting time analyses and power law fitting results for lysozyme

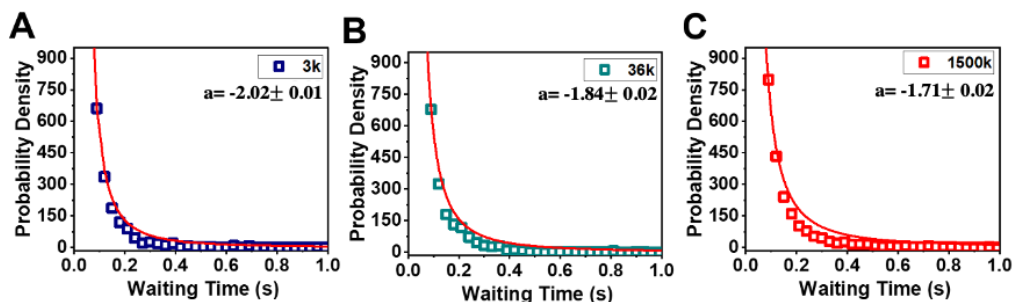


Figure S3. Waiting time distributions for Lys at MW varied PS. Lys

displacements greater than 22 nm indicate a desorption event, this distance is determined by our localization precision (Fig. 1 A-B). Defining a hop with a spatial filter has been previously applied by others.⁸⁰ Roughly 2,000 hops are analyzed and fit to a power law function ($f(x) = bx^{-a}$) as described by others.⁸⁰ Fits (red) indicate the presence of CTRW motion for Lys at PS. The increase in the waiting exponent (a) indicates that longer waiting times are observed as MW is increased.

Lys Surface Residence Time Fit Results at MW Varied PS

Molecular Weight	A ₁ (%)	k ₁ (s ⁻¹)	A ₂ (%)	k ₂ (s ⁻¹)
3k	56.7±0.2	14.6±0.1	16.1±0.1	1.83±0.02
36k	54.7±0.2	12.9±0.1	16.0±0.1	1.56±0.01
1500k	57.5±0.3	13.1±0.1	16.3±0.2	1.98±0.02

Table S2. Fit results from residence time distributions of Lys. from data in Fig.

2D using $P(t) = A_1 e^{-k_1 t} + A_2 e^{-k_2 t}$ (Equation 4.2).²⁴⁶ No major change in desorption rate constants are observed as MW is varied.

Lys Surface Residence Time Fit Results at Annealed PS

Treatment	A ₁ (%)	k ₁ (s ⁻¹)	A ₂ (%)	k ₂ (s ⁻¹)
As-prepared	54.7±0.2	12.9±0.1	16.0±0.1	1.56±0.01
Annealed	52.5±0.3	10.03±0.09	10.4±0.1	1.54±0.01

Table S3. Fit results from residence time distributions of Lys. from data in Fig.

3B using $P(t) = A_1 e^{-k_1 t} + A_2 e^{-k_2 t}$ (Equation 4.2).²⁴⁶ Results indicate that on the annealed PS that desorption is occurring more slowly for the A₁ population.

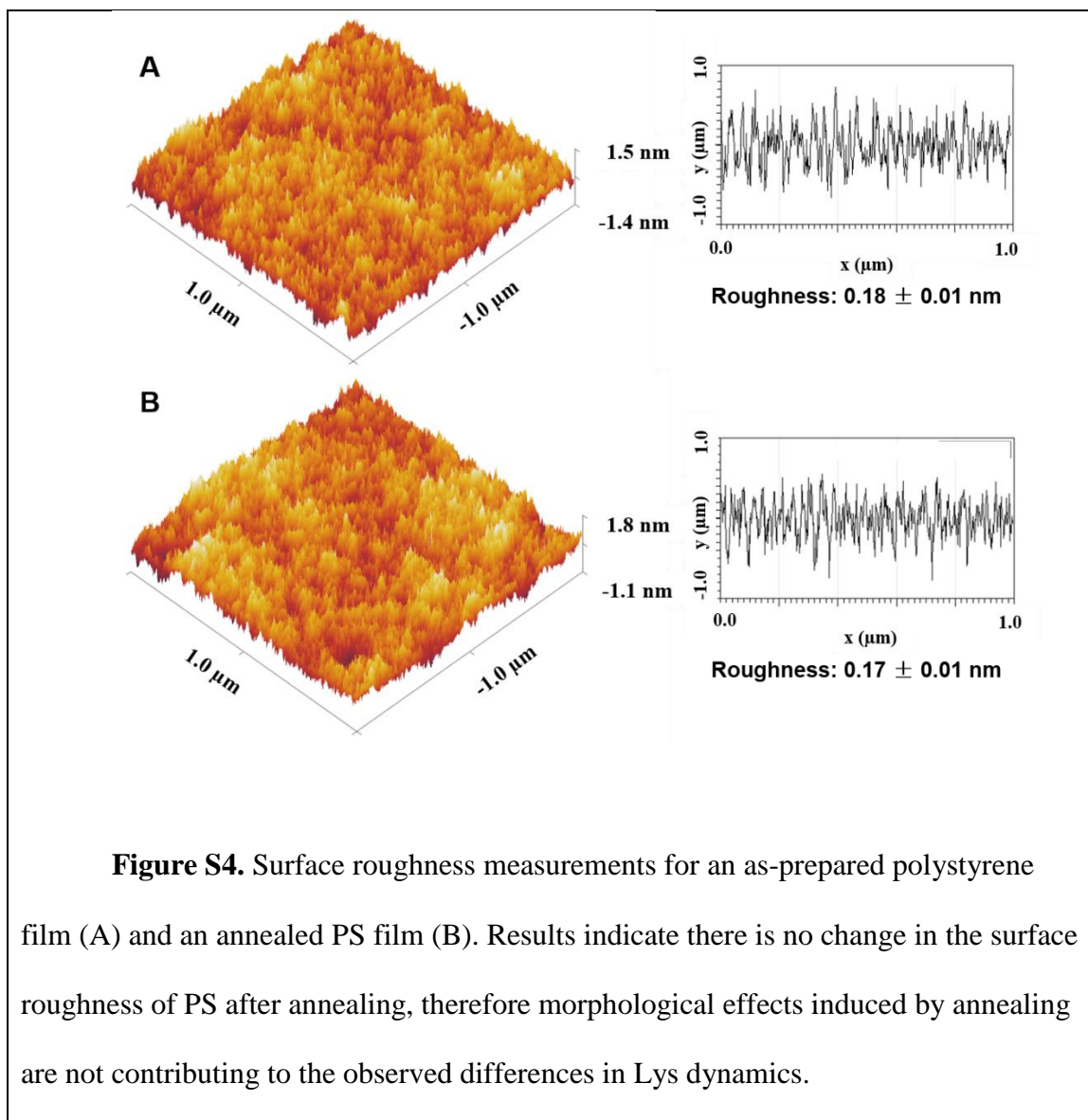
Lys Surface Residence Time Fit Results at Solvent varied PS

Solvent	A ₁ (%)	k ₁ (s ⁻¹)	A ₂ (%)	k ₂ (s ⁻¹)
Toluene	54.7±0.2	12.9±0.1	16.0±0.1	1.56±0.01
Cyclohexane	59.3±0.3	12.0±0.1	11.7±0.1	1.01±0.01

Table S4. Fit results from residence time distributions of Lys. from data in Fig.

3D using $P(t) = A_1 e^{-k_1 t} + A_2 e^{-k_2 t}$ (Equation 4.2).²⁴⁶ Results indicate that on the cyclohexane PS that desorption is occurring more slowly overall.

Atomic Force Microscopy of PS and Annealed PS Surface



Single frame displacement distributions under salt conditions

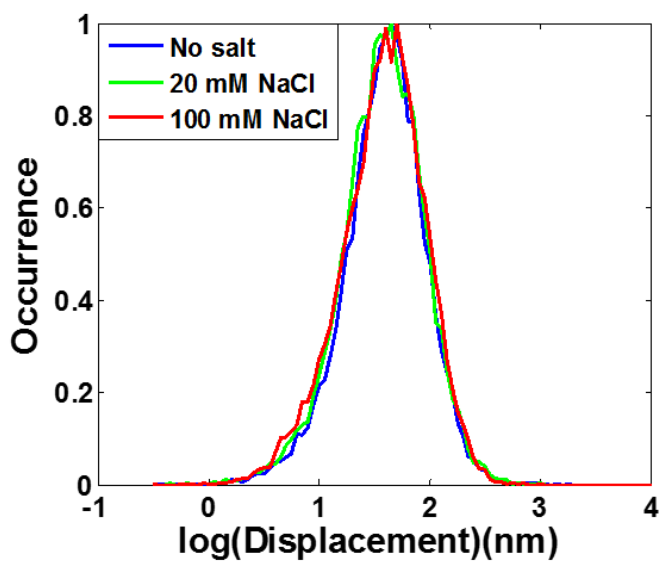


Figure S5. Lys single frame displacement distributions of Lys at varied ionic conditions. These results indicate that Lys dynamics at PS are not driven by electrostatics.

Lys Surface Residence Time Fitting Results for mPEG doped PS

Surface	A ₁ (%)	k ₁ (s ⁻¹)	A ₂ (%)	k ₂ (s ⁻¹)
Pure PS	54.7±0.2	12.9±0.1	16.0±0.1	1.56±0.01
mPEG/PS	53.3±0.3	11.7±0.1	15.6±0.1	1.51±0.01

Table S5. Fit results from residence time distributions of Lys. from data in Fig.

4B using $P(t) = A_1 e^{-k_1 t} + A_2 e^{-k_2 t}$ (Equation 4.2)²⁴⁶ indicating that the overall desorption from the mPEG doped PS is slower.

References

1. National Academies of Sciences, E., and Medicine *A Research Agenda for Transforming Separation Science*; Washington, DC, 2019.
2. McGrath, N. A.; Brichacek, M.; Njardarson, J. T. A graphical journey of innovative organic architectures that have improved our lives. *J. Chem. Educ.* **2010**, *87*, 1348-1349.
3. Moringo, N. A.; Shen, H.; Bishop, L. D.; Wang, W.; Landes, C. F. Enhancing Analytical Separations Using Super-Resolution Microscopy. *Annu. Rev. Phys. Chem.* **2018**, *69*, 353-375.
4. Avorn, J. The \$2.6 billion pill—methodologic and policy considerations. *New England Journal of Medicine* **2015**, *372*, 1877-1879.
5. Ahuja, S., *Handbook of bioseparations*. Academic press: 2000; Vol. 2.
6. Brady, R.; Woonton, B.; Gee, M. L.; O'Connor, A. J. Hierarchical mesoporous silica materials for separation of functional food ingredients—A review. *Innovative food science & emerging technologies* **2008**, *9*, 243-248.
7. Langer, E. S. *Annual Report and Survey of Biopharmaceutical Manufacturing Capacity and Production* BioPlan Associates April 2017, 2017.
8. Thömmes, J.; Kula, M. R. Membrane chromatography—an integrative concept in the downstream processing of proteins. *Biotechnol. Prog.* **1995**, *11*, 357-367.
9. Shukla, A. A.; Hubbard, B.; Tressel, T.; Guhan, S.; Low, D. Downstream processing of monoclonal antibodies—application of platform approaches. *J. Chromatogr. B* **2007**, *848*, 28-39.
10. Lowe, C. R.; Lowe, A. R.; Gupta, G. New developments in affinity chromatography with potential application in the production of biopharmaceuticals. *J. Biochem. Bioph. Methods* **2001**, *49*, 561-574.
11. Butcher, L. Employers Struggle To Cope With the Rising Use of Biologics: Tradeoffs in cost sharing or higher deductibles could derail treatment and decrease the value of healthcare spending. *Biotechnology Healthcare* **2011**, *8*, 21-24.
12. Walsh, G. Biopharmaceutical benchmarks *Nat. Biotechnol.* **2014**, *32*, 992-1000.
13. Lan, Q.; Bassi, A. S.; Zhu, J.-X.; Margaritis, A. A modified Langmuir model for the prediction of the effects of ionic strength on the equilibrium characteristics of protein adsorption onto ion exchange/affinity adsorbents. *Chem. Eng. J.* **2001**, *81*, 179-186.
14. Chang, C.; Lenhoff, A. M. Comparison of protein adsorption isotherms and uptake rates in preparative cation-exchange materials. *J. Chromatogr. A* **1998**, *827*, 281-293.
15. Murch, D. Height of equivalent theoretical plate in packed fractionation columns. *Industrial & Engineering Chemistry* **1953**, *45*, 2616-2621.
16. Peters, W. A. Calculations on fractionating columns from theoretical data. *Ind. Eng. Chem.* **1923**, *15*, 402-403.

17. van Deemter, J. J.; Zuiderweg, F. J.; Klinkenberg, A. Longitudinal diffusion and resistance to mass transfer as causes of nonideality in chromatography. *Chem. Eng. Sci.* **1956**, *5*, 271-289.
18. Giddings, J. C.; Eyring, H. A Molecular Dynamic Theory of Chromatography. *J. Phys. Chem.* **1955**, *59*, 416-421.
19. von Diezmann, A.; Shechtman, Y.; Moerner, W. E. Three-Dimensional Localization of Single Molecules for Super-Resolution Imaging and Single-Particle Tracking. *Chem. Rev.* **2017**, *117*, 7244-7275.
20. Shen, H.; Tauzin, L. J.; Baiyasi, R.; Wang, W.; Moringo, N.; Shuang, B.; Landes, C. F. Single Particle Tracking: From Theory to Biophysical Applications. *Chem. Rev.* **2017**.
21. Kisley, L.; Landes, C. F. Molecular approaches to chromatography using single molecule spectroscopy. *Anal. Chem.* **2014**, *87*, 83-98.
22. Annibale, P.; Dvornikov, A.; Gratton, E. Electrically tunable lens speeds up 3D orbital tracking. *Biomedical optics express* **2015**, *6*, 2181-2190.
23. Wang, W.; Shen, H.; Moringo, N. A.; Carrejo, N. C.; Ye, F.; Robinson, J. T.; Landes, C. F. Super-temporal resolved microscopy reveals multistep desorption kinetics of α -lactalbumin from nylon. *Langmuir* **2018**, *34*, 6697-6702.
24. Wang, W.; Shen, H.; Shuang, B.; Hoener, B. S.; Tauzin, L. J.; Moringo, N. A.; Kelly, K. F.; Landes, C. F. Super Temporal-Resolved Microscopy (STReM). *J. Phys. Chem. Lett.* **2016**.
25. Wang, W.; Ye, F.; Shen, H.; Moringo, N. A.; Dutta, C.; Robinson, J. T.; Landes, C. F. Generalized method to design phase masks for 3D super-resolution microscopy. *Optics Express* **2019**, *27*, 3799-3816.
26. Cho, N.-J.; Frank, C. W.; Kasemo, B.; Höök, F. Quartz crystal microbalance with dissipation monitoring of supported lipid bilayers on various substrates. *Nat. Protoc.* **2010**, *5*, 1096-1106.
27. Shuang, B.; Wang, W.; Shen, H.; Tauzin, L. J.; Flatebo, C.; Chen, J.; Moringo, N. A.; Bishop, L. D.; Kelly, K. F.; Landes, C. F. Generalized recovery algorithm for 3D super-resolution microscopy using rotating point spread functions. *Scientific Reports* **2016**, *6*, 30826.
28. Shuang, B.; Chen, J.; Kisley, L.; Landes, C. F. Troika of single particle tracking programing: SNR enhancement, particle identification, and mapping. *Phys. Chem. Chem. Phys.* **2014**, *16*, 624-34.
29. Shuang, B.; Byers, C. P.; Kisley, L.; Wang, L. Y.; Zhao, J. L.; Morimura, H.; Link, S.; Landes, C. F. Improved Analysis for Determining Diffusion Coefficients from Short, Single-Molecule Trajectories with Photoblinking. *Langmuir* **2013**, *29*, 228-234.
30. Wei, Q.; Becherer, T.; Angioletti-Uberti, S.; Dzubiella, J.; Wischke, C.; Neffe, A. T.; Lendlein, A.; Ballauff, M.; Haag, R. Protein interactions with polymer coatings and biomaterials. *Angew. Chem., Int. Ed. Engl.* **2014**, *53*, 8004-31.
31. Walder, R.; Kastantin, M.; Schwartz, D. K. High throughput single molecule tracking for analysis of rare populations and events. *Analyst* **2012**, *137*, 2987-2996.

32. Kisley, L.; Chen, J.; Mansur, A. P.; Shuang, B.; Kourentzi, K.; Poongavanam, M. V.; Chen, W. H.; Dhamane, S.; Willson, R. C.; Landes, C. F. Unified superresolution experiments and stochastic theory provide mechanistic insight into protein ion-exchange adsorptive separations. *Proc. Natl. Acad. Sci. U.S.A.* **2014**, *111*, 2075-80.
33. Lakowicz, J. R., *Principles of fluorescence spectroscopy*. Springer Science & Business Media: 2013.
34. Jablonski, A. Efficiency of anti-Stokes fluorescence in dyes. *Nature* **1933**, *131*, 839.
35. Condon, E. A theory of intensity distribution in band systems. *Physical Review* **1926**, *28*, 1182.
36. Franck, J.; Dymond, E. Elementary processes of photochemical reactions. *Transactions of the Faraday Society* **1926**, *21*, 536-542.
37. Kasha, M. Characterization of electronic transitions in complex molecules. *Discussions of the Faraday society* **1950**, *9*, 14-19.
38. Dean, K. M.; Palmer, A. E. Advances in fluorescence labeling strategies for dynamic cellular imaging. *Nature chemical biology* **2014**, *10*, 512.
39. Dempsey, G. T.; Vaughan, J. C.; Chen, K. H.; Bates, M.; Zhuang, X. Evaluation of fluorophores for optimal performance in localization-based super-resolution imaging. *Nat. Methods* **2011**, *8*, 1027.
40. Abbe, E. Beiträge zur Theorie des Mikroskops und der mikroskopischen Wahrnehmung. *Archiv für mikroskopische Anatomie* **1873**, *9*, 413-418.
41. Betzig, E.; Patterson, G. H.; Sougrat, R.; Lindwasser, O. W.; Olenych, S.; Bonifacino, J. S.; Davidson, M. W.; Lippincott-Schwartz, J.; Hess, H. F. Imaging Intracellular Fluorescent Proteins at Nanometer Resolution. *Science* **2006**, *313*, 1642-1645.
42. Dickson, R. M.; Cubitt, A. B.; Tsien, R. Y.; Moerner, W. On/off blinking and switching behaviour of single molecules of green fluorescent protein. *Nature* **1997**, *388*, 355-358.
43. Moerner, W. E.; Kador, L. Optical detection and spectroscopy of single molecules in a solid. *Physical review letters* **1989**, *62*, 2535.
44. Hell, S. W.; Kroug, M. Ground-state-depletion fluorescence microscopy: A concept for breaking the diffraction resolution limit. *Applied Physics B* **1995**, *60*, 495-497.
45. Hell, S. W.; Wichmann, J. Breaking the diffraction resolution limit by stimulated emission: stimulated-emission-depletion fluorescence microscopy. *Optics letters* **1994**, *19*, 780-782.
46. Möckl, L.; Lamb, D. C.; Bräuchle, C. Super-resolved Fluorescence Microscopy: Nobel Prize in Chemistry 2014 for Eric Betzig, Stefan Hell, and William E. Moerner. *Angew. Chem. Int. Ed.* **2014**, *53*, 13972-13977.
47. Chen, J. X.; Bremauntz, A.; Kisley, L.; Shuang, B.; Landes, C. F. Super-Resolution mbPAINT for Optical Localization of Single-Stranded DNA. *ACS. Appl. Mater Interfaces* **2013**, *5*, 9338-9343.

48. Rust, M. J.; Bates, M.; Zhuang, X. Sub-diffraction-limit imaging by stochastic optical reconstruction microscopy (STORM). *Nat. Methods* **2006**, *3*, 793.
49. Gustavsson, A.-K.; Petrov, P. N.; Lee, M. Y.; Shechtman, Y.; Moerner, W. 3D single-molecule super-resolution microscopy with a tilted light sheet. *Nat. Commun.* **2018**, *9*, 123.
50. De Silva Indrasekara, A. S.; Shuang, B.; Hollenhorst, F.; Hoener, B. S.; Hoggard, A.; Chen, S.; Villarreal, E.; Cai, Y.-Y.; Kisley, L.; Derry, P. J. Optimization of Spectral and Spatial Conditions to Improve Super-Resolution Imaging of Plasmonic Nanoparticles. *J. Phys. Chem. Lett.* **2017**.
51. Kisley, L.; Serrano, K. A.; Guin, D.; Kong, X.; Gruebele, M.; Leckband, D. E. Direct Imaging of Protein Stability and Folding Kinetics in Hydrogels. *ACS Appl. Mater. Interfaces* **2017**.
52. Kisley, L.; Patil, U.; Dhamane, S.; Kourentzi, K.; Tauzin, L. J.; Willson, R. C.; Landes, C. F. Competitive multicomponent anion exchange adsorption of proteins at the single molecule level. *Analyst* **2017**, 3127-3131.
53. Shen, H.; Tauzin, L. J.; Wang, W.; Hoener, B.; Shuang, B.; Kisley, L.; Hoggard, A.; Landes, C. F. Single-Molecule Kinetics of Protein Adsorption on Thin Nylon-6, 6 Films. *Anal. Chem.* **2016**, *88*, 9926-9933.
54. Lanzanò, L.; Gratton, E. Orbital single particle tracking on a commercial confocal microscope using piezoelectric stage feedback. *Methods Appl. Fluoresc.* **2014**, *2*, 024010.
55. Annibale, P.; Gratton, E. 3D orbital tracking of a DNA locus during the process of transcription. *Biophys. J.* **2014**, *106*, 394a-395a.
56. Han, J. J.; Kiss, C.; Bradbury, A. R.; Werner, J. H. Time-resolved, confocal single-molecule tracking of individual organic dyes and fluorescent proteins in three dimensions. *ACS Nano* **2012**, *6*, 8922-8932.
57. Wells, N. P.; Lessard, G. A.; Goodwin, P. M.; Phipps, M. E.; Cutler, P. J.; Lidke, D. S.; Wilson, B. S.; Werner, J. H. Time-resolved three-dimensional molecular tracking in live cells. *Nano Lett.* **2010**, *10*, 4732-4737.
58. Lessard, G. A.; Goodwin, P. M.; Werner, J. H. Three-dimensional tracking of individual quantum dots. *Applied Physics Letters* **2007**, *91*, 224106.
59. Joyce, W.; Joyce, A. Descartes, Newton, and Snell's law. *JOSA* **1976**, *66*, 1-8.
60. Chen, J.; Bremauntz, A.; Kisley, L.; Shuang, B.; Landes, C. F. Super-Resolution mbPAINT for Optical Localization of Single-Stranded DNA. *ACS Appl. Mater. Interfaces* **2013**, *5*, 9338-9343.
61. Guiochon, G.; Felinger, A.; Shirazi, D. G., *Fundamentals of preparative and nonlinear chromatography*. Academic Press: 2006.
62. Cavazzini, A.; Remelli, M.; Dondi, F. Stochastic theory of two-site adsorption chromatography by the characteristic function method. *J. Microcolumn Sep.* **1997**, *9*, 295-302.
63. Cavazzini, A.; Remelli, M.; Dondi, F.; Felinger, A. Stochastic theory of multiple-site linear adsorption chromatography. *Anal. Chem.* **1999**, *71*, 3453-3462.

64. Small, A.; Stahlheber, S. Fluorophore localization algorithms for super-resolution microscopy. *Nat. Methods* **2014**, *11*, 267-279.
65. Kisley, L.; Chen, J. X.; Mansur, A. P.; Dominguez-Medina, S.; Kulla, E.; Kang, M. K.; Shuang, B.; Kourentzi, K.; Poongavanam, M. V.; Dhamane, S.; Willson, R. C.; Landes, C. F. High ionic strength narrows the population of sites participating in protein ion-exchange adsorption: A single-molecule study. *J. Chromatogr. A* **2014**, *1343*, 135-142.
66. Giddings, J. C. Kinetic Origin of Tailing in Chromatography. *Anal. Chem.* **1963**, *35*, 1999-&.
67. Cano, T.; Offringa, N. D.; Willson, R. C. Competitive ion-exchange adsorption of proteins: Competitive isotherms with controlled competitor concentration. *J. Chromatogr. A* **2005**, *1079*, 116-126.
68. Yamamoto, S.; Nakanishi, K.; Matsuno, R., *Ion-Exchange Chromatography of Proteins*. Taylor & Francis: 1988.
69. Kato, K.; Ikada, Y. Selective adsorption of proteins to their ligands covalently immobilized onto microfibers. *Biotechnology and bioengineering* **1995**, *47*, 557-566.
70. Wirth, M. J.; Swinton, D. J. Single-molecule probing of mixed-mode adsorption at a chromatographic interface. *Anal. Chem.* **1998**, *70*, 5264-5271.
71. Wirth, M. J.; Swinton, D. J.; Ludes, M. D. Adsorption and diffusion of single molecules at chromatographic interfaces. *J. Phys. Chem. B* **2003**, *107*, 6258-6268.
72. Mabry, J. N.; Skaug, M. J.; Schwartz, D. K. Single-molecule insights into retention at a reversed-phase chromatographic interface. *Anal. Chem.* **2014**, *86*, 9451-9458.
73. Wirth, M. J.; Legg, M. A. Single-molecule probing of adsorption and diffusion on silica surfaces. *Annu. Rev. Phys. Chem.* **2007**, *58*, 489-510.
74. Fanali, S.; Haddad, P. R.; Poole, C.; Riekkola, M. L., *Liquid Chromatography: Fundamentals and Instrumentation*. Elsevier Science: 2017.
75. Pavani, S. R. P.; Piestun, R. In *3D fluorescent particle tracking with nanometer scale accuracies using a double-helix point spread function*, 2009 Conference on Lasers and Electro-Optics and 2009 Conference on Quantum electronics and Laser Science Conference, 2-4 June 2009; 2009; pp 1-2.
76. Pavani, S. R. P.; Thompson, M. A.; Biteen, J. S.; Lord, S. J.; Liu, N.; Twieg, R. J.; Piestun, R.; Moerner, W. E. Three-dimensional, single-molecule fluorescence imaging beyond the diffraction limit by using a double-helix point spread function. *Proc. Natl. Acad. Sci. U.S.A.* **2009**, *106*, 2995-2999.
77. Pavani, S. R. P.; Piestun, R. High-efficiency rotating point spread functions. *Optics Express* **2008**, *16*, 3484-3489.
78. Kisley, L.; Poongavanam, M. V.; Kourentzi, K.; Willson, R. C.; Landes, C. F. pH-dependence of single-protein adsorption and diffusion at a liquid chromatographic interface. *J. Sep. Sci.* **2016**, *39*, 682-688.
79. Skaug, M. J.; Mabry, J.; Schwartz, D. K. Intermittent Molecular Hopping at the Solid-Liquid Interface. *Physical Review Letters* **2013**, *110*, 256101.

80. Wertz, J. S.; Schwartz, D. K.; Kaar, J. L. Surface-Mediated Protein Unfolding as a Search Process for Denaturing Sites. *ACS Nano* **2016**, *10*, 730-738.
81. Tauzin, L. J.; Shuang, B.; Kisley, L.; Mansur, A. P.; Chen, J.; de Leon, A.; Advincula, R. C.; Landes, C. F. Charge-Dependent Transport Switching of Single Molecular Ions in a Weak Polyelectrolyte Multilayer. *Langmuir* **2014**, *30*, 8391-8399.
82. Wang, D.; Chin, H.-Y.; He, C.; Stoykovich, M. P.; Schwartz, D. K. Polymer Surface Transport Is a Combination of in-Plane Diffusion and Desorption-Mediated Flights. *ACS Macro Lett.* **2016**, *5*, 509-514.
83. McUmber, A. C.; Larson, N. R.; Randolph, T. W.; Schwartz, D. K. Molecular Trajectories Provide Signatures of Protein Clustering and Crowding at the Oil/Water Interface. *Langmuir* **2015**, *31*, 5882-5890.
84. Wang, D. P.; Hu, R. F.; Mabry, J. N.; Miao, B.; Wu, D. T.; Koynov, K.; Schwartz, D. K. Scaling of Polymer Dynamics at an Oil-Water Interface in Regimes Dominated by Viscous Drag and Desorption-Mediated Flights. *J. Am. Chem. Soc.* **2015**, *137*, 12312-12320.
85. Tauzin, L. J.; Shen, H.; Moringo, N. A.; Roddy, M. H.; Bothof, C. A.; Griesgraber, G. W.; McNulty, A. K.; Rasmussen, J. K.; Landes, C. F. Variable surface transport modalities on functionalized nylon films revealed with single molecule spectroscopy. *RSC Adv.* **2016**, *6*, 27760-27766.
86. Giri, D.; Ashraf, K. M.; Collinson, M. M.; Higgins, D. A. Single-Molecule Perspective on Mass Transport in Condensed Water Layers over Gradient Self-Assembled Monolayers. *J. Phys. Chem. C* **2015**, *119*, 9418-9428.
87. Sukhishvili, S. A.; Granick, S. Adsorption of human serum albumin: dependence on molecular architecture of the oppositely charged surface. *The Journal of chemical physics* **1999**, *110*, 10153-10161.
88. McNay, J. L.; Fernandez, E. J. How does a protein unfold on a reversed-phase liquid chromatography surface? *J. Chromatogr. A* **1999**, *849*, 135-148.
89. Benedek, K.; Dong, S.; Karger, B. Kinetics of unfolding of proteins on hydrophobic surfaces in reversed-phase liquid chromatography. *J. Chromatogr. A* **1984**, *317*, 227-243.
90. Ha, T.; Enderle, T.; Ogletree, D.; Chemla, D. S.; Selvin, P. R.; Weiss, S. Probing the interaction between two single molecules: fluorescence resonance energy transfer between a single donor and a single acceptor. *Proc. Natl. Acad. Sci. U.S.A.* **1996**, *93*, 6264-6268.
91. Roy, R.; Hohng, S.; Ha, T. A practical guide to single-molecule FRET. *Nat. Methods* **2008**, *5*, 507-516.
92. Weiss, S. Fluorescence spectroscopy of single biomolecules. *Science* **1999**, *283*, 1676-1683.
93. Darugar, Q.; Kim, H.; Gorelick, R. J.; Landes, C. Human T-cell lymphotropic virus type 1 nucleocapsid protein-induced structural changes in transactivation response DNA hairpin measured by single-molecule fluorescence resonance energy transfer. *Journal of virology* **2008**, *82*, 12164-12171.

94. Shaikh, S. A.; Dolino, D. M.; Lee, G.; Chatterjee, S.; MacLean, D. M.; Flatebo, C.; Landes, C. F.; Jayaraman, V. Stargazin Modulation of AMPA Receptors. *Cell reports* **2016**, *17*, 328-335.
95. Cooper, D. R.; Dolino, D. M.; Jaurich, H.; Shuang, B.; Ramaswamy, S.; Nurik, C. E.; Chen, J.; Jayaraman, V.; Landes, C. F. Conformational transitions in the glycine-bound GluN1 NMDA receptor LBD via single-molecule FRET. *Biophys. J.* **2015**, *109*, 66-75.
96. Chen, J. X.; Poddar, N. K.; Tauzin, L. J.; Cooper, D.; Kolomeisky, A. B.; Landes, C. F. Single-Molecule FRET Studies of HIV TAR-DNA Hairpin Unfolding Dynamics. *J. Phys. Chem. B* **2014**, *118*, 12130-12139.
97. Chen, T.-Y.; Santiago, A. G.; Jung, W.; Krzemiński, Ł.; Yang, F.; Martell, D. J.; Helmann, J. D.; Chen, P. Concentration- and chromosome-organization-dependent regulator unbinding from DNA for transcription regulation in living cells. *Nat. Commun.* **2015**, *6*.
98. Ramaswamy, S.; Cooper, D.; Poddar, N.; MacLean, D. M.; Rambhadrán, A.; Taylor, J. N.; Uhm, H.; Landes, C. F.; Jayaraman, V. Role of conformational dynamics in α -amino-3-hydroxy-5-methylisoxazole-4-propionic acid (AMPA) receptor partial agonism. *J. Biol. Chem.* **2012**, *287*, 43557-43564.
99. Jäger, M.; Nir, E.; Weiss, S. Site-specific labeling of proteins for single-molecule FRET by combining chemical and enzymatic modification. *Protein Sci.* **2006**, *15*, 640-646.
100. Yang, J.-Y.; Yang, W. Y. Site-specific two-color protein labeling for FRET studies using split inteins. *J. Am. Chem. Soc.* **2009**, *131*, 11644-11645.
101. Faulón Marruecos, D.; Kastantin, M.; Schwartz, D. K.; Kaar, J. L. Dense Poly (ethylene glycol) Brushes Reduce Adsorption and Stabilize the Unfolded Conformation of Fibronectin. *Biomacromolecules* **2016**, *17*, 1017-1025.
102. McLoughlin, S. Y.; Kastantin, M.; Schwartz, D. K.; Kaar, J. L. Single-molecule resolution of protein structure and interfacial dynamics on biomaterial surfaces. *Proc. Natl. Acad. Sci. U.S.A.* **2013**, *110*, 19396-19401.
103. Felsovalyi, F.; Patel, T.; Mangiagalli, P.; Kumar, S. K.; Banta, S. Effect of thermal stability on protein adsorption to silica using homologous aldo-keto reductases. *Protein Sci.* **2012**, *21*, 1113-1125.
104. Felsovalyi, F.; Mangiagalli, P.; Bureau, C.; Kumar, S. K.; Banta, S. Reversibility of the adsorption of lysozyme on silica. *Langmuir* **2011**, *27*, 11873-11882.
105. Weltz, J. S.; Schwartz, D. K.; Kaar, J. L. Surface-Mediated Protein Unfolding as a Search Process for Denaturing Sites. *ACS Nano* **2015**, *10*, 730-738.
106. Langdon, B. B.; Kastantin, M.; Schwartz, D. K. Surface Chemistry Influences Interfacial Fibrinogen Self-Association. *Biomacromolecules* **2015**, *16*, 3201-3208.
107. Fisher, M. E.; Kolomeisky, A. B. Molecular motors and the forces they exert. *Physica A: Statistical Mechanics and its Applications* **1999**, *274*, 241-266.
108. Kastantin, M.; Langdon, B. B.; Chang, E. L.; Schwartz, D. K. Single-molecule resolution of interfacial fibrinogen behavior: Effects of oligomer populations and surface chemistry. *J. Am. Chem. Soc.* **2011**, *133*, 4975-4983.

109. Chung, H. S.; Louis, J. M.; Eaton, W. A. Experimental determination of upper bound for transition path times in protein folding from single-molecule photon-by-photon trajectories. *Proc. Natl. Acad. Sci. U.S.A.* **2009**, *106*, 11837-11844.
110. Nettels, D.; Hoffmann, A.; Schuler, B. Unfolded protein and peptide dynamics investigated with single-molecule FRET and correlation spectroscopy from picoseconds to seconds. *J. Phys. Chem. B.* **2008**, *112*, 6137-6146.
111. Nettels, D.; Gopich, I. V.; Hoffmann, A.; Schuler, B. Ultrafast dynamics of protein collapse from single-molecule photon statistics. *Proc. Natl. Acad. Sci. U.S.A.* **2007**, *104*, 2655-2660.
112. Saito, M.; Kamonprasertsuk, S.; Suzuki, S.; Nanatani, K.; Oikawa, H.; Kushiro, K.; Takai, M.; Chen, P.-t.; Chen, E. H.-L.; Chen, R. P.-Y. Significant heterogeneity and slow dynamics of the unfolded ubiquitin detected by the line confocal method of single-molecule fluorescence spectroscopy. *J. Phys. Chem. B.* **2016**, *120*, 8818-8829.
113. Phizicky, E. M.; Fields, S. Protein-protein interactions: methods for detection and analysis. *Microbiological reviews* **1995**, *59*, 94-123.
114. Song, S.; Xie, T.; Ravensbergen, K.; Hahm, J. I. Ascertaining effects of nanoscale polymeric interfaces on competitive protein adsorption at the individual protein level. *Nanoscale* **2016**, *8*, 3496-509.
115. Hirsh, S. L.; McKenzie, D. R.; Nosworthy, N. J.; Denman, J. A.; Sezerman, O. U.; Bilek, M. M. The Vroman effect: competitive protein exchange with dynamic multilayer protein aggregates. *Colloids and Surfaces, B: Biointerfaces* **2013**, *103*, 395-404.
116. Vroman, L.; Adams, A.; Fischer, G.; Munoz, P. Interaction of high molecular weight kininogen, factor XII, and fibrinogen in plasma at interfaces. *Blood* **1980**, *55*, 156-159.
117. Vroman, L.; Adams, A. L. Findings with the recording ellipsometer suggesting rapid exchange of specific plasma proteins at liquid/solid interfaces. *Surf. Sci.* **1969**, *16*, 438-446.
118. Inoue, G.; Kawase, M. Understanding formation mechanism of heterogeneous porous structure of catalyst layer in polymer electrolyte fuel cell. *Int. J. Hydrogen Energy* **2016**, *41*, 21352-21365.
119. Craig, A. A.; Imrie, C. T. Effect of Backbone Flexibility on the Thermal Properties of Side-Group Liquid-Crystal Polymers. *Macromolecules* **1999**, *32*, 6215-6220.
120. Bakry, R.; Bonn, G. K.; Mair, D.; Svec, F. Monolithic Porous Polymer Layer for the Separation of Peptides and Proteins Using Thin-Layer Chromatography Coupled with MALDI-TOF-MS. *Anal. Chem.* **2007**, *79*, 486-493.
121. Cai, Y.; Chen, Y.; Hong, X.; Liu, Z.; Yuan, W. Porous microsphere and its applications. *International journal of nanomedicine* **2013**, *8*, 1111.
122. Maaloum, M.; Pernodet, N.; Tinland, B. Agarose gel structure using atomic force microscopy: Gel concentration and ionic strength effects. *ELECTROPHORESIS* **1998**, *19*, 1606-1610.

123. Gallagher, S.; Florea, L.; Fraser, K. J.; Diamond, D. Swelling and shrinking properties of thermo-responsive polymeric ionic liquid hydrogels with embedded linear pNIPAAm. *Int. J. Mol. Sci.* **2014**, *15*, 5337-5349.
124. Cooper, J. T.; Peterson, E. M.; Harris, J. M. Fluorescence Imaging of Single-Molecule Retention Trajectories in Reversed-Phase Chromatographic Particles. *Anal. Chem.* **2013**, *85*, 9363-9370.
125. Cooper, J.; Harris, J. M. Fluorescence-correlation spectroscopy study of molecular transport within reversed-phase chromatographic particles compared to planar model surfaces. *Anal. Chem.* **2014**, *86*, 11766-11772.
126. Kisley, L.; Brunetti, R.; Tauzin, L. J.; Shuang, B.; Yi, X.; Kirkeminde, A. W.; Higgins, D. A.; Weiss, S.; Landes, C. F. Characterization of Porous Materials by Fluorescence Correlation Spectroscopy Super-resolution Optical Fluctuation Imaging. *ACS Nano* **2015**, *9*, 9158-9166.
127. Yamaguchi, N.; Zhang, L.; Chae, B.-S.; Palla, C. S.; Furst, E. M.; Kiick, K. L. Growth Factor Mediated Assembly of Cell Receptor-Responsive Hydrogels. *J. Am. Chem. Soc.* **2007**, *129*, 3040-3041.
128. Dhar, A.; Samiotakis, A.; Ebbinghaus, S.; Nienhaus, L.; Homouz, D.; Gruebele, M.; Cheung, M. S. Structure, function, and folding of phosphoglycerate kinase are strongly perturbed by macromolecular crowding. *Proc. Natl. Acad. Sci. U.S.A.* **2010**, *107*, 17586-17591.
129. Langecker, M.; Arnaut, V.; Martin, T. G.; List, J.; Renner, S.; Mayer, M.; Dietz, H.; Simmel, F. C. Synthetic Lipid Membrane Channels Formed by Designed DNA Nanostructures. *Science* **2012**, *338*, 932-936.
130. Dertinger, T.; Colyer, R.; Iyer, G.; Weiss, S.; Enderlein, J. Fast, background-free, 3D super-resolution optical fluctuation imaging (SOFI). *Proc. Natl. Acad. Sci. U.S.A.* **2009**, *106*, 22287-22292.
131. Hoyer, P.; de Medeiros, G.; Balázs, B.; Norlin, N.; Besir, C.; Hanne, J.; Kräusslich, H.-G.; Engelhardt, J.; Sahl, S. J.; Hell, S. W.; Hufnagel, L. Breaking the diffraction limit of light-sheet fluorescence microscopy by RESOLFT. *Proc. Natl. Acad. Sci. U.S.A.* **2016**, *113*, 3442-3446.
132. Prabhat, P.; Ram, S.; Ward, E. S.; Ober, R. J. Simultaneous imaging of different focal planes in fluorescence microscopy for the study of cellular dynamics in three dimensions. *IEEE Transactions on NanoBioscience* **2004**, *3*, 237-242.
133. Ram, S.; Chao, J.; Prabhat, P.; Ward, E. S.; Ober, R. J. In *A novel approach to determining the three-dimensional location of microscopic objects with applications to 3D particle tracking*, 2007; pp 64430D-64430D-7.
134. Huang, B.; Wang, W.; Bates, M.; Zhuang, X. Three-Dimensional Super-Resolution Imaging by Stochastic Optical Reconstruction Microscopy. *Science* **2008**, *319*, 810-813.
135. Lien, C.-H.; Lin, C.-Y.; Chen, S.-J.; Chien, F.-C. Dynamic particle tracking via temporal focusing multiphoton microscopy with astigmatism imaging. *Optics Express* **2014**, *22*, 27290-27299.

136. Power, R. M.; Huisken, J. A guide to light-sheet fluorescence microscopy for multiscale imaging. *Nat Meth* **2017**, *14*, 360-373.
137. Keller, P. J.; Schmidt, A. D.; Wittbrodt, J.; Stelzer, E. H. K. Reconstruction of Zebrafish Early Embryonic Development by Scanned Light Sheet Microscopy. *Science* **2008**, *322*, 1065-1069.
138. Badieirostami, M.; Lew, M. D.; Thompson, M. A.; Moerner, W. E. Three-dimensional localization precision of the double-helix point spread function versus astigmatism and biplane. *Applied Physics Letters* **2010**, *97*, 161103.
139. Backer, A. S.; Moerner, W. E. Extending Single-Molecule Microscopy Using Optical Fourier Processing. *J. Phys. Chem. B* **2014**, *118*, 8313-8329.
140. Fienup, J. R. Phase retrieval algorithms: a comparison. *Appl. Opt.* **1982**, *21*, 2758-2769.
141. Bauschke, H. H.; Combettes, P. L.; Luke, D. R. Phase retrieval, error reduction algorithm, and Fienup variants: a view from convex optimization. *JOSA A* **2002**, *19*, 1334-1345.
142. MacBeath, G.; Schreiber, S. L. Printing proteins as microarrays for high-throughput function determination. *Science* **2000**, *289*, 1760-1763.
143. Talapatra, A.; Rouse, R.; Hardiman, G. Protein microarrays: challenges and promises. *Pharmacogenomics* **2002**, *3*, 527-536.
144. Zhu, H.; Snyder, M. Protein chip technology. *Curr. Opin. Chem. Biol.* **2003**, *7*, 55-63.
145. Hahm, J. I. Fundamentals of Nanoscale Polymer-Protein Interactions and Potential Contributions to Solid-State Nanobioarrays. *Langmuir* **2014**, *30*, 9891-9904.
146. Ribeiro, M.; Monteiro, F. J.; Ferraz, M. P. Infection of orthopedic implants with emphasis on bacterial adhesion process and techniques used in studying bacterial-material interactions. *Biomatter* **2012**, *2*, 176-194.
147. Ratner, B. D. Replacing and renewing: synthetic materials, biomimetics, and tissue engineering in implant dentistry. *Journal of Dental Education* **2001**, *65*, 1340-1347.
148. Anderson, J. M. Biological responses to materials. *Annu. Rev. Mater. Res.* **2001**, *31*, 81-110.
149. Liu, H. F.; Ma, J.; Winter, C.; Bayer, R. Recovery and purification process development for monoclonal antibody production. *mAbs* **2010**, *2*, 480-499.
150. Smith, C. Striving for purity: advances in protein purification. *Nat. Methods* **2005**, *2*, 71-77.
151. Daniels, C. R.; Kisley, L.; Kim, H.; Chen, W. H.; Poongavanam, M. V.; Reznik, C.; Kourentzi, K.; Willson, R. C.; Landes, C. F. Fluorescence correlation spectroscopy study of protein transport and dynamic interactions with clustered-charge peptide adsorbents. *J. Mol. Recognit.* **2012**, *25*, 435-442.
152. MacKerell Jr, A. D.; Bashford, D.; Bellott, M.; Dunbrack Jr, R. L.; Evanseck, J. D.; Field, M. J.; Fischer, S.; Gao, J.; Guo, H.; Ha, S. All-atom empirical potential for

- molecular modeling and dynamics studies of proteins. *J. Phys. Chem. B* **1998**, *102*, 3586-3616.
153. Onuchic, J. N.; Wolynes, P. G. Theory of protein folding. *Curr. Opin. Struct. Biol.* **2004**, *14*, 70-75.
154. Kurplus, M.; McCammon, J. Dynamics of proteins: elements and function. *Annu. Rev. Biochem.* **1983**, *52*, 263-300.
155. Kolomeisky, A. B.; Fisher, M. E. Molecular motors: a theorist's perspective. *Annu. Rev. Phys. Chem.* **2007**, *58*, 675-695.
156. Haïdopoulos, M.; Horgnies, M.; Mirabella, F.; Pireaux, J. J. Angle-Resolved XPS Study of Plasma-Deposited Polystyrene Films after Oxygen Plasma Treatment. *Plasma Processes and Polymers* **2008**, *5*, 67-75.
157. Klein, R. J.; Fischer, D. A.; Lenhart, J. L. Systematic oxidation of polystyrene by ultraviolet-ozone, characterized by near-edge X-ray absorption fine structure and contact angle. *Langmuir* **2008**, *24*, 8187-8197.
158. Zhang, D.; Dougal, S.; Yeganeh, M. Effects of UV irradiation and plasma treatment on a polystyrene surface studied by IR-visible sum frequency generation spectroscopy. *Langmuir* **2000**, *16*, 4528-4532.
159. Teare, D.; Ton-That, C.; Bradley, R. Surface characterization and ageing of ultraviolet-ozone-treated polymers using atomic force microscopy and x-ray photoelectron spectroscopy. *Sur. Interface Anal.* **2000**, *29*, 276-283.
160. Nabe, A.; Staude, E.; Belfort, G. Surface modification of polysulfone ultrafiltration membranes and fouling by BSA solutions. *J. Membr. Sci.* **1997**, *133*, 57-72.
161. Daniels, C. R.; Reznik, C. G.; Kilmer, R.; Felipe, M. J.; Tria, C. M.; Kourentzi, K.; Chen, W. H.; Willson, R. C.; Advincula, R. C.; Landes, C. F. Permeability of anti-fouling PEGylated surfaces probed by fluorescence correlation spectroscopy. *Abstr Pap Am Chem S* **2011**, 242.
162. Chen, S.; Li, L.; Zhao, C.; Zheng, J. Surface hydration: principles and applications toward low-fouling/nonfouling biomaterials. *Polymer* **2010**, *51*, 5283-5293.
163. Lyu, S.; Untereker, D. Degradability of polymers for implantable biomedical devices. *Int. J. Mol. Sci.* **2009**, *10*, 4033-4065.
164. Chu, P. K.; Chen, J.; Wang, L.; Huang, N. Plasma-surface modification of biomaterials. *Mat. Sci. Eng.,R* **2002**, *36*, 143-206.
165. Anand, G.; Zhang, F.; Linhardt, R. J.; Belfort, G. Protein-associated water and secondary structure effect removal of blood proteins from metallic substrates. *Langmuir* **2010**, *27*, 1830-1836.
166. Lindman, S.; Lynch, I.; Thulin, E.; Nilsson, H.; Dawson, K. A.; Linse, S. Systematic investigation of the thermodynamics of HSA adsorption to N-isopropylacrylamide/N-tert-butylacrylamide copolymer nanoparticles. Effects of particle size and hydrophobicity. *Nano Lett.* **2007**, *7*, 914-920.
167. Cedervall, T.; Lynch, I.; Lindman, S.; Berggård, T.; Thulin, E.; Nilsson, H.; Dawson, K. A.; Linse, S. Understanding the nanoparticle-protein corona using

methods to quantify exchange rates and affinities of proteins for nanoparticles. *Proc. Natl. Acad. Sci. U.S.A.* **2007**, *104*, 2050-2055.

168. Hirn, R.; Schuster, B.; Sleytr, U. B.; Bayerl, T. M. The effect of S-layer protein adsorption and crystallization on the collective motion of a planar lipid bilayer studied by dynamic light scattering. *Biophys. J.* **1999**, *77*, 2066-2074.

169. Kisley, L.; Chen, J.; Mansur, A. P.; Dominguez-Medina, S.; Kulla, E.; Kang, M. K.; Shuang, B.; Kourentzi, K.; Poongavanam, M.-V.; Dhamane, S. High ionic strength narrows the population of sites participating in protein ion-exchange adsorption: A single-molecule study. *J. Chromatogr. A* **2014**, *1343*, 135-142.

170. Kastantin, M.; Walder, R.; Schwartz, D. K. Identifying Mechanisms of Interfacial Dynamics Using Single-Molecule Tracking. *Langmuir* **2012**, *28*, 12443-12456.

171. Higgins, D. A.; Tran-Ba, K.-H.; Ito, T. Following Single Molecules to a Better Understanding of Self-Assembled One-Dimensional Nanostructures. *J. Phys. Chem. Lett.* **2013**, *4*, 3095-3103.

172. Peterson, E. M.; Manhart, M. W.; Harris, J. M. Single-Molecule Fluorescence Imaging of Interfacial DNA Hybridization Kinetics at Selective Capture Surfaces. *Anal. Chem.* **2016**, *88*, 1345-1354.

173. Welsher, K.; Yang, H. Multi-resolution 3D visualization of the early stages of cellular uptake of peptide-coated nanoparticles. *Nat. Nanotechnol.* **2014**, *9*, 198-203.

174. Perillo, E. P.; Liu, Y.-L.; Huynh, K.; Liu, C.; Chou, C.-K.; Hung, M.-C.; Yeh, H.-C.; Dunn, A. K. Deep and high-resolution three-dimensional tracking of single particles using nonlinear and multiplexed illumination. *Nat. Commun.* **2015**, *6*.

175. Jaqaman, K.; Loerke, D.; Mettlen, M.; Kuwata, H.; Grinstein, S.; Schmid, S. L.; Danuser, G. Robust single-particle tracking in live-cell time-lapse sequences. *Nat. Methods* **2008**, *5*, 695-702.

176. Landes, C. F. Single-molecule tracking and super-resolution imaging shed light on cholera toxin transcription activation. *Mol. Microbiol.* **2015**, *96*, 1-3.

177. Lupo, K. M.; Hinton, D. A.; Ng, J. D.; Padilla, N. A.; Goldsmith, R. H. Probing heterogeneity and bonding at silica surfaces through single-molecule investigation of base-mediated linkage failure. *Langmuir* **2016**, *32*, 9171-9179.

178. Kisley, L.; Brunetti, R.; Tauzin, L. J.; Shuang, B.; Yi, X. Y.; Kirkeminde, A. W.; Higgins, D. A.; Weiss, S.; Landes, C. F. Characterization of Porous Materials by Fluorescence Correlation Spectroscopy Super-resolution Optical Fluctuation Imaging. *ACS Nano* **2015**, *9*, 9158-9166.

179. Kastantin, M.; Keller, T. F.; Jandt, K. D.; Schwartz, D. K. Single-Molecule Tracking of Fibrinogen Dynamics on Nanostructured Poly (ethylene) Films. *Adv. Funct. Mater.* **2012**, *22*, 2617-2623.

180. Langdon, B. B.; Mirhossaini, R. B.; Mabry, J. N.; Sriram, I.; Lajmi, A.; Zhang, Y. X.; Rojas, O. J.; Schwartz, D. K. Single-Molecule Resolution of Protein Dynamics on Polymeric Membrane Surfaces: The Roles of Spatial and Population Heterogeneity. *ACS Appl. Mater. Interfaces* **2015**, *7*, 3607-3617.

181. Yu, C.; Granick, S. Revisiting Polymer Surface Diffusion in the Extreme Case of Strong Adsorption. *Langmuir* **2014**, *30*, 14538-14544.
182. Chin, H.-Y.; Wang, D.; Schwartz, D. K. Dynamic Molecular Behavior on Thermoresponsive Polymer Brushes. *Macromolecules* **2015**, *48*, 4562-4571.
183. Murray, T. D.; Lyubimov, A. Y.; Ogata, C. M.; Vo, H.; Uervirojnangkoorn, M.; Brunger, A. T.; Berger, J. M. A high-transparency, micro-patternable chip for X-ray diffraction analysis of microcrystals under native growth conditions. *Acta Crystallogr., Sect. D: Biol. Crystallogr.* **2015**, *71*, 1987-1997.
184. Fleming, A.; Allison, V. Observations on a bacteriolytic substance ("lysozyme") found in secretions and tissues. *Br. J. Exp. Pathol.* **1922**, *3*, 252.
185. Kappes, R. S.; Schönfeld, F.; Li, C.; Golriz, A. A.; Nagel, M.; Lippert, T.; Butt, H.-J.; Gutmann, J. S. A study of photothermal laser ablation of various polymers on microsecond time scales. *SpringerPlus* **2014**, *3*, 1.
186. Teare, D.; Emmison, N.; Ton-That, C.; Bradley, R. Cellular attachment to ultraviolet ozone modified polystyrene surfaces. *Langmuir* **2000**, *16*, 2818-2824.
187. Banerjee, I.; Pangule, R. C.; Kane, R. S. Antifouling coatings: recent developments in the design of surfaces that prevent fouling by proteins, bacteria, and marine organisms. *Adv. Mater.* **2011**, *23*, 690-718.
188. Feng, Y.; Borrelli, M.; Meyer-ter-Vehn, T.; Reichl, S.; Schrader, S.; Geerling, G. Epithelial wound healing on keratin film, amniotic membrane and polystyrene in vitro. *Curr. Eye Res.* **2014**, *39*, 561-570.
189. Ma, H. M.; Davis, R. H.; Bowman, C. N. A novel sequential photoinduced living graft polymerization. *Macromolecules* **2000**, *33*, 331-335.
190. Yang, Q.; Hu, M.-X.; Dai, Z.-W.; Tian, J.; Xu, Z.-K. Fabrication of glycosylated surface on polymer membrane by UV-induced graft polymerization for lectin recognition. *Langmuir* **2006**, *22*, 9345-9349.
191. Xu, Z.-K.; Kou, R.-Q.; Liu, Z.-M.; Nie, F.-Q.; Xu, Y.-Y. Incorporating α -allyl glucoside into polyacrylonitrile by water-phase precipitation copolymerization to reduce protein adsorption and cell adhesion. *Macromolecules* **2003**, *36*, 2441-2447.
192. Ruch, D.; Boes, C.; Zimmer, R.; Migeon, H. N.; Muller, J. Surface oxidation of styrene butadiene copolymers: Study by laser ablation and secondary ion mass spectrometry. *J. Appl. Polym. Sci.* **2003**, *87*, 1910-1917.
193. Wertz, C. F.; Santore, M. M. Adsorption and reorientation kinetics of lysozyme on hydrophobic surfaces. *Langmuir* **2002**, *18*, 1190-1199.
194. Chandler, D. Interfaces and the driving force of hydrophobic assembly. *Nature* **2005**, *437*, 640-7.
195. Latour Jr, R. A. Molecular modeling of biomaterial surfaces. *Curr. Opin. Solid State Mater. Sci.* **1999**, *4*, 413-417.
196. Muntean, S. A.; Kemper, M.; van IJzendoorn, L. J.; Lyulin, A. V. Roughness and ordering at the interface of oxidized polystyrene and water. *Langmuir* **2011**, *27*, 8678-8686.
197. Trudeau, T. G.; Jena, K. C.; Hore, D. K. Water structure at solid surfaces of varying hydrophobicity. *J. Phys. Chem. C* **2009**, *113*, 20002-20008.

198. Sendner, C.; Horinek, D.; Bocquet, L.; Netz, R. R. Interfacial water at hydrophobic and hydrophilic surfaces: Slip, viscosity, and diffusion. *Langmuir* **2009**, *25*, 10768-10781.
199. Chapman, R. G.; Ostuni, E.; Takayama, S.; Holmlin, R. E.; Yan, L.; Whitesides, G. M. Surveying for surfaces that resist the adsorption of proteins. *J. Am. Chem. Soc.* **2000**, *122*, 8303-8304.
200. Ostuni, E.; Chapman, R. G.; Holmlin, R. E.; Takayama, S.; Whitesides, G. M. A survey of structure-property relationships of surfaces that resist the adsorption of protein. *Langmuir* **2001**, *17*, 5605-5620.
201. Vogler, E. A. Structure and reactivity of water at biomaterial surfaces. *Adv. Colloid Interface Sci.* **1998**, *74*, 69-117.
202. Elliott, L. C. C.; Barhoum, M.; Harris, J. M.; Bohn, P. W. Single Molecule Tracking Studies of Lower Critical Solution Temperature Transition Behavior in Poly(N-isopropylacrylamide). *Langmuir* **2011**, *27*, 11037-11043.
203. Elliott, L. C.; Barhoum, M.; Harris, J. M.; Bohn, P. W. Trajectory analysis of single molecules exhibiting non-Brownian motion. *Phys. Chem. Chem. Phys.* **2011**, *13*, 4326-4334.
204. Pertsin, A. J.; Grunze, M. Computer simulation of water near the surface of oligo (ethylene glycol)-terminated alkanethiol self-assembled monolayers. *Langmuir* **2000**, *16*, 8829-8841.
205. Myers, G. A.; Gacek, D. A.; Peterson, E. M.; Fox, C. B.; Harris, J. M. Microscopic Rates of Peptide-Phospholipid Bilayer Interactions from Single-Molecule Residence Times. *J. Am. Chem. Soc.* **2012**, *134*, 19652-19660.
206. Beaulieu, I.; Geissler, M.; Mauzeroll, J. Oxygen plasma treatment of polystyrene and zeonor: substrates for adhesion of patterned cells. *Langmuir* **2009**, *25*, 7169-7176.
207. Möller, J.; Schroer, M. A.; Erilkamp, M.; Grobelny, S.; Paulus, M.; Tiemeyer, S.; Wirkert, F. J.; Tolan, M.; Winter, R. The effect of ionic strength, temperature, and pressure on the interaction potential of dense protein solutions: from nonlinear pressure response to protein crystallization. *Biophys. J.* **2012**, *102*, 2641-2648.
208. Song, W.; Popp, L.; Yang, J.; Kumar, A.; Gangoli, V. S.; Segatori, L. The autophagic response to polystyrene nanoparticles is mediated by transcription factor EB and depends on surface charge. *Journal of nanobiotechnology* **2015**, *13*, 87.
209. Tu, A.; Kwag, H. R.; Barnette, A. L.; Kim, S. H. Water adsorption isotherms on CH₃-, OH-, and COOH-terminated organic surfaces at ambient conditions measured with PM-RAIRS. *Langmuir* **2012**, *28*, 15263-15269.
210. Harings, J. A.; Deshmukh, Y. S.; Hansen, M. R.; Graf, R.; Rastogi, S. Processing of polyamides in the presence of water via hydrophobic hydration and ionic interactions. *Macromolecules* **2012**, *45*, 5789-5797.
211. Parmar, A. S.; Muschol, M. Hydration and hydrodynamic interactions of lysozyme: effects of chaotropic versus kosmotropic ions. *Biophys. J.* **2009**, *97*, 590-598.

212. Zhang, L.; Radovic-Moreno, A. F.; Alexis, F.; Gu, F. X.; Basto, P. A.; Bagalkot, V.; Jon, S.; Langer, R. S.; Farokhzad, O. C. Co-delivery of hydrophobic and hydrophilic drugs from nanoparticle–aptamer bioconjugates. *ChemMedChem* **2007**, *2*, 1268-1271.
213. Detobel, F.; Fekete, V.; De Malsche, W.; De Bruyne, S.; Gardeniers, H.; Desmet, G. Estimation of surface desorption times in hydrophobically coated nanochannels and their effect on shear-driven and pressure-driven chromatography. *Anal. Bioanal. Chem.* **2009**, *394*, 399-411.
214. Xu, X.; Roman, J. M.; Veenstra, T. D.; Van Anda, J.; Ziegler, R. G.; Issaq, H. J. Analysis of fifteen estrogen metabolites using packed column supercritical fluid chromatography-mass spectrometry. *Anal. Chem.* **2006**, *78*, 1553-1558.
215. Burnouf, T.; Radosevich, M. Affinity chromatography in the industrial purification of plasma proteins for therapeutic use. *J. Biochem. Bioph. Methods* **2001**, *49*, 575-586.
216. Ladiwala, A.; Rege, K.; Breneman, C. M.; Cramer, S. M. A priori prediction of adsorption isotherm parameters and chromatographic behavior in ion-exchange systems. *Proc. Natl. Acad. Sci. U.S.A.* **2005**, *102*, 11710-11715.
217. Castillo, E.; Koenig, J.; Andersen, J.; Lo, J. Characterization of protein adsorption on soft contact lenses: I. Conformational changes of adsorbed human serum albumin. *Biomaterials* **1984**, *5*, 319-325.
218. Omali, N. B.; Subbaraman, L. N.; Coles-Brennan, C.; Fadli, Z.; Jones, L. W. Biological and clinical implications of lysozyme deposition on soft contact lenses. *Optometry and Vision Science* **2015**, *92*, 750.
219. Hahm, J.-i. Functional polymers in protein detection platforms: Optical, electrochemical, electrical, mass-sensitive, and magnetic biosensors. *Sensors* **2011**, *11*, 3327-3355.
220. Chen, M.; Khalid, S.; Sansom, M. S.; Bayley, H. Outer membrane protein G: Engineering a quiet pore for biosensing. *Proc. Natl. Acad. Sci. U.S.A.* **2008**, *105*, 6272-6277.
221. Baker, S. E.; Colavita, P. E.; Tse, K.-Y.; Hamers, R. J. Functionalized vertically aligned carbon nanofibers as scaffolds for immobilization and electrochemical detection of redox-active proteins. *Chem. Mater.* **2006**, *18*, 4415-4422.
222. Clare, T. L.; Clare, B. H.; Nichols, B. M.; Abbott, N. L.; Hamers, R. J. Functional monolayers for improved resistance to protein adsorption: oligo (ethylene glycol)-modified silicon and diamond surfaces. *Langmuir* **2005**, *21*, 6344-6355.
223. Sargent, R. N.; Graham, D. L. Salting-out chromatography of serum proteins. *Anal. Chim. Acta* **1964**, *30*, 101-104.
224. Arakawa, T.; Timasheff, S. N. Mechanism of protein salting in and salting out by divalent cation salts: balance between hydration and salt binding. *Biochemistry* **1984**, *23*, 5912-5923.
225. Stone, M. C.; Tao, Y.; Carta, G. Protein adsorption and transport in agarose and dextran-grafted agarose media for ion exchange chromatography: Effect of ionic strength and protein characteristics. *J. Chromatogr. A* **2009**, *1216*, 4465-4474.

226. Okur, H. I.; Hladílková, J.; Rembert, K. B.; Cho, Y.; Heyda, J.; Dzubiella, J.; Cremer, P. S.; Jungwirth, P. Beyond the Hofmeister series: ion-specific effects on proteins and their biological functions. *J. Phys. Chem. B.* **2017**, *121*, 1997-2014.
227. Hofmeister, F. Zur Lehre von der Wirkung der Salze–Untersuchungen über den Quellungsvorgang. *Archiv für experimentelle Pathologie und Pharmakologie* **1888**, 395-413.
228. Zhang, Y.; Cremer, P. S. The inverse and direct Hofmeister series for lysozyme. *Proc. Natl. Acad. Sci. U.S.A.* **2009**, *106*, 15249-15253.
229. Tsumoto, K.; Ejima, D.; Senczuk, A. M.; Kita, Y.; Arakawa, T. Effects of salts on protein–surface interactions: applications for column chromatography. *J. Pharm. Sci.* **2007**, *96*, 1677-1690.
230. Saxena, A.; Tripathi, B. P.; Kumar, M.; Shahi, V. K. Membrane-based techniques for the separation and purification of proteins: an overview. *Adv. Colloid Interface Sci.* **2009**, *145*, 1-22.
231. Dziennik, S.; Belcher, E.; Barker, G.; DeBergalis, M.; Fernandez, S.; Lenhoff, A. Nondiffusive mechanisms enhance protein uptake rates in ion exchange particles. *Proc. Natl. Acad. Sci. U.S.A.* **2003**, *100*, 420-425.
232. Vaisocherova, H.; Yang, W.; Zhang, Z.; Cao, Z.; Cheng, G.; Piliarik, M.; Homola, J.; Jiang, S. Ultralow fouling and functionalizable surface chemistry based on a zwitterionic polymer enabling sensitive and specific protein detection in undiluted blood plasma. *Anal. Chem.* **2008**, *80*, 7894-7901.
233. Welsch, N.; Lu, Y.; Dzubiella, J.; Ballauff, M. Adsorption of proteins to functional polymeric nanoparticles. *Polymer* **2013**, *54*, 2835-2849.
234. Rico, F.; Russek, A.; González, L.; Grubmüller, H.; Scheuring, S. Heterogeneous and rate-dependent streptavidin–biotin unbinding revealed by high-speed force spectroscopy and atomistic simulations. *Proc. Natl. Acad. Sci. U.S.A.* **2019**, 201816909.
235. Deich, J.; Judd, E.; McAdams, H.; Moerner, W. Visualization of the movement of single histidine kinase molecules in live *Caulobacter* cells. *Proc. Natl. Acad. Sci. U.S.A.* **2004**, *101*, 15921-15926.
236. Cohen, A. E.; Moerner, W. Suppressing Brownian motion of individual biomolecules in solution. *Proc. Natl. Acad. Sci. U.S.A.* **2006**, *103*, 4362-4365.
237. Wiedenmann, J.; Ivanchenko, S.; Oswald, F.; Schmitt, F.; Röcker, C.; Salih, A.; Spindler, K.-D.; Nienhaus, G. U. EosFP, a fluorescent marker protein with UV-inducible green-to-red fluorescence conversion. *Proc. Natl. Acad. Sci. U.S.A.* **2004**, *101*, 15905-15910.
238. Radadia, A. D.; Stavis, C. J.; Carr, R.; Zeng, H.; King, W. P.; Carlisle, J. A.; Aksimentiev, A.; Hamers, R. J.; Bashir, R. Control of nanoscale environment to improve stability of immobilized proteins on diamond surfaces. *Adv. Funct. Mater.* **2011**, *21*, 1040-1050.
239. Chung, W. K.; Freed, A. S.; Holstein, M. A.; McCallum, S. A.; Cramer, S. M. Evaluation of protein adsorption and preferred binding regions in multimodal chromatography using NMR. *Proc. Natl. Acad. Sci. U.S.A.* **2010**, *107*, 16811-16816.

240. Shechtman, Y.; Weiss, L. E.; Backer, A. S.; Sahl, S. J.; Moerner, W. Precise Three-Dimensional Scan-Free Multiple-Particle Tracking over Large Axial Ranges with Tetrapod Point Spread Functions. *Nano Lett.* **2015**, *15*, 4194-4199.
241. Quirin, S.; Pavani, S. R. P.; Piestun, R. Optimal 3D single-molecule localization for superresolution microscopy with aberrations and engineered point spread functions. *Proc. Natl. Acad. Sci. U.S.A.* **2012**, *109*, 675-679.
242. Moringo, N. A.; Shen, H.; Tauzin, L. J.; Wang, W.; Bishop, L. D.; Landes, C. F. Variable lysozyme transport dynamics on oxidatively functionalized polystyrene films. *Langmuir* **2017**, *33*, 10818-10828.
243. Shen, H.; Xu, W.; Chen, P. Single-molecule nanoscale electrocatalysis. *Phys. Chem. Chem. Phys.* **2010**, *12*, 6555-6563.
244. Shen, H.; Zhou, X.; Zou, N.; Chen, P. Single-molecule kinetics reveals a hidden surface reaction intermediate in single-nanoparticle catalysis. *J. Phys. Chem. C* **2014**, *118*, 26902-26911.
245. Andoy, N. M.; Zhou, X.; Choudhary, E.; Shen, H.; Liu, G.; Chen, P. Single-molecule catalysis mapping quantifies site-specific activity and uncovers radial activity gradient on single 2D nanocrystals. *J Am Chem Soc* **2013**, *135*, 1845-52.
246. Peterson, E. M.; Manhart, M. W.; Harris, J. M. Competitive Assays of Label-Free DNA Hybridization with Single-Molecule Fluorescence Imaging Detection. *Anal. Chem.* **2016**, *88*, 6410-6417.
247. Peterson, E. M.; Manhart, M. W.; Kriech, D. M.; Harris, J. M. Fluorescence microscopy of single-molecule DNA hybridization at high density interfaces. *Abstr Pap Am Chem S* **2014**, 248.
248. Schickinger, M.; Zacharias, M.; Dietz, H. Tethered multifluorophore motion reveals equilibrium transition kinetics of single DNA double helices. *Proc. Natl. Acad. Sci. U.S.A.* **2018**, *115*, E7512-E7521.
249. Weiss, L. E.; Milenkovic, L.; Yoon, J.; Stearns, T.; Moerner, W. Motional dynamics of single Patched1 molecules in cilia are controlled by Hedgehog and cholesterol. *Proc. Natl. Acad. Sci. U.S.A.* **2019**, 201816747.
250. Daniels, T. R.; Bernabeu, E.; Rodríguez, J. A.; Patel, S.; Kozman, M.; Chiappetta, D. A.; Holler, E.; Ljubimova, J. Y.; Helguera, G.; Penichet, M. L. The transferrin receptor and the targeted delivery of therapeutic agents against cancer. *Biochimica et Biophysica Acta (BBA)-General Subjects* **2012**, *1820*, 291-317.
251. Liang, W.; Li, Q.; Ferrara, N. Metastatic growth instructed by neutrophil-derived transferrin. *Proc. Natl. Acad. Sci. U.S.A.* **2018**, *115*, 11060-11065.
252. Jain, P.; Vyas, M. K.; Geiger, J. H.; Baker, G. L.; Bruening, M. L. Protein purification with polymeric affinity membranes containing functionalized poly (acid) brushes. *Biomacromolecules* **2010**, *11*, 1019-1026.
253. Zeng, X.; Ruckenstein, E. Membrane chromatography: preparation and applications to protein separation. *Biotechnol. Prog.* **1999**, *15*, 1003-1019.
254. Orr, V.; Zhong, L.; Moo-Young, M.; Chou, C. P. Recent advances in bioprocessing application of membrane chromatography. *Biotechnol. Adv.* **2013**, *31*, 450-465.

255. Kolesov, I.; Mileva, D.; Androsch, R. Mechanical behavior and optical transparency of polyamide 6 of different morphology formed by variation of the pathway of crystallization. *Polym. Bull.* **2014**, *71*, 581-593.
256. Handley, S., *Nylon: The Story of a Fashion Revolution: a Celebration of Design from Art Silk to Nylon and Thinking Fibres*. JHU Press: 1999.
257. Camper, D. V.; Viola, R. E. Fully automated protein purification. *Anal Biochem* **2009**, *393*, 176-181.
258. Suen, S.-Y.; Liu, Y.-C.; Chang, C.-S. Exploiting immobilized metal affinity membranes for the isolation or purification of therapeutically relevant species. *J. Chromatogr. B* **2003**, *797*, 305-319.
259. McQuarrie, D. A. On Stochastic Theory of Chromatography. *J. Chem. Phys.* **1963**, *38*, 437-445.
260. Felinger, A. Molecular dynamic theories in chromatography. *J. Chromatogr. A* **2008**, *1184*, 20-41.
261. Giddings, J. C. The random downstream migration of molecules in chromatography. *J. Chem. Educ.* **1958**, *35*, 588.
262. Pasti, L.; Cavazzini, A.; Felinger, A.; Martin, M.; Doni, F. Single-molecule observation and chromatography unified by levy process representation. *Anal. Chem.* **2005**, *77*, 2524-2535.
263. Hlushkou, D.; Gritti, F.; Daneyko, A.; Guiochon, G.; Tallarek, U. How Microscopic Characteristics of the Adsorption Kinetics Impact Macroscale Transport in Chromatographic Beds. *J. Phys. Chem. C* **2013**, *117*, 22974-22985.
264. Giddings, J. C. Nonequilibrium Kinetics and Chromatography. *J. Chem. Phys.* **1959**, *31*, 1462-1467.
265. Hlushkou, D.; Gritti, F.; Guiochon, G.; Seidel-Morgenstern, A.; Tallarek, U. Effect of adsorption on solute dispersion: a microscopic stochastic approach. *Anal. Chem.* **2014**, *86*, 4463-70.
266. Giddings, J. C., *Dynamics of Chromatography: Principles and Theory*. Marcel Dekker, Inc.: 1965; Vol. 1.
267. Wirth, M. J.; Legg, M. A., Single-molecule probing of adsorption and diffusion on silica surfaces. In *Annu. Rev. Phys. Chem.*, 2007; Vol. 58, pp 489-510.
268. Hlushkou, D.; Svidrytski, A.; Tallarek, U. Tracer-Size-Dependent Pore Space Accessibility and Long-Time Diffusion Coefficient in Amorphous, Mesoporous Silica. *J. Phys. Chem. C* **2017**, *121*, 8416-8426.
269. Gotmar, G.; Fornstedt, T.; Guiochon, G. Peak tailing and mass transfer kinetics in linear chromatography - Dependence on the column length and the linear velocity of the mobile phase. *J. Chromatogr. A* **1999**, *831*, 17-35.
270. Felinger, A. Molecular movement in an HPLC column: A stochastic analysis. *LCCG North Am.* **2004**, *22*, 642-647.
271. Giddings, J. C. Stochastic Considerations on Chromatographic Dispersion. *J. Chem. Phys.* **1957**, *26*, 169-173.
272. Kisley, L.; Chen, J. X.; Mansur, A. P.; Shuang, B.; Kourentzi, K.; Poongavanam, M. V.; Chen, W. H.; Dhamane, S.; Willson, R. C.; Landes, C. F. Unified superresolution

- experiments and stochastic theory provide mechanistic insight into protein ion-exchange adsorptive separations. *P. Natl. Acad. Sci. USA* **2014**, *111*, 2075-2080.
273. Savitzky, A.; Golay, M. J. E. Smoothing + differentiation of data by simplified least squares procedures. *Anal. Chem.* **1964**, *36*, 1627-1639.
274. Savitzky, A.; Golay, M. J. Smoothing and differentiation of data by simplified least squares procedures. *Anal. Chem.* **1964**, *36*, 1627-1639.
275. Shuang, B.; Byers, C. P.; Kisley, L.; Wang, L.-Y.; Zhao, J.; Morimura, H.; Link, S.; Landes, C. F. Improved analysis for determining diffusion coefficients from short, single-molecule trajectories with photoblinking. *Langmuir* **2012**, *29*, 228-234.
276. Yang, A. H.-W.; Macgillivray, R. T.; Chen, J.; Luo, Y.; Wang, Y.; Brayer, G. D.; Mason, A. B.; Woodworth, R. C.; Murphy, M. E. Crystal structures of two mutants (K206Q, H207E) of the N-lobe of human transferrin with increased affinity for iron. *Protein Sci.* **2000**, *9*, 49-52.
277. Tausin, L. J.; Shuang, B.; Kisley, L.; Mansur, A. P.; Chen, J. X.; de Leon, A.; Advincula, R. C.; Landes, C. F. Charge-Dependent Transport Switching of Single Molecular Ions in a Weak Polyelectrolyte Multilayer. *Langmuir* **2014**, *30*, 8391-8399.
278. Nelson, N.; Schwartz, D. K. Specific ion (Hofmeister) effects on adsorption, desorption, and diffusion at the solid-aqueous interface. *J. Phys. Chem. Lett.* **2013**, *4*, 4064-4068.
279. McUmber, A. C.; Randolph, T. W.; Schwartz, D. K. Electrostatic interactions influence protein adsorption (but not desorption) at the silica-aqueous interface. *J. Phys. Chem. Lett.* **2015**, *6*, 2583-2587.
280. Collins, K. D.; Washabaugh, M. W. The Hofmeister effect and the behaviour of water at interfaces. *Quarterly reviews of biophysics* **1985**, *18*, 323-422.
281. Hyde, A. M.; Zultanski, S. L.; Waldman, J. H.; Zhong, Y.-L.; Shevlin, M.; Peng, F. General principles and strategies for salting-out informed by the Hofmeister series. *Org. Process Res. Dev.* **2017**, *21*, 1355-1370.
282. Grover, P. K.; Ryall, R. L. Critical appraisal of salting-out and its implications for chemical and biological sciences. *Chem. Rev.* **2005**, *105*, 1-10.
283. Hovanessian, A. G.; Awdeh, Z. L. Gel Isoelectric Focusing of Human-Serum Transferrin. *Eur. J. Biochem.* **1976**, *68*, 333-338.
284. Zhang, X.; Bai, R. Adsorption behavior of humic acid onto polypyrrole-coated nylon 6, 6 granules. *J. Mater. Chem.* **2002**, *12*, 2733-2739.
285. Abdizadeh, H.; Atilgan, A. R.; Atilgan, C. Mechanisms by which salt concentration moderates the dynamics of human serum transferrin. *J. Phys. Chem. B.* **2017**, *121*, 4778-4789.
286. Zhang, X.; Bai, R. Immobilization of chitosan on nylon 6, 6 and PET granules through hydrolysis pretreatment. *J. Appl. Polym. Sci.* **2003**, *90*, 3973-3979.
287. Ohkuma, T.; Hara, S. Tail-producing slow adsorption—desorption process in liquid—solid chromatography. *J. Chromatogr. A* **1987**, *400*, 47-63.
288. Giddings, J. C.; Byring, H. A molecular dynamic theory of chromatography. *J. Phys. Chem.* **1955**, *59*, 416-421.

289. Micsonai, A.; Wien, F.; Kernya, L.; Lee, Y.-H.; Goto, Y.; Réfrégiers, M.; Kardos, J. Accurate secondary structure prediction and fold recognition for circular dichroism spectroscopy. *Proc. Natl. Acad. Sci. U.S.A.* **2015**, *112*, E3095-E3103.
290. Marruecos, D. F.; Schwartz, D. K.; Kaar, J. L. Impact of Surface Interactions on Protein Conformation. *Current Opinion in Colloid & Interface Science* **2018**, *38*, 45-55.
291. Wyzgoski, M. G.; Novak, G. E. Stress cracking of nylon polymers in aqueous salt solutions. *Journal of materials science* **1987**, *22*, 1715-1723.
292. Gadgil, H. S.; Pipes, G. D.; Dillon, T. M.; Treuheit, M. J.; Bondarenko, P. V. Improving mass accuracy of high performance liquid chromatography/electrospray ionization time-of-flight mass spectrometry of intact antibodies. *J. Am. Soc. Mass. Spectrom.* **2006**, *17*, 867-872.
293. Rivat, C.; Sertillanges, P.; Patin, E.; Stoltz, J. Single-step method for purification of human transferrin from a by-product of chromatographic fractionation of plasma. *Journal of Chromatography B: Biomedical Sciences and Applications* **1992**, *576*, 71-77.
294. Sawatzki, G.; Anselstetter, V.; Kubanek, B. Isolation of mouse transferrin using salting-out chromatography on Sepharose CL-6B. *Biochimica et Biophysica Acta (BBA)-Protein Structure* **1981**, *667*, 132-138.
295. Ghosh, R. Separation of proteins using hydrophobic interaction membrane chromatography. *J. Chromatogr. A* **2001**, *923*, 59-64.
296. Boi, C.; Dimartino, S.; Sarti, G. C. Performance of a new protein a affinity membrane for the primary recovery of antibodies. *Biotechnol. Prog.* **2008**, *24*, 640-647.
297. Rieman III, W. Salting-out chromatography: A review. *J. Chem. Educ.* **1961**, *38*, 338.
298. Dondi, F.; Munari, P.; Remelli, M.; Cavazzini, A. Monte Carlo model of nonlinear chromatography. *Anal. Chem.* **2000**, *72*, 4353-4362.
299. Cavazzini, A.; Dondi, F.; Jaulmes, A.; Vidal-Madjar, C.; Felinger, A. Monte Carlo model of nonlinear chromatography: correspondence between the microscopic stochastic model and the macroscopic Thomas kinetic model. *Anal. Chem.* **2002**, *74*, 6269-6278.
300. Giddings, J. C., *Dynamics of chromatography: principles and theory*. CRC Press: 1965.
301. Vanderheyden, Y.; Vanderlinden, K.; Broeckhoven, K.; Desmet, G. Problems involving the determination of the column-only band broadening in columns producing narrow and tailed peaks. *J. Chromatogr. A* **2016**, *1440*, 74-84.
302. Felinger, A., *Data analysis and signal processing in chromatography*. Elsevier: 1998; Vol. 21.
303. Gritti, F.; Guiochon, G. Accurate measurements of the true column efficiency and of the instrument band broadening contributions in the presence of a chromatographic column. *J. Chromatogr. A* **2014**, *1327*, 49-56.

304. Song, S.; Ravensbergen, K.; Alabanza, A.; Soldin, D.; Hahm, J.-i. Distinct Adsorption Configurations and Self-Assembly Characteristics of Fibrinogen on Chemically Uniform and Alternating Surfaces including Block Copolymer Nanodomains. *ACS Nano* **2014**, *8*, 5257-5269.
305. Wang, Z.; Yan, Y.; Qiao, L. Protein adsorption on implant metals with various deformed surfaces. *Colloids and Surfaces, B: Biointerfaces* **2017**, *156*, 62-70.
306. Michael, K. E.; Vernekar, V. N.; Keselowsky, B. G.; Meredith, J. C.; Latour, R. A.; García, A. J. Adsorption-Induced Conformational Changes in Fibronectin Due to Interactions with Well-Defined Surface Chemistries. *Langmuir* **2003**, *19*, 8033-8040.
307. Hu, W. J.; Eaton, J. W.; Tang, L. Molecular basis of biomaterial-mediated foreign body reactions. *Blood* **2001**, *98*, 1231-1238.
308. Garrett, Q.; Garrett, R. W.; Milthorpe, B. K. Lysozyme sorption in hydrogel contact lenses. *Investigative Ophthalmology & Visual Science* **1999**, *40*, 897-903.
309. Deng, X. M.; Castillo, E. J.; Anderson, J. M. Surface modification of soft contact lenses: Silanization, wettability and lysozyme adsorption studies. *Biomaterials* **1986**, *7*, 247-251.
310. Daniels, C. R.; Reznik, C.; Kilmer, R.; Felipe, M. J.; Tria, M. C. R.; Kourentzi, K.; Chen, W. H.; Advincula, R. C.; Willson, R. C.; Landes, C. F. Permeability of anti-fouling PEGylated surfaces probed by fluorescence correlation spectroscopy. *Colloid Surf., B* **2011**, *88*, 31-38.
311. Szleifer, I. Protein adsorption on tethered polymer layers: effect of polymer chain architecture and composition. *Physica A: Statistical Mechanics and its Applications* **1997**, *244*, 370-388.
312. Herrwerth, S.; Eck, W.; Reinhardt, S.; Grunze, M. Factors that determine the protein resistance of oligoether self-assembled monolayers– internal hydrophilicity, terminal hydrophilicity, and lateral packing density. *J. Am. Chem. Soc.* **2003**, *125*, 9359-9366.
313. Yu, Z.; Yahsi, U.; McGervey, J.; Jamieson, A.; Simha, R. Molecular weight-dependence of free volume in polystyrene studied by positron annihilation measurements. *J. Polym. Sci., Part B: Polym. Phys.* **1994**, *32*, 2637-2644.
314. White, R. P.; Lipson, J. E. Polymer free volume and its connection to the glass transition. *Macromolecules* **2016**, *49*, 3987-4007.
315. Tant, M.; Wilkes, G. An overview of the nonequilibrium behavior of polymer glasses. *Polymer Engineering & Science* **1981**, *21*, 874-895.
316. Nagel, C.; Günther-Schade, K.; Fritsch, D.; Strunskus, T.; Faupel, F. Free volume and transport properties in highly selective polymer membranes. *Macromolecules* **2002**, *35*, 2071-2077.
317. Kobayashi, Y.; Zheng, W.; Meyer, E.; McGervey, J.; Jamieson, A.; Simha, R. Free volume and physical aging of poly (vinyl acetate) studied by positron annihilation. *Macromolecules* **1989**, *22*, 2302-2306.
318. Malekmotiei, L.; Voyiadjis, G. Z.; Samadi-Dooki, A.; Lu, F.; Zhou, J. Effect of annealing temperature on interrelation between the microstructural evolution and

plastic deformation in polymers. *J. Polym. Sci., Part B: Polym. Phys.* **2017**, *55*, 1286-1297.

319. Liu, M.; Zhang, Y.; Wang, M.; Deng, C.; Xie, Q.; Yao, S. Adsorption of bovine serum albumin and fibrinogen on hydrophilicity-controllable surfaces of polypyrrole doped with dodecyl benzene sulfonate—A combined piezoelectric quartz crystal impedance and electrochemical impedance study. *Polymer* **2006**, *47*, 3372-3381.

320. Pothula, K. R.; Smyrnova, D.; Schröder, G. F. Clustering cryo-EM images of helical protein polymers for helical reconstructions. *Ultramicroscopy* **2019**, *203*, 132-138.

321. Lord, S. J.; Lee, H.-I. D.; Moerner, W. Single-molecule spectroscopy and imaging of biomolecules in living cells. *Anal. Chem.* **2010**, *82*, 2192-2203.

322. Daniels, C. R.; Tauzin, L. J.; Foster, E.; Advincula, R. C.; Landes, C. F. On the pH-Responsive, Charge-Selective, Polymer-Brush-Mediated Transport Probed by Traditional and Scanning Fluorescence Correlation Spectroscopy. *J. Phys. Chem. B* **2013**, *117*, 4284-4290.

323. Cordes, T.; Moerner, W.; Orrit, M.; Sekatskii, S.; Faez, S.; Borri, P.; Goswami, H. P.; Clark, A.; El-Khoury, P.; Mayr, S. Plasmonics, tracking and manipulating, and living cells: general discussion. *Faraday discussions* **2015**, *184*, 451-473.

324. Bishop, L. D.; Landes, C. F. From a Protein's Perspective: Elution at the Single-Molecule Level. *Acc. Chem. Res.* **2018**, *51*, 2247-2254.

325. Moringo, N. A.; Bishop, L. D. C.; Shen, H.; Misiura, A.; Carrejo, N. C.; Baiyasi, R.; Wang, W.; Ye, F.; Robinson, J. T.; Landes, C. F. A mechanistic examination of salting out in protein-polymer membrane interactions. *Proc. Natl. Acad. Sci. U.S.A.* **2019**, 201909860.

326. Huopalahti, R.; Anton, M.; López-Fandiño, R.; Schade, R., *Bioactive egg compounds*. Springer: 2007.

327. Bramaud, C.; Aimar, P.; Daufin, G. Whey protein fractionation: Isoelectric precipitation of α -lactalbumin under gentle heat treatment. *Biotechnology and bioengineering* **1997**, *56*, 391-397.

328. Breite, D.; Went, M.; Prager, A.; Schulze, A. Tailoring membrane surface charges: A novel study on electrostatic interactions during membrane fouling. *Polymers* **2015**, *7*, 2017-2030.

329. Swaminathan, R.; Ravi, V. K.; Kumar, S.; Kumar, M. V. S.; Chandra, N., Lysozyme: a model protein for amyloid research. In *Advances in protein chemistry and structural biology*, Elsevier: 2011; Vol. 84, pp 63-111.

330. Permyakov, E. A.; Berliner, L. J. α -Lactalbumin: structure and function. *FEBS Lett.* **2000**, *473*, 269-274.

331. Ulsan, S.; Bütün, V.; Banerjee, S.; Erel-Goktepe, I. Biologically Functional Ultrathin Films Made of Zwitterionic Block Copolymer Micelles. *Langmuir* **2018**, *35*, 1156-1171.

332. Iyer, L. K.; Qasba, P. K. Molecular dynamics simulation of α -lactalbumin and calcium binding c-type lysozyme. *Protein Engineering* **1999**, *12*, 129-139.

333. Acharya, K. R.; Stuart, D. I.; Walker, N. P. C.; Lewis, M.; Phillips, D. C. Refined structure of baboon α -lactalbumin at 1.7 Å resolution: Comparison with C-type lysozyme. *Journal of Molecular Biology* **1989**, *208*, 99-127.
334. Bekele, S.; Tsige, M. Interfacial properties of oxidized polystyrene and its interaction with water. *Langmuir* **2013**, *29*, 13230-13238.
335. Honciuc, A.; Harant, A. W.; Schwartz, D. K. Single-molecule observations of surfactant diffusion at the solution– solid interface. *Langmuir* **2008**, *24*, 6562-6566.
336. Walder, R.; Nelson, N.; Schwartz, D. K. Single molecule observations of desorption-mediated diffusion at the solid-liquid interface. *Physical review letters* **2011**, *107*, 156102.
337. Gast, K.; Zirwer, D.; Müller-Frohne, M.; Damaschun, G. Compactness of the kinetic molten globule of bovine α -lactalbumin: A dynamic light scattering study. *Protein Sci.* **1998**, *7*, 2004-2011.
338. Xiaoyan, M.; Jun, Q. L.; Brock, R. S.; Kenneth, M. J.; Ping, Y.; Xin-Hua, H. Determination of complex refractive index of polystyrene microspheres from 370 to 1610 nm. *Physics in Medicine and Biology* **2003**, *48*, 4165.
339. Shuang, B.; Chen, J.; Kisley, L.; Landes, C. F. Troika of single particle tracking programing: SNR enhancement, particle identification, and mapping. *Phys. Chem. Chem. Phys.* **2014**, *16*, 624-634.
340. Bates, M.; Huang, B.; Dempsey, G. T.; Zhuang, X. Multicolor Super-Resolution Imaging with Photo-Switchable Fluorescent Probes. *Science* **2007**, *317*, 1749-1753.
341. Weilin Xu, H. S., Yoon Ji Kim, Xiaochun Zhou, Guokun Liu, Jiwoong Park, and Peng Chen Single-Molecule Electrocatalysis by Single-Walled Carbon Nanotubes. *Nano Lett.* **2009**, *9*, 3968-3973.
342. Rust, M. J.; Bates, M.; Zhuang, X. Sub-diffraction-limit imaging by stochastic optical reconstruction microscopy (STORM). *Nat Meth* **2006**, *3*, 793-796.
343. James, S.; McManus, J. J. Thermal and solution stability of lysozyme in the presence of sucrose, glucose, and trehalose. *J. Phys. Chem. B.* **2012**, *116*, 10182-10188.
344. West, D.; McBrierty, V.; Delaney, C. Positron decay in polymers: Molecular weight dependence in polystyrene. *Applied physics* **1975**, *7*, 171-174.
345. Montroll, E. W.; Weiss, G. H. Random walks on lattices. II. *Journal of Mathematical Physics* **1965**, *6*, 167-181.
346. Nitta, K.; Sugai, S. The evolution of lysozyme and α -lactalbumin. *European Journal of Biochemistry* **1989**, *182*, 111-118.
347. Nitta, K., α -Lactalbumin and (Calcium-Binding) Lysozyme. In *Calcium-Binding Protein Protocols*, Vogel, H., Ed. Humana Press: 2002; Vol. 172, pp 211-224.
348. Qasba, P. K.; Kumar, S.; Brew, K. Molecular Divergence of Lysozymes and α -Lactalbumin. *Critical Reviews in Biochemistry and Molecular Biology* **1997**, *32*, 255-306.
349. Sandreczki, T.; Hong, X.; Jean, Y. Sub-glass-transition-temperature annealing of polycarbonate studied by positron annihilation spectroscopy. *Macromolecules* **1996**, *29*, 4015-4018.

350. Ton-That, C.; Shard, A.; Daley, R.; Bradley, R. Effects of annealing on the surface composition and morphology of PS/PMMA blend. *Macromolecules* **2000**, *33*, 8453-8459.
351. Hougham, G.; Tesoro, G.; Viehbeck, A. Influence of free volume change on the relative permittivity and refractive index in fluoropolyimides. *Macromolecules* **1996**, *29*, 3453-3456.
352. Sugiyama, M.; Nakamura, Y.; Norisuye, T. Dilute-solution properties of polystyrene polymacromonomer having side chains of over 100 monomeric units. *Polym. J.* **2008**, *40*, 109.
353. Wang, R.; Wang, Z.-G. Theory of polymer chains in poor solvent: Single-chain structure, solution thermodynamics, and θ point. *Macromolecules* **2014**, *47*, 4094-4102.
354. Ayen, W. Y.; Chintankumar, B.; Jain, J. P.; Kumar, N. Effect of PEG chain length and hydrophilic weight fraction on polymersomes prepared from branched (PEG) 3-PLA co-polymers. *Polym. Adv. Technol.* **2011**, *22*, 158-165.
355. Brumaru, C.; Geng, M. L. Interaction of surfactants with hydrophobic surfaces in nanopores. *Langmuir* **2010**, *26*, 19091-19099.
356. Elliott, L. C.; Barhoum, M.; Harris, J. M.; Bohn, P. W. Single molecule tracking studies of lower critical solution temperature transition behavior in poly (N-isopropylacrylamide). *Langmuir* **2011**, *27*, 11037-11043.
357. Thevis, M.; Loo, R. R. O.; Loo, J. A. Mass spectrometric characterization of transferrins and their fragments derived by reduction of disulfide bonds. *J. Am. Soc. Mass. Spectrom.* **2003**, *14*, 635-647.
358. Shen, Z. M.; Yang, J. T.; Feng, Y. M.; Wu, C. S. C. Conformational stability of porcine serum transferrin. *Protein Sci.* **1992**, *1*, 1477-1484.
359. Schöler, J.; Frank, J.; Trier, U.; Schäfer-Korting, M.; Saenger, W. Interaction kinetics of tetramethylrhodamine transferrin with human transferrin receptor studied by fluorescence correlation spectroscopy. *Biochemistry* **1999**, *38*, 8402-8408.
360. Lu, H. P.; Xun, L.; Xie, X. S. Single-molecule enzymatic dynamics. *Science* **1998**, *282*, 1877-1882.
361. Xu, W.; Kong, J. S.; Chen, P. Single-molecule kinetic theory of heterogeneous and enzyme catalysis. *J. Phys. Chem. C* **2009**, *113*, 2393-2404.
362. Makabe, K.; Nakamura, T.; Kuwajima, K. Structural insights into the stability perturbations induced by N-terminal variation in human and goat α -lactalbumin. *Protein Engineering, Design & Selection* **2012**, *26*, 165-170.
363. Kundrot, C. E.; Richards, F. M. Crystal structure of hen egg-white lysozyme at a hydrostatic pressure of 1000 atmospheres. *J. Mol. Biol.* **1987**, *193*, 157-170.